九州大学学術情報リポジトリ
Kyushu University Institutional Repository

Study on Microstructure and Electrical Resistance of Surface Oxide Layer of Fe-Cr-Al Alloy for Solid Oxide Fuel Cell Applications

ファム, フン クオン

https://doi.org/10.15017/1654881

出版情報：九州大学, 2015, 博士（工学）, 課程博士
バージョン：
権利関係：全文ファイル公表済

KYUSHU UNIVERSITY

Study on Microstructure and Electrical Resistance of Surface Oxide Layer of Fe-Cr-Al Alloy for Solid Oxide Fuel Cell Applications

by
Pham Hung-Cuong

Department of Hydrogen Energy Systems
Graduate School of Engineering
Kyushu University

SUBMITTED TO THE GRADUATE SCHOOL OF ENGINEERING
IN PARTIAL FULFILLMENT OF THE REQUIREMENTS FOR THE
DEGREE OF DOCTOR OF ENGINEERING

Kyushu University

Approved by:

Prof. Dr. Kazunari SASAKI, thesis examiner/supervisor
Department of Hydrogen Energy Systems,
Graduate School of Engineering, Kyushu University

Prof. Dr. Shunsuke TANIGUCHI, thesis co-examiner/co-supervisor
International Research Center for Hydrogen Energy, Kyushu University

Prof. Dr. Yoshihiro YAMAZAKI, thesis co-examiner
Department of Materials Physics and Chemistry,
Graduate School of Engineering, Kyushu University

Associate Prof. Dr. Yusuke SHIRATORI, thesis co-examiner
Department of Hydrogen Energy Systems,
Graduate School of Engineering, Kyushu University

Fukuoka, Japan

Abstract

Solid Oxide Fuel Cells (SOFCs) are considered to be a promising power generation system because they offer advantages of high energy conversion efficiency, fuel flexibility and low pollutant. SOFCs are expected to show higher durability compared to the other fuel cells because their component materials are solid state with lower corrosive materials. However, several challenges such as improved long-term durability, higher start up, lower material costs and fabrication costs are remained to be solved to expand SOFC products in the market. Metal-supported SOFC (MSC) is the best candidate to solve the above challenges. Durability of MSC can be significantly improved because of high mechanical strength, high thermal conductivity, high electrical conductivity of the metal support. Therefore, this study is related to MSC and deals with a metal support material which will be the core technology of the future SOFC. We investigated the property of a new material of Fe-Cr-Al alloy for a porous alloy substrate of MSC. The Fe-Cr-Al alloy generally shows high oxidation resistance in air because of the formation of mainly alumina-based oxide layer on the surface as a protective layer. This layer can prevent the chromium diffusion from the alloy to the electrode materials. Understanding the relationship among microstructure (crystal structure and elemental composition) of the oxide layer, electrical conductivity and heat resistance is important to improve the performance and long-term durability of MSCs.

The dissertation starts with the general introductory of fuel cells and describes how to expand SOFC products in the market. In Chapter 2, MSC is overviewed with key issues for commercialization, which lead to the objectives of this study. Experimental method of porous alloy fabrication, electrical resistance measurement, and analysis of the surface oxide layer are presented in Chapter 3.

In Chapter 4, we succeeded in decreasing electrical resistance of the surface oxide layer of the Fe-Cr-Al alloy. A relatively low electrical resistance was obtained when the porous alloy substrate was coated with $La_{0.6}Sr_{0.4}Co_{0.2}Fe_{0.8}O_3$ (LSCF) and heat-treated at 700–800 °C in air. The morphology of the surface oxide layer observed by high-resolution transmission electron microscopy was columnar structure of γ-Al_2O_3 polycrystal and $Sr_3Al_2O_6$ growing outward in the same direction. We hypothesized that the electronic conduction path was generated at thin interface of γ-Al_2O_3/ $Sr_3Al_2O_6$. The

columnar structure arranged perpendicular to the surface may also contribute to the enhancement of the electronic conductivity. In contrast, the surface oxide layer of the alloy showed a high electrical resistance when the uncoated porous alloy substrate was heat-treated. The morphology of the surface oxide layer in that case was a columnar structure consisting of only γ-Al_2O_3 growing outward in various directions.

In Chapter 5, we obtained the similar results with the case of LSCF using $La_{0.8}Sr_{0.2}MnO_3$ (LSM), $LaNi_{0.6}Fe_{0.4}O_3$ (LNF), $Pr_{0.8}Sr_{0.2}MnO_3$ (PrSM) for the coating materials. In the surface oxide layer, small amount of La, Ni, Pr or Sr were observed. It is expected that the same microstructure, as discussed in Chapter 4, consisting of γ-Al_2O_3 columnar crystal growing outward in the same direction, and small amount of aluminum compound with La, Ni, Pr or Sr was formed for each material. In the case of LNF, the interfacial resistance and activation energy of the electrical conduction were slightly lower than the other cases. Possibility of formation of γ-$Al_2O_3/NiAl_2O_4$, with higher electronic conductivity than γ-$Al_2O_3/Sr_3Al_2O_6$, between γ-Al_2O_3 columnar crystals was suggested.

In Chapter 6, we confirmed long-term durability of the oxidation resistance of the LSCF-coated Fe-Cr-Al alloy at 700 °C by measuring the mass gain, surface oxide thickness, and electrical resistance at different temperatures from 700 to 900 °C. The mass gain of the alloy at 700 and 900 °C followed a parabolic law. By extrapolation of the data, we estimated the mass gain after 17,000 h at 700 °C to be equal to that after 230 h at 900 °C. We thus estimated that the interfacial resistance of the porous alloy substrate at 700 °C will increase from 20 $m\Omega cm^2$ to 53 $m\Omega cm^2$ after 17,000 h of operation based on the results at 900 °C after 230 h in air. Therefore, we regarded this alloy as a candidate material for commercialization.

In Chapter 7, we concluded this study. We have clarified that the Fe-Cr-Al alloy can be applied for the porous alloy substrate of MSCs. We can expect high durability of MSCs using this material because of not only its stability but also less chromium evaporation.

固体酸化物形燃料電池への適用を目指した Fe-Cr-Al 合金の表面酸化物の微細構造と電気抵抗に関する研究

論文内容の要旨

固体酸化物形燃料電池（SOFC）は、高効率でクリーンな発電が可能であり、様々な燃料種や発電規模（携帯用から大規模発電まで）にも適用できるため、広く実用化・普及が期待されている。その他の燃料電池と比較して、SOFC は構成材料が固体であり腐食性材料を含まないため、高い耐久性を示すことも期待される。しかし現状の技術では、発電の基本単位であるセルの機械的安定性が十分でなく、急速起動時にセルが割れる等の課題がある。また比較的高価な元素が多く用いられるため材料コストにも課題がある。安価な鉄を主成分とするステンレス鋼を支持体に用いるメタルサポート SOFC は、支持体の高い機械強度や加工性、高い熱伝導性、高い電子伝導性により、これらの課題を解決できる有望な次世代技術と位置付けられている。従来のメタルサポート SOFC 開発では、支持体に Fe-Cr 合金が用いられてきたが、表面に生成する Cr_2O_3 層の時間的な膜厚増加による抵抗増加、表面から気化するクロム酸化物（CrO_3(g)等）が引き起こす電極の被毒（クロム被毒）の問題があった。別の合金種である Fe-Cr-Al 合金は、表面に生成する Al_2O_3 層が、高温で高い安定性を示すだけでなくクロム成分を含まない利点があるが、これまで Al_2O_3 層の電気抵抗が高い問題があったため、SOFC 用の材料としては検討されて来なかった。

本研究は、メタルサポート SOFC 実現のため最も重要な支持体材料として、これまで検討されて来なかった Fe-Cr-Al 合金に着目し、表面に生成する Al_2O_3 層の電気抵抗を低減する処理法を開発した。この処理により、表面 Al_2O_3 層は微量の $Sr_3Al_2O_6$ を含有し、ナノサイズの柱状γ-Al_2O_3 結晶が同一方向に整列した特異な微細構造に変化することを明らかにした。電子伝導性発現の機構として、同一方向に整列した柱状結晶に沿って生成したγ-Al_2O_3/$Sr_3Al_2O_6$ ヘテロ界面が電子伝導を促す機構を推論した。また、Sr 以外にも Ni や Pr でも同様の効果が得られることを明らかにした。さらに温度上昇による加速試験法を適用し、700 ^{o}C で 2 万時間程度の安定性が期待されることも確認した。これらの成果により、

耐久性に優れたFe-Cr-Al合金をSOFCに適用することが可能になり、SOFCの飛躍的な耐久性向上に貢献できる。

本論文は以下の7章で構成される。

第1章では、燃料電池の一般論からSOFCの原理、開発の経緯、開発動向、課題等を述べた。

第2章では、次世代技術として期待されるメタルサポートSOFCの研究開発状況と普及までの課題を述べた。特に、支持体に用いる合金材料の酸化進行や、合金表面から拡散するクロム成分が引き起こす電極被毒が問題であり、これらの解決を目指すことが本研究の動機であることを述べた。

第3章では、本研究における実験方法である多孔質のメタルサポートの作製方法、電気抵抗の測定方法、耐酸化性の評価方法、高分解能電子顕微鏡観察（FIB, TEM, STEM, EDS）および結晶構造解析手法を述べた。

第4章では、Fe-Cr-Al合金の表面に生成するAl_2O_3層を、電子伝導に適した特異な微細構造に変化させることに成功した。具体的には、合金表面に予め$La_{0.6}Sr_{0.4}Co_{0.2}Fe_{0.8}O_3$ (LSCF)をコーティングし、空気中700–800 ^{o}Cで熱処理することにより、表面Al_2O_3層の電気抵抗が低下し時間的にも安定となった。高分解能像観察および結晶構造解析によって、ナノサイズのγ-Al_2O_3からなる柱状結晶が合金内部から外側に向かって同一方向に整列し、その中に数%程度の$Sr_3Al_2O_6$が複合化した構造へと変化することを明らかにした。γ-Al_2O_3や$Sr_3Al_2O_6$は高抵抗材料ではあるが、同一方向に整列した柱状結晶に沿って生成したγ-Al_2O_3/$Sr_3Al_2O_6$ヘテロ界面が電子伝導を促し、電子伝導率を1000倍以上向上させる機構を推論した。一方、この処理を施さない通常の酸化状態では、結晶性の高い比較的大きなγ-Al_2O_3が様々な方向に成長しており電気抵抗が高かった。　第5章では、本研究で考案した処理法に対して、種々のコーティング材$La_{0.8}Sr_{0.2}MnO_3$ (LSM), $LaNi_{0.6}Fe_{0.4}O_3$ (LNF), $Pr_{0.8}Sr_{0.2}MnO_3$ (PrSM)を適用し、表面酸化物層中に固溶させる元素種の影響を検討した。その結果、LSCFを用いた場合と同様に、合金表面には同一方向に揃った柱状結晶からなる酸化物層(Al_2O_3)が成長し、これらの酸化物層は高い電子伝導性を示すことを確認した。酸化物層に含まれる微量元素は、LSMの場合Sr、LNFの場合Ni、PrSMの場合Prであり、同一方向に揃ったナノサイズの柱状γ-Al_2O_3結晶に沿って生成するγ-Al_2O_3/$Sr_3Al_2O_6$、γ-Al_2O_3/$NiAl_2O_4$、γ-Al_2O_3/$PrAlO_3$等のヘテロ界面が電子伝導経

路となる機構を推論した。特にγ-Al_2O_3/$NiAl_2O_4$ 場合、電子伝導の活性化エネルギーが小さく、電子伝導性がさらに向上する可能性を見出した。

第 6 章では、温度上昇による加速試験法を適用してこの材料の耐久性を評価し、700 ^{o}C で 2 万時間程度の安定性を確認した。LSCF をコートした Fe-Cr-Al 合金を用い、700 ^{o}C から 900 ^{o}C の温度で重量増加、酸化物層厚さ、電気抵抗を測定した。酸化物層厚さや重量増加が放物線則に従い、700 ^{o}C でのデータの外挿により、900 ^{o}C における酸化速度は、700 ^{o}C における酸化速度の約 70 倍であると見積もり、その結果 700 ^{o}C で初期 20 mΩcm^2 程度である抵抗が、17,000 時間後には 50 mΩcm^2 程度まで上昇するものと推定した。さらなる抵抗低減や安定性向上の課題は残るものの、将来有望な材料であることを確認した。

第 7 章では本論文を総括し、Fe-Cr-Al 合金がクロム被毒の問題を回避できる有望な材料として SOFC に適用可能であることを明確に示した。

Contents

List of Figures

List of Tables

Chapter 1

General Introduction

1.1 Fuel cell

1.1.1 Basic principles

Fuel cell is a device that converts chemical energy directly into electrical energy. Its operation can be explained using electrochemical concepts that are now well understood. Fuel cell was originally invented by Sir William Robert Grove in 1839 [1]. Grove's fuel cell is one of the simplest examples, for which the reactions are described in Table 1.1.

Table 1-1. Electrode reactions for Grove's fuel cell

Half-reaction at the anode:	$H_2 \leftrightarrow 2H^+ + 2e$	$E^o = 0$ V	(1.1)
Half-reaction at the cathode:	$1/2O_2 + 2H^+ + 2e \leftrightarrow H_2O$	$E^o = 1.23$ V	(1.2)
Net reaction (the combustion reaction):	$H_2 + 1/2O_2 \leftrightarrow H_2O$	$E^o = 1.23$ V	(1.3)

He made several important improvements to the design of batteries and found that the combination of hydrogen and oxygen can be used to produce electricity. Fuel cell can run continuously as long as it has fuel and oxygen fed from outside, in contrast to the secondary batteries that store limited energy inside via active materials. The hydrogen needed for the fuel cell reaction can be extracted from hydrocarbon such as natural gas, LPG, alcohol and gasoline. They are fed to the anode (negative electrode), one of two electrodes of the cell.

Theoretical efficiency of fuel cells can be described as the following equation:

$$\mu_G = \frac{\Delta G}{\Delta H} = 1 - \frac{T \times \Delta S}{\Delta H} \tag{1.4}$$

where, ΔH is the change of enthalpy, ΔG is the change in Gibbs free energy, and ΔS is the change in entropy of the fuel cell reaction. In the case of combustion, the energy corresponding to ΔH is converted to heat generation. In the case of the fuel cell reaction, the energy corresponding to ΔG can be converted to electrical energy by the following equations:

$$\Delta G^o = -nFE^o \tag{1.5}$$

and

$$\Delta G = -nFE \tag{1.6}$$

$$E = E^o - \frac{RT}{nF}\ln\Phi \tag{1.7}$$

E is the theoretical voltage, T is the absolute temperature, R is the gas constant, n is the number of electrons involved in the reaction, F is the Faraday's constant, Φ is the chemical activity.

1.1.2 Fuel cell types

Many types of fuel cells have been developed. The types of fuel cells are usually distinguished by the electrolyte materials as shown in Table 1-2.

Table 1-2. Different types of fuel cells.

System	Temperature	Power Density in Stack (kw/m^2)	Electrolyte	Application
AFC-Alkaline Fuel Cell	60-90 ^{o}C	2	KOH 30%	Space mobile
PEFC or PEM	60-80 ^{o}C	3	Nafion	Mobile and Stationary
PAFC-Phosphoric Acid	160-220 ^{o}C	1.3	H_3PO_4 conc.	Stationary up to 11MW
MCFC Molten Carbonate	620-660 ^{o}C	1.4	Li_2CO_3/ Na_2CO_3	Stationary up to MW
SOFC-Solid Oxide	500-1000 ^{o}C	6	YSZ/ScSZ	Stationary, 2kW to multi-MW

1.1.3 Advantages and applications

There are a lot of advantages of fuel cell. Fuel cells are generally more efficient than combustion engines or turbines. Fuel cells can generate electricity efficiently regardless of the system size and even a small system can show high efficiency. Fuel cells are very simple, with few moving parts, leading to highly reliable and long-lasting systems. Fuel cells are silent and easy to set-up. This is very important both for portable mobile applications and for stationary application. Each type of fuel cell has advantages depending on the electrolyte material and operating temperature and has been investigated for different applications.

Alkaline fuel cell (AFC) uses a solution of potassium hydroxide as an alkaline electrolyte. AFCs are operated at temperature around 70–250 ◦C. The primary advantages of the AFCs are the lower cost of materials and higher efficiency. AFCs were developed as an auxiliary power unit (APU) for space applications by the Soviet Union and US in the 1950s and served on the spaceship Apollo as well as the Space Shuttle orbiter.

Polymer electrolyte fuel cell (PEFC) has also been referred to as solid polymer electrolyte (SPE) fuel cell or proton exchange membrane (PEM) fuel cell. PEFCs are operated at low temperature around 60-80 ^{o}C. The advantages of low operating temperature allow lower cost, simple stack design and rapid start-up of the system. Thus, they can be alternative to automobile engines. Currently, PEFCs are developed for automotive and stationary (residential) applications in Japan.

Direct methanol fuel cell (DMFC) basically has the same component materials as PEFCs, but it utilizes liquid methanol directly as a fuel to generate electricity. In 2000s, DMFCs were investigated for mobile, portable applications such as cell phone or laptop PC, because energy density of methanol theoretically is much higher than lithium ion batteries.

Molten carbonate fuel cell (MCFC) operates at high temperature around 600–700 ^{o}C with a molten mixture of alkali metal carbonates such as lithium and sodium carbonates as electrolyte materials retained in a porous ceramic. MCFCs are suitable for larger scale power plant, and several companies commercialize MCFCs including a 250kW unit in US.

Phosphoric acid fuel cell (PAFC) uses highly concentrated phosphoric acid (H_3PO_4) solution, retained in a Teflon-bonded SiC matrix as the electrolyte. PAFCs are operated at around 160–220 ^{o}C, allowing PAFC operation with 1–2% CO in fuel. PAFC was developed for commercial application in 1960s, for example, over 200 kW commercial PAFC units were developed and sold by United Technologies Corporation. Durability up to several ten thousand hours was confirmed for PAFC systems.

Solid Oxide Fuel Cell (SOFC) is normally operated at around 600-900ºC using solid oxide electrolyte. The primary advantages of SOFC are higher electrical conversion efficiency and fuel flexibility compared to the other fuel cell because of higher operation compared to the other fuel cell systems. SOFCs also have advantages such as higher durability because component materials are solid state with no corrosive materials.

1.2 Solid oxide fuel cells

1.2.1 Brief history of solid oxide fuel cells

Solid oxide fuel cell was recognized following the discovery of solid oxide electrolytes by Nernst [2] in 1899. He compared the behavior of liquid electrolytes including aqueous salt solutions, and discovered that the aqueous salt solution is highly conductive, whereas the conductivities of pure water and pure common salt are very low. Many kinds of mixed oxides were also identified which show high conductivity at elevated temperatures. One of the conductive mixed oxides was yttria doped stabilized zirconia (ZrO_2 85%, Y_2O_3 15%). In this patent, Nernst proposed that the yttria doped stabilized zirconia could be used as an electrolyte material.

Haber invented solid electrolyte materials consisting of glass and porcelain for fuel cells in 1905 [3], in which platinum and gold were used for the electrode materials. Baur and Treadwell invented metal oxide electrode materials for fuel cells, in which ceramic solids with salt melts were used for the electrolyte in 1916 [4].

Baur and Preis used yttria doped stabilized zirconia as the electrolyte for solid oxide fuel cell in 1937 [5]. Yttria doped stabilized zirconia was tested at 1050 and

1100 °C in a ceramic tube made of brickyard clay and two types of unglazed porcelain, but the resistance of the electrolyte was high because of thickness.

Weissbart and Ruka at the Westinghouse Electric Corporation designed a SOFC that used 85% ZrO_2-15% CaO as the electrolyte and porous platinum as the electrodes in 1962 [6]. The cell had an area of 2.5 cm^2 and thickness of 0.15 cm and located at the bottom of a closed tube made of the same material as the electrolyte as shown in Figure 1-1.

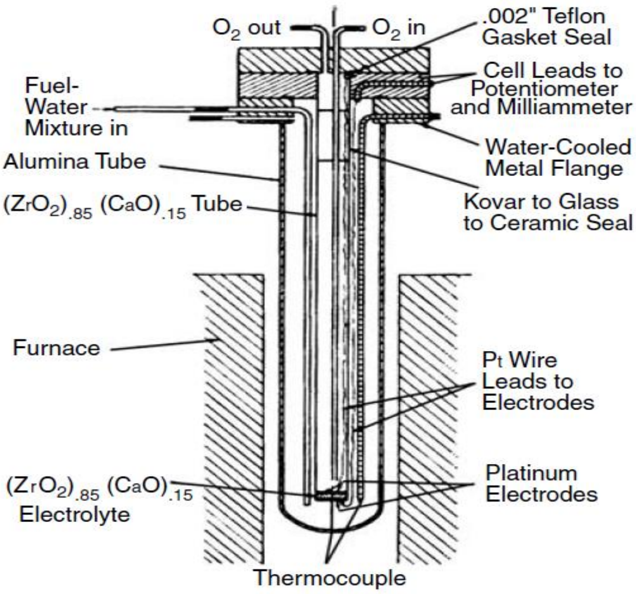

Figure 1-1. The SOFC developed by Westinghouse Electric Corporation using $(ZrO_2)_{0.85}(CaO)_{0.15}$ as the electrolyte [6].

In 1970s, many fabrication methods have been investigated to form thinner electrolytes; however, the performance was still low due to high resistance inside of the cell. In the last three decades, numerous designs including various tubular and planar designs and materials have been developed.

1.2.2 Operating principle of solid oxide fuel cell

Figure 1-2 shows the configuration and operating principle of SOFC. A single cell of SOFC consists of porous anode layer, porous cathode layer and dense electrolyte layer. Fuels such as H_2 and CH_4 oxidized at the anode by the oxygen ions (O^{2-}) coming through the electrolyte layer from the cathode side. Oxidant such as air is fed to the cathode, where oxygen ions are generated electrochemically at the cathode/electrolyte interface. The electrolyte layer conducts these oxygen ions from the cathode to the anode, maintaining overall electrical charge balance. The electrons flow from the anode to the cathode through the external circuit, providing electric power to the external load.

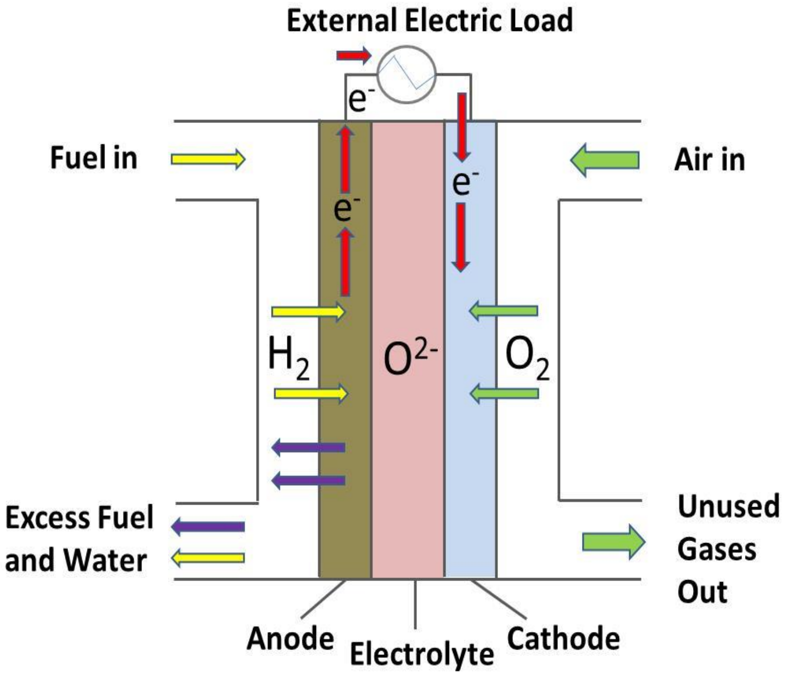

Figure 1-2. Operating principle of solid oxide fuel cell.

In SOFC, the difference in chemical potential ΔG of oxygen between the cathode and the anode is the driving force of the transport of oxygen ions in the electrolyte:

$$\Delta G = -2EF = \mu(\mathrm{O_2}, \mathrm{a}) - \mu(\mathrm{O_2}, \mathrm{c}) \tag{1.8}$$

where E is the theoretical voltage. Chemical potential of oxygen is described as follows:

$$\mu(\mathrm{O_2}) = \mu^{\mathrm{o}}(\mathrm{O_2}) + RT\ln p(\mathrm{O_2}) \tag{1.9}$$

Where $\mu^{\mathrm{o}}(\mathrm{O_2})$ is the standard chemical potential.

$$E = \frac{RT}{2F} \ln\left(\frac{p(O_2, c)}{p(O_2, a)} \right) \tag{1.10}$$

$$p(\mathrm{O}_2, a) = \frac{1}{K_H} \left(\frac{p(H_2O, a)}{p(H_2, a)} \right)^2, \Delta G_f^o = -RT \ln K_H \tag{1.11}$$

where K_H is the equilibrium constant of the reaction below,

$$\mathrm{H_2 + 1/2O_2 \leftrightarrow H_2O} \tag{1.12}$$

ΔG_f^o is the standard Gibbs free energy of H_2O formation.

Therefore, the correlation between the partial pressure and the theoretical voltage is given by the following equation:

$$E = -\frac{\Delta G_f^o}{2F} - \frac{RT}{F} \ln\left(\frac{P(H_2O, a)}{P(H_2, a)}, a \right) + \frac{RT}{2F} \ln P(O_2, c) \tag{1.13}$$

Open circuit voltage (OCV) is equal to the theoretical voltage (*E*) calculated above when the electrolyte is a pure ionic conductor (with no electronic conduction). In the operation, cell voltage becomes lower than the OCV because of voltage losses due to internal resistances of the cell.

The electrochemical reactions and energy generated in SOFC utilizing hydrogen as a fuel at 900 ^{o}C are shown in Table 1.3.

Table 1-3. Electrode reactions and energy generated in SOFC at 900 ^{o}C

Anode:	$\mathrm{H_2 + O^{2-} \rightarrow H_2O + 2e}$	$E^o = 0$ V	(1.14)
Cathode:	$\mathrm{1/2O_2 + 2e \rightarrow O^{2-}}$	$E^o = 0.89$ V	(1.15)
Overall:	$\mathrm{H_2 + 1/2O_2 \rightarrow H_2O}$	$E^O = 0.89$ V, ΔH = -248.8 KJ/mol	(1.16)

1.2.3 Components of solid oxide fuel cell

1.2.3.1 Cathode materials

General perovskite type oxide

Cathode is the place where oxygen is reduced to oxygen ions by the following equation.

$$O_2 + 2e^- \leftrightarrow O^{2-} \tag{1.17}$$

Cathode of SOFC should possess not only high electronic conductivity for current collection, high ionic conductivity for oxygen transfer, and catalytic activity for oxygen reduction but also a suitable porosity for diffusion of gas reactants. Moreover, the cathode should be mechanically and chemically compatible with the other components such as electrolyte under fabrication and operation conditions. In addition to the high activity and stability, enough tolerance against poisoning toward contaminants is required, for example, chromium contaminations from alloy-based metal support or interconnector.

Perovskite oxides are the most commonly used cathode materials of SOFCs. Perovskite oxides have the general formula ABO_3, with the unit cell shown in Figure 1-3. The ideal unit of perovskite is a cubic structure. Usually, some distortions, such as cation displacements within the octahedral and tilting of the octahedral, appear in the perovskite lattice, which are caused by substitution of A or B site by other elements [7]. Distortion degree of perovskite can be described by the Goldschmidt tolerance factor *t*,

$$r_A + r_O = t\sqrt{2}(r_B + r_O) \tag{1.18}$$

where r_A, r_B, and r_O represent for the atomic size of A, B, and O sites, respectively. Because a wide range of tolerance factor ($0.7 < t < 1.1$) on the ion radius can be accepted, modification of a perovskite oxide with different doping ions and different concentrations is possible to create material with designed properties [8]. For the A site, rare earth element such as lanthanum is used with dopants of alkaline earth elements such as Ca and Sr. For the B site, transition metals such as Mn, Fe, Co, Ni etc. are used. Conventionally, several kinds of perovskite materials such as $La_{1-x}Sr_xMnO_{3-\delta}$ (LSM) and $La_{1-x}Sr_xCoO_{3-\delta}$, (LSC) and $La_{1-x}Sr_xCo_{1-y}Fe_yO_{3-\delta}$ (LSCF) were used for SOFC cathodes.

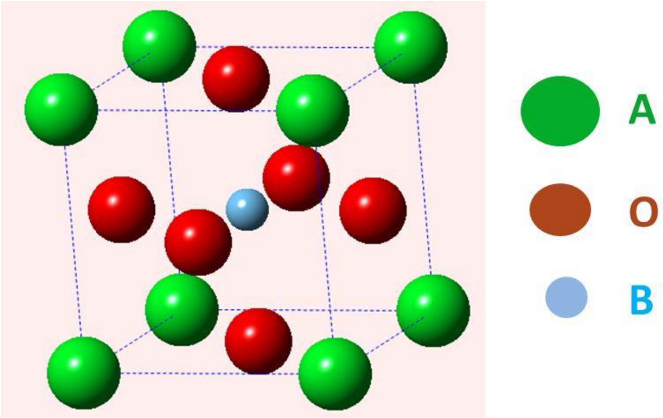

Figure 1-3. Unit cell of ABO_3 perovkite structure.

Lanthanum strontium cobaltite (LSC)

$La_{1-x}Sr_xCoO_{3-\delta}$ (LSC) was one of the first perovskite oxides investigated for cathode material of SOFC [9]. LSC shows high electrochemical activity, and has been used as a cathode material for SOFCs. LSC shows a complex behavior with regard to oxygen nonstoichiometry, crystal structure, electrical conductivity, and catalytic activity depending on the strontium content, temperature, and oxygen partial pressure. The model of LSC which describes the defect structure is given by Petrov [10]. $\mathrm{Co_{Co}^{\bullet}}$ and $\mathrm{V_{O}^{\bullet\bullet}}$ are formed in the lattice to maintain electrical neutrality, which is caused by the substitution of Sr ions on La sites. The overall electrical neutrality condition is shown as follows equations,

$$\mathrm{Sr_{Sr}^{X} + Co_{Co}^{\bullet} + 2V_{O}^{\bullet\bullet} \leftrightarrow Sr_{La}^{'} + Co_{Co}^{X}} \tag{1.19}$$

$$\mathrm{2Co_{Co}^{\bullet} + O_{O}^{X} \leftrightarrow 2Co_{Co}^{X} + V_{O}^{\bullet\bullet} + 1/2O_2} \tag{1.20}$$

$$[\mathrm{V_{O}^{\bullet\bullet}}][\mathrm{Co_{Co}^{X}}]^2 \leftrightarrow K_{V_O^{\bullet\bullet}}[\mathrm{Co_{Co}^{\bullet}}]^2[\mathrm{O_{O}^{X}}]P_{O_2}^{-1/2} \tag{1.21}$$

where $\mathrm{Co}_{\mathrm{Co}}^{\bullet}$ and $\mathrm{Co}_{\mathrm{Co}}^{\mathrm{X}}$ represent for the Co^{4+} and Co^{3+} ions at B site, respectively, and $K_{V_O^{\bullet\bullet}}$ is the defect equilibrium constant.

Lanthanum strontium manganite (LSM)

LSM has oxygen excess nonstoichiometries unlike the other cathode materials which has oxygen deficiency. To describe the nonstoichiometry of LSM by oxygen partial pressure, a model has been given by Van Roosmalen and Cordfunke as the following equations [11,12].

Oxygen excess:

$$3/2\mathrm{O}_2 + 6\mathrm{Mn}_{\mathrm{Mn}}^{\mathrm{X}} \leftrightarrow 3\mathrm{O}_{\mathrm{O}}^{\mathrm{X}} + 6\mathrm{Mn}_{\mathrm{Mn}}^{\bullet} + \mathrm{V}_{\mathrm{La}}^{'''} + \mathrm{V}_{\mathrm{Mn}}^{'''} \tag{1.22}$$

Oxygen deficient:

$$2\mathrm{Mn}_{\mathrm{Mn}}^{\bullet} + \mathrm{O}_{\mathrm{O}}^{\mathrm{X}} \leftrightarrow 2\mathrm{Mn}_{\mathrm{Mn}}^{\mathrm{X}} + \mathrm{V}_{\mathrm{O}}^{\bullet\bullet} + 1/2\mathrm{O}_2 \tag{1.23}$$

$$2\mathrm{Mn}_{\mathrm{Mn}}^{\mathrm{X}} + \mathrm{O}_{\mathrm{O}}^{\mathrm{X}} \leftrightarrow 2\mathrm{Mn}_{\mathrm{Mn}}^{'} + \mathrm{V}_{\mathrm{O}}^{\bullet\bullet} + 1/2\mathrm{O}_2 \tag{1.24}$$

where $\mathrm{Mn}_{\mathrm{Mn}}^{\bullet}, \mathrm{Mn}_{\mathrm{Mn}}^{\mathrm{X}}$, and $\mathrm{Mn}_{\mathrm{Mn}}^{'}$ are Mn^{4+}, Mn^{3+}, and Mn^{2+} ions, respectively. The electrical conductivity of LSM is expressed by the following equation [13].

$$\delta T = (\delta T)^{O} \exp({-E_a}/{kT}) = A({hv^{O}}/{k})c(1-c)\exp({-E_a}/{kT}) \tag{1.25}$$

where $(\delta T)^o$ is the preexponential constant, E_a is the activation energy, and c represents the ratio of carrier occupancy.

1.2.3.2 Anode materials

Anode is the place where oxygen ion meets hydrogen to produce water vapor, releasing electron to the external circuit. The state-of-the-art anode materials are based on Ni/YSZ cermets. Nickel is an excellent electrocatalyst for electrochemical oxidation of hydrogen and it also acts as an excellent reforming catalyst. It also provides electronic conduction path for the anode. The function of the oxide component (YSZ) is primarily to prevent sintering of the Ni particles maintaining the porosity in the anode of more than 30% by volume, facilitating transport of the reactant gases [14]. The framework of the YSZ can offer an ionic conduction path, effectively broadening the triple phase boundary (TPB) as shown in figure 1-4.

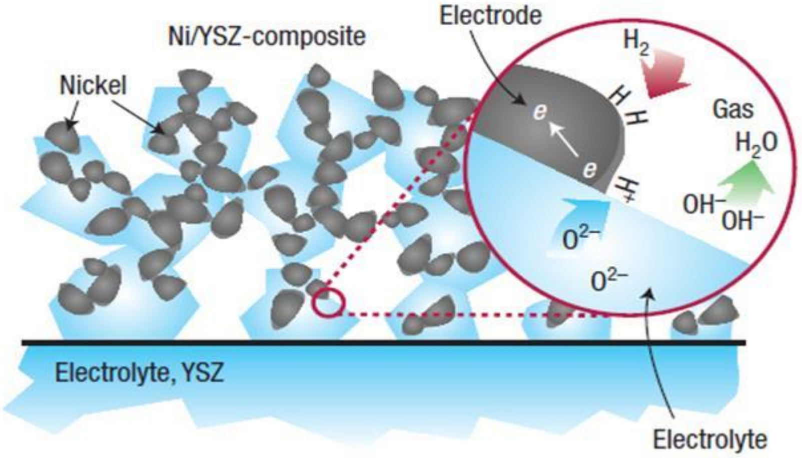

Figure 1-4. Schematic of the electrode reaction sites (TPB) in Ni/YSZ anode [7].

Electrical conductivity of Ni/YSZ strongly depends on the nickel content. Its conductivity a function of nickel content shows the curve predicted by percolation theory as shown in Figure 1-5 [15-17].

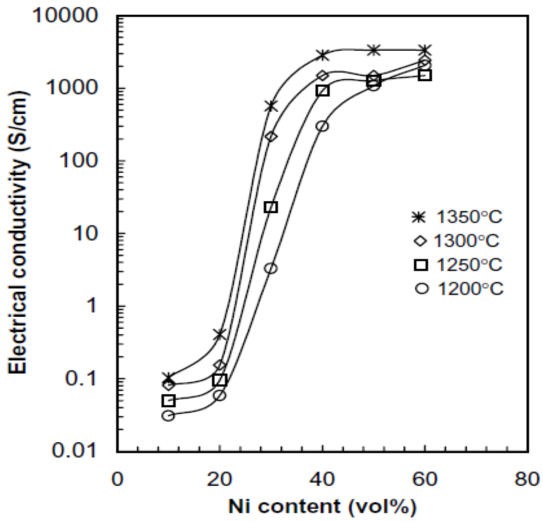

Figure 1-5. Electrical conductivities of Ni/YSZ as a function of Ni concentration for different temperatures [17].

Gadolinia doped ceria (GDC) and scandia doped zirconia (ScSZ) have also been investigated for the oxide material other than YSZ, because characteristic features against carbon deposition or sulfur poisoning can be improved.

1.2.3.3 Electrolyte materials

Ionic conductivity of electrolytes is the most important factor to determine the operating temperature. Relationship between the ionic conductivity and temperature is given by the following equation,

$$\sigma T = A_o \exp[\frac{-(\alpha + \beta T^{-1})}{kT}] \tag{1.26}$$

where σ is the conductivity, T is the temperature, k is the Boltzmann constant, A_o is the pre-exponential constant, α and β are positive constants.

The oxide ion conductivity determines the area specific resistance contributed by the electrolyte. For electron and hole conductivities, the oxygen potential dependence is given by the following equation [18]:

$$\sigma_{electrolyte} = \sigma_e{}^o (P_{O_2}{}^{-1/4}) + \sigma_{hole}{}^o (P_{O_2}{}^{1/4}) \tag{1.27}$$

where σ_e^o, σ_{hole}^o are the normalized contribution of electrons and holes at 1 atm oxygen partial pressure, respectively.

ZrO_2 doped with divalent or trivalent cations of appropriate size is an oxygen-ion conductor. Cubic structure of ZrO_2 is stabilized by substitution of host lattice cation of Zr^{4+} by Y^{3+}. This substitution creates oxygen vacancies by charge compensation according to following equation.

$$Y_2O_3 \rightarrow 2Y'_{Zr} + V_O^{\bullet\bullet} + 3O_O^X \tag{1.28}$$

The high oxygen vacancy concentration gives rise to high oxygen-ion mobility. Oxygen-ion conduction takes place in YSZ by movement of oxygen ions via vacancies. The ionic conductivity of electrolyte material is influenced by several factors such as dopant and dopant concentration, temperature, atmosphere, and nature of grain boundaries.

Among various electrolyte materials, YSZ is the most commonly used because of its stability and cost. YSZ is the oxygen ionic conductor and is generally used for the electrolyte of SOFCs in the temperature range of 700-900 ◦C. GDC has been intensively studied in recent years [19,20]. The electrolyte offer the possibility of lower temperature operation of SOFCs at around 500 ◦C. ScSZ has been investigated as an alternative electrolyte to YSZ, which shows higher ionic conductivities but has a problem of material cost compared to YSZ. Figure 1-6 shows a plot of ionic conductivities of various electrolyte materials.

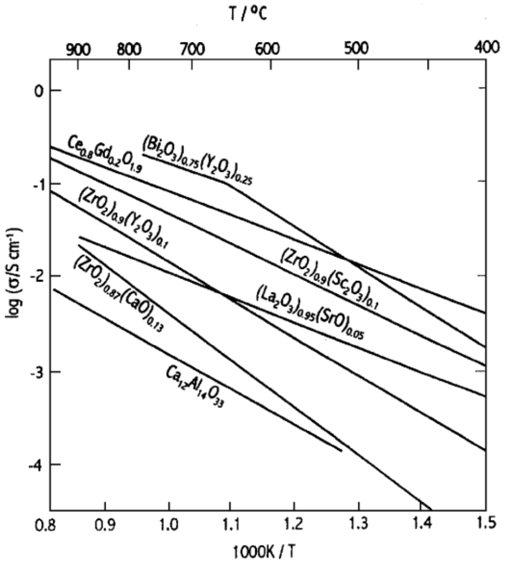

Figure 1-6. Ionic conductivities of different electrolyte materials [21].

1.2.3.4 Interconnector

Interconnector is one of the main components of SOFC. It locates between each individual cell, electrically connecting each cell in series and separating fuel and air in the stack as shown in Figure1-7 [22].

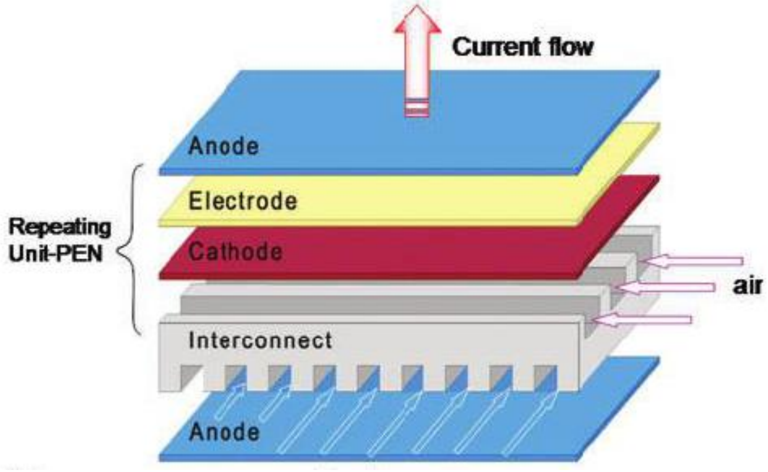

Figure 1-7. Schematic of planar SOFC using interconnector [22].

Interconnector also distributes the fuel/air to anode/cathode and supports the cells under assembling pressure helping to maintain the structural integrity of the SOFC stack. Accordingly, interconnector has to satisfy the requirements of high electrical conductivity, oxidation and reduction resistivity, gas impermeability [22-24]. Ceramic interconnector materials based on lanthanum chromite ($LaCrO_3$) have been considered as proper candidates for interconnector [25,26]. However, it was not applied for planar type interconnector because volume expansion under reduction atmosphere was a severe problem.

Recently, metallic interconnector based on such as stainless steel is widely used because of its high thermal conductivity, high electrical conductivity, high mechanical stability, easy fabrication and low cost.

1.2.3.5 Cell and stack design

The components of SOFCs consist of ceramic materials which are rigid and brittle. Accordingly, there are many types of cell structures depending on the support materials and shapes, in which electrolyte-supported, cathode-supported, anode-supported, ceramic-supported and metal-supported are typical cell designs. The key features of these SOFC configurations are summarized in Table 1-4.

Table 1-4. Five types of cell design and their features.

Cell design	Advantages	Disadvantages
Electrolyte supported-cell	- High mechanical strength because of dense electrolyte - High tolerance to failure such as anode re-oxidation or cathode reduction	- High resistance due to the thickness of the electrolyte - High operating temperatures
Cathode supported-cell	- High tolerance to anode re-oxidation	- Not easy to fabricate electrolyte due to high reactivity - Low mechanical stability
Anode supported-cell	- Low operating temperature - Easy fabrication	- Low tolerance to anode re-oxidation
Ceramic supported-cell (segmented in series type)	- Gas seal and current collector are integrated in one cell-stack - Easy to scale up the systems	- Not easy to fabricate the cell-stack
Metal supported-cell	- Low operating temperature - High mechanical strength - Low cost	- Not easy to fabricate

Two types of cell designs are investigated for SOFC: planar cell as shown in Figure 1-8 and tubular cell as shown in Figure 1-9. The cells are integrated into stack or module to increase the output power up to the required scale. For example, tubular SOFC cells developed by Mitsubishi Hitachi Power Systems Ltd., shown Figure 1-10, have been scaled-up and integrated into a system with capacity of 250 kW. Planar SOFC cells have been deployed in California for many companies such as Google with capacity of 100 kW developed by Bloom Energy.

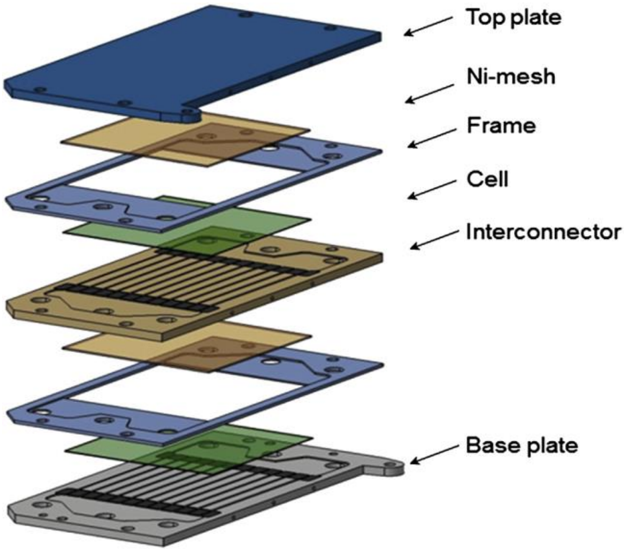

Figure 1-8. Design of planar SOFC stack [27].

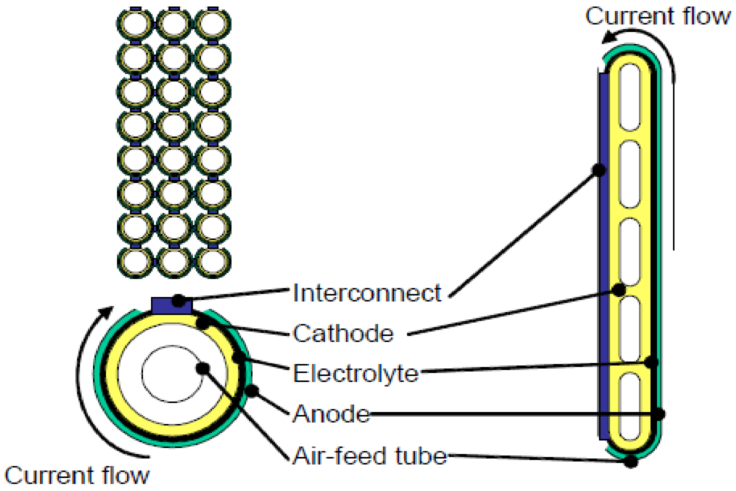

Figure 1-9. Design of cathode supported tubular SOFC stack developed by Westinghouse.

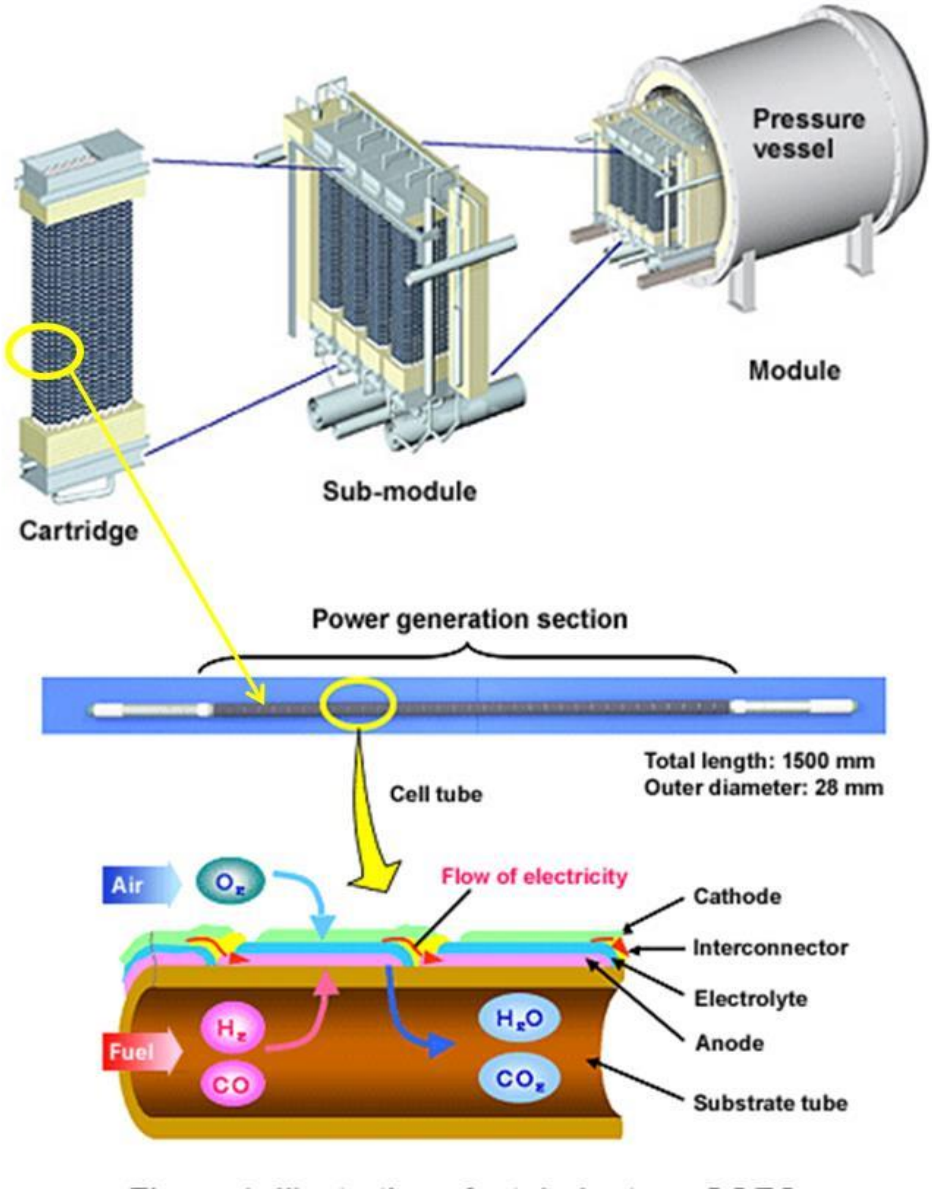

Figure 1-10. Design of tubular SOFC cell and stack developed by Misubishi Hitachi Power Systems [28].

1.3 How to expand SOFC products in the market

SOFC have the potential to replace existing power sources for many applications, such as portable (0 –500 W), stationary (1 –25 kW), and transportation (10 -100 kW) applications with very high efficiency. In the conventional technologies, however, SOFC cell-stack which meets all the requirements has not been realized yet. To develop such SOFCs which can be widely used in many applications, we should solve the issues as follows.

- Rapid start-up is difficult because thermal shock causes crack of the cell-stack.
- Shortage of fuel causes oxidation of nickel in the anode and leads to damage of cell, especially in the case of anode-supported cell.
- Material costs of cell components are high.
- Fabrication costs of cell-stack are high due to the limitation about fabrication methods of ceramic materials.

Metal-supported SOFC (MSC) is the best way to solve the above mentioned issues because metal support materials show high mechanical strength, high thermal conductivity, high electrical conductivity, and have low cost. In this study, we focus on MSC and deal with surface oxide layer of the metal support, which is the most important factor to develop completely new metal support material with high stability.

Reference

[1] W. R. Grove, Phil. Mag., Ser. 3, 14 (1839) 127-130.
[2] W. Nernst, Z. Electrochem., 6 (2) (1899) 41-43.
[3] F. Haber, Austrian Patent 27 743, filed August 5, 1905.
[4] W.D. Treadwell, Z. Electrochem., 22 (1916) 414-421.
[5] E. Baur, H. Preis, Z. Elektrochem, 43 (1937) 727–732.
[6] J. Weissbart, R. Ruka, J. Electrochem. Soc, 109 (1962) 723–726.
[7] B.A. Boukamp, Nat Mater, 2 (2003) 294-296.
[8] S.B. Adler, Chem Rev, 104 (2004) 4791-4843.
[9] C.S. Tedmon, H.S. Spacil, S.P. Mitoff, J. Electrochem. Soc., 116(9) (1969) 1170-1175.

[10] A.N. Petrov, O.F. Kononchuk, A.V. Andreev, V.A. Cherepanov, P. Kofstad, Solid State Ionics, 80(95) (1995) 189–199.

[11] J. a. M. van Roosmalen, E.H.P. Cordfunke, J. Solid State Chem., 110 (1994) 109–112.

[12] J. a. M. Van Roosmalen, E.H.P. Cordfunke, J. Solid State Chem., (1994) 106–108.

[13] H. Kamata, Y. Yonemura, J. Mizusaki, H. Tagawa, K. Naraya, T. Sasamoto, J. Phys. Chem. Solids, 56 (1995) 943-950.

[14] W.Z. Zhu, S.C. Deevi, Mater. Sci. Eng. A, 362(1-2) (2003) 228–39

[15] D.W. Dees, T.D. Claar, T.E. Easler, D.C. Fee, F.C. Mrazek, J. Electrochem. Soc., 134 (1987) 2141-2146.

[16] E.I. Tiffee, W. Wersing, M. Schiebi, H. Greiner, Ber. Bunsen-Ges. Phys. Chem. 94 (1990) 978.

[17] S.K. Pratihar, R.N. Basu, S. Mazumder, H.S. Maiti, in: S.C. Singhal, M. Dokiya (Eds.), ECS trans, 99-19 (1999) 513-517.

[18] H. Yokokawa, N.Sakai, T. Horita, K. Yamaji, M.E. Brito, Electrochemistry, 73 (2005) 20-30.

[19] M. Mogensen, N. M. Sammes and G. A. Tompsett, Solid State Ionics, 129 (2000) 63-94.

[20] B. C. H. Steele, Solid State Ionics, 129 (2000) 95-110.

[21] R.M. Ormerod, Chem. Soc. Rev. 32(1) (2003) 17–28.

[22] Z. Yang, Int. Mater. Rev., 53(1) (2008) 39–54.

[23] Y. Xu, S. Wang, L. Shao, T. Wen, Z. Wen, Int. J. Hydrogen Energy, 36(10) (2011) 6194–6198.

[24] D.N. Boccaccini, O. Sevecek, H.L. Frandsen, I. Dlouhy, S. Molin, M. Cannio, J. Hjelm, P.V. Hendriksen, Mater. Lett. (2015). 10.1016/j.matlet.2015.07.137.

[25] M. Suzukia, H. Sasaki, A. Kajimurab, M. Suzuki, a Kajimura, Solid State Ionics, 96(1-2) (1997) 83–88.

[26] L.F.G. Setz, I. Santacruz, M.T. Colomer, S.R.H. Mello-Castanho, R. Moreno, Mater. Res. Bull., 46(7) (2011) 983–986.

[27] Q. Fang, L. Blum, R. Peters, M. Peksen, P. Batfalsky, D. Stolten, Int. J. Hydrogen Energy, 40(2) (2015) 1128–1136.

[28]https://www.mhps.com/en/technology/business/power/sofc/development_situation.html

Chapter 2

Overview of Metal-Supported SOFC (MSC)

2.1 Merit of metal-supported solid oxide fuel cell

Metal-supported SOFC (MSC) provides many potential advantages such as improving durability against RedOx and thermal shock [1], reducing material costs compared to the conventional ceramic-based ones. Metal supports allow the use of inexpensive metal joining technique and decrease significantly the manufacturing cost of SOFC stacks. High ductility, rigidity and thermal conductivity of the metal support can improve the structural stability as well as prevent the stack failure. Thus, MSC can be fabricated into much more robust SOFC stacks with higher performance with thinner electrolyte. In general, MSCs are regarded as the third generation technologies as shown in Figure 2-1.

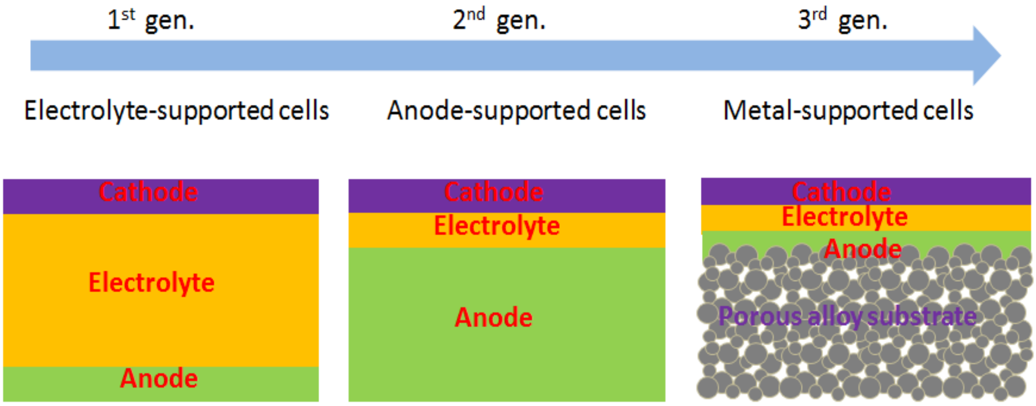

Figure 2-1. Schematic representation of electrolyte-supported cell, anode supported cell, and metal supported cell.

2.2. Summary of literature reviews

2.2.1 Brief history of MSC

MSC was first fabricated by Williams et al. in the 1960s [2]. He deposited zirconia-based electrolyte ($Zr_{0.82}Y_{0.16}O_{2.08}$) onto NiAl alloy as a porous alloy substrate by using flame spray. The porous alloy substrate also had a function as the fuel electrode. The cell was operated in the range of 700–800 °C with power density of about 115 mWcm^{-2} at 750 °C. In the 1990s, MSCs were fabricated by using tubular NiCrAlY

[3] alloy and planar $CrFe_5Y_2O_3$ [4] alloy, which were coated with zirconia-based electrolyte by plasma spray. Power densities of the cells were about 1 Wcm^{-2} at 900 ^oC.

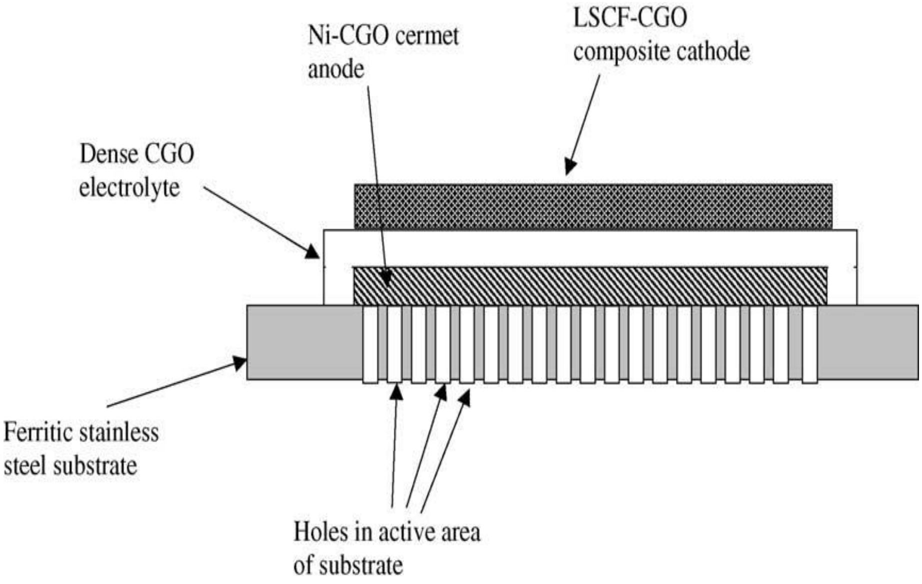

Figure 2-2. Schematic diagram of a metal-supported IT-SOFC developed by Ceres Power Ltd. [5].

After that, Ceres Power Ltd. developed SOFC concept based on a porous stainless steel substrate, using gadolinia doped ceria (GDC or CGO) as the electrolyte material as shown in Figure 2-2. The cell was operated at 500- 600 ◦C with power density of 250-350 $mWcm^{-2}$ [5].

2.2.2 Materials and fabrication processes for MSCs

2.2.2.1 Cathode Layer

$(La,Sr)CoO_3$ (LSC), $(La,Sr)(Co,Fe)O_3$ (LSCF), $(Ba,Sr)(Co,Fe)O_3$ (BSCF) can be used as cathode materials for MSCs [6–13]. These are conventional cathode materials. When we use these materials for the conventional cells (other than MSCs), high temperature sintering (≥ 900 ^oC) in air is required to obtain good adhesion with the electrolyte [8,9,12,13]. The cathode particles grow with increasing sintering temperature, resulting in decrease in active electrode reaction site as shown in Figure 2-3 in the case of LSC [8]. Moreover, with increasing the sintering temperature, Sr tends to segregate from cathode materials to the electrolyte resulting in formation of $SrZrO_3$ which shows low conductivity as shown in Figure 2-4.

In the case of MSCs, we want to apply vacuum process to avoid oxidation of metal support materials. However, high temperature sintering process in a vacuum may damage these conventional cathode materials because they are not stable under low oxygen partial pressure. Therefore, low temperature fabrication process or completely new cathode materials are required for the cathode of MSCs.

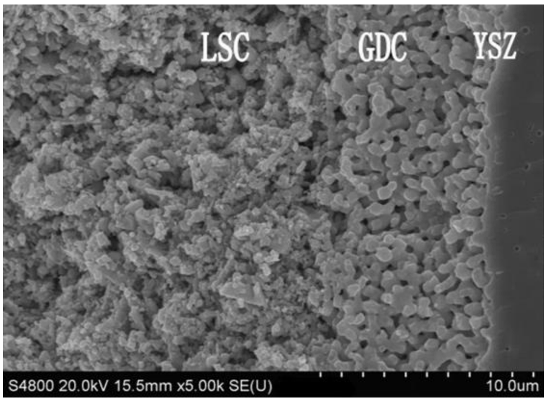

Figure 2-3. Cross-sectional SEM image of LSC cathode/GDC interlayer/YSZ electrolyte. The LSC cathode was sintered at 950 °C [8].

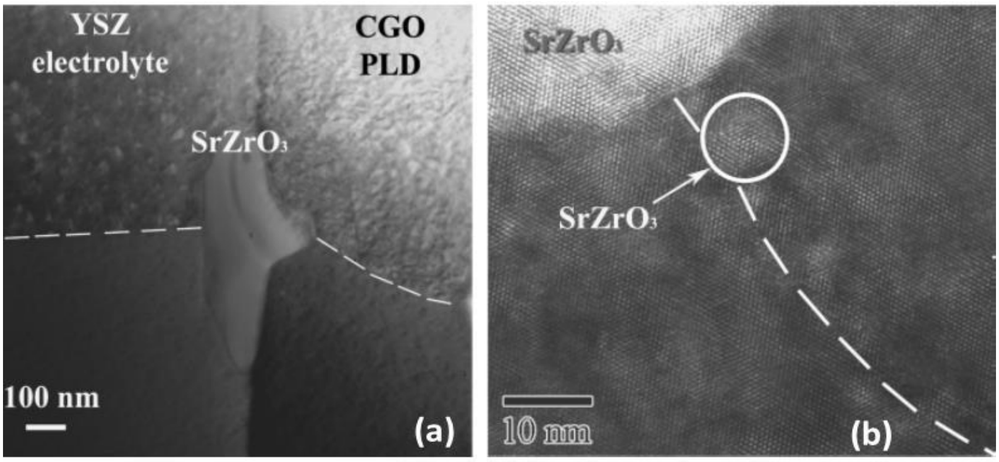

Figure 2-4. (a) $SrZrO_3$ formation at the interface between CGO–PLD barrier layer and YSZ after heat treatment at 1050 °C. (b) Small $SrZrO_3$ grains found at the CGO/YSZ interface [6].

As one possible solution for the above mentioned issues, infiltration method has been proposed as shown in Figure 2-5 [14], in which LSM nanoparticles was infiltrated into a porous YSZ backbone. Triple phase boundary was increased by network of LSM, maintaining match of thermal efficiency coefficient (TEC) between the cathode materials and theYSZ backbone.

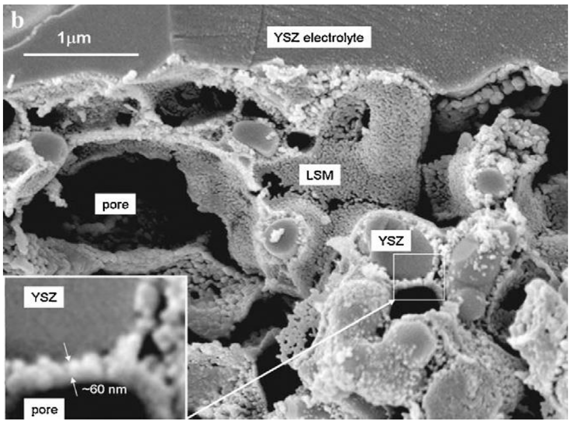

Figure 2-5. SEM micrograph of a fracture surface of a cathode consisting of porous YSZ and infiltrated LSM [14].

2.2.1.2 Anode Layer

Most of the MSC developers have used porous alloy substrates for the anode side to avoid oxidation of metal support during operation. Conventional anode consists of Ni/YSZ and is generally fabricated at high temperature (~ 1300 ^{o}C) in air. In the case of MSCs, however, oxidation of the metal support will be a problem. Thus, vacuum processing for the fabrication of MSCs is widely investigated. When we apply high temperature sintering for the anode, interdiffusion of Ni and the metal support materials may occur, which causes formation of insulating oxides such as $NiCr_2O_4$ with lower oxidation resistance and increase in TEC in the metal support [15-19]. Although diffusion barrier layers between the anode layer and the metal support have been investigated [15,20], the additional barrier layer will increase the total resistance of MSC. Therefore, applying relatively low temperature for the sintering of the anode is one possible solution. However, the performance of the anode prepared at lower temperature is not so stable because Ni grain easily agglomerate and cause decrease in the triple phase boundaries as well as decrease in electrical conduction path consisting of Ni grains. We need to solve the above mentioned issues to obtain high performance and high durability when we develop anodes for MSCs.

2.2.1.3 Electrolyte Layer

Electrolyte layer must be dense and continuous with no crack in order to prevent gas leakage. Furthermore, interface with the electrodes must be well bonded to provide electrode reaction sites, in which oxygen ions can move smoothly and react with gases coming through or moving away the porous electrodes. MSCs have been fabricated with thinner electrolyte to decrease ohmic losses and decrease operating temperature. In the conventional cells, high temperature sintering in air was generally applied. In the case of MSCs, however, there is a problem of oxidation of the metal support. Thus, fabrication of dense electrolyte films on the metal support is one of the most important issues. Several methods were proposed to fabricate dense electrolyte layers, such as atmospheric plasma spray processing, vacuum plasma spraying, pulsed laser deposition, flame-spray, or high temperature sintering in reducing atmosphere.

YSZ is the conventional electrolyte which is commonly used for MSC even its conductivity is not high compared to the other electrolyte materials such as ScSZ, GDC, LSGM as shown in Figure 2-6 [21-23]. YSZ is stable in the operating atmosphere of SOFC and shows pure ionic conductivity which is one of the most important requirements to obtain high efficiency, while GDC exhibits electronic conductivity [21,24–28].

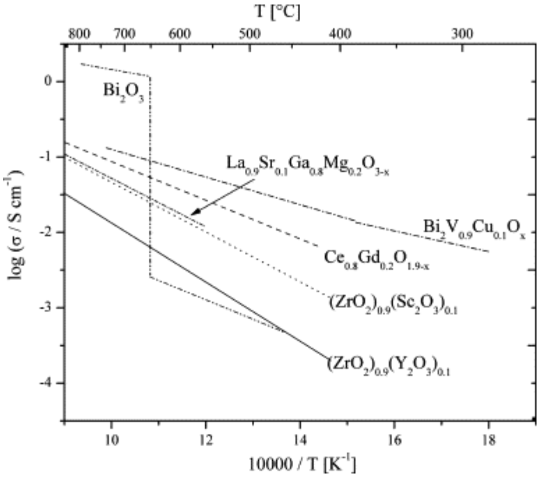

Figure 2-6. Conductivity of various electrolyte materials [21].

2.2.1.4 Porous alloy substrate

There are two ways to fabricate the porous alloy substrate. (i) Sheets made of the alloys are wire cut to form flow channels or laser drilled to create pores. Laser drilling of a preformed sheet provides a smooth, well-defined surface, which facilitates the deposition of thin layers of cell components. On the other hand, this kind of prefabricated sheet does not shrink and is not suitable for sintering process during MSC fabrication [5]. (ii) The other method is extrusion of the alloy powder with binder and other additives [29,30], sometimes with a pore former, and sintering at high temperature in a vacuum. The pore size of the porous alloy substrate can be adjusted by the ratio of binder and alloy powder as shown in Figure 2-7.

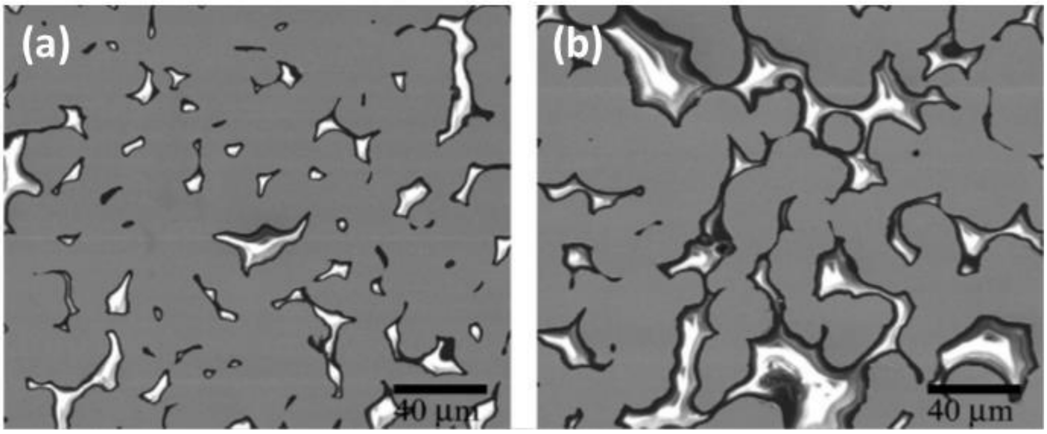

Figure 2-7. SEM of cross-sections of samples, (a) acrylic/PEG = 13/87 wt.%, (b) polymer/alloy = 23/100 wt.%, after sintering at 1573K [29].

There are several types of materials which have been used for MSCs such as pure Ni, Ni-Fe alloy, Ni-Cr based alloys and Fe-Cr based alloys.

Pure Ni metal has been applied for MSCs as a metal support. Cho et al. fabricated a cell using this material, coating Ni/YSZ and YSZ electrolyte, sintering at 1400 °C in a vacuum. The power density was 470 mWcm^{-2} at 800 °C [31]. Ni-Fe alloy was applied for MSCs with various kinds of electrolytes such as LSGM/SDC [32–35] and GDC [36,37] electrolyte. This material is cheaper and lower mismatch TEC from other cell components than pure Ni metal because of additional Fe. However, when we apply this material for MSCs, the main issues are low RedOx tolerance.

Ni-Cr based alloys generally show higher heat resistance than Fe-Cr based alloys. The typical chemical compositions of Ni-Cr based alloys are shown in Table 2.1 [38]. For example, Wang et al. fabricated a cell using this type of materials (Hastelloy X). The anode layer and electrolyte layer were deposited on the alloy by suspension plasma spray, while the cathode layer was deposited on electrolyte layer by screen printing method. The cell exhibited the power density of 216 mWcm^{-2} at 650 °C [39].

Table 2-1. Chemical compositions of Ni-Cr based alloys [38].

Alloy	Concentration/ Wt pct									
	Ni	Cr	Fe	Co	Mn	Mo	Nb	Ti	Si	Al
Inconel 600	Bal.	14-16	6-9		0.4-1			0.2-0.4	0.2-0.5	0.2
ASL 528	Bal.	16	7.1		0.3			0.3	0.2	
Haynes R-41 (Rene 14)	Bal.	19	5	11	0.1	10		3.1	0.5	1.5
Inconel 718	Bal.	22	18	1	0.4	1.9				
Haynes 230	Bal.	22-26	3	5	0.5-0.7	1-2			0.3	
Hastelloy X	Bal.	24	19	1.5	1.0	5.3				
Inconel 625	Bal.	25	5.4	1.0	0.6	5.7				
Nicrofer 6025 HT	Bal.	25	9.5		0.1	0.5			0.5	0.15
Hastelloy G-30	Bal.	30	1.5	5	1.5	5.5	1.5	1.8	1	

Fe-Cr based alloys are body-centered cubic, ferromagnetic alloys containing mainly iron and chromium. The typical chemical compositions of the alloys are shown in Table 2.-2. The alloys have widely been used for furnace, automotive exhaust manifolds and mufflers. The alloys are inexpensive, show high heat resistance and show electrical conductivity at the surface oxide layer of Cr_2O_3 at high temperature as shown in Figure 2-8 [40]. When we apply this type of alloy, the main issues are (i) corrosion resistance in a long-term operation, (ii) chromium diffusion (contamination) to the electrodes, (iii) interdiffusion of Ni from the anode and Cr from the metal support. The chromium diffusion (ii) to the anode may cause the formation of chromium oxide scale on nickel catalyst surface as shown in Figure 2-9. This leads to the degradation of cell performance. The interdiffusion of Ni and Cr (iii) causes decrease of oxidation resistance and change in TEC [18,19], which are detrimental to cell performance and durability [15,20]. In order to suppress the interdiffusion, $SrTiO_3$ [16] or Ni-GDC [20] was infiltrated into porous alloy substrate as shown in Figure 2-10.

Table 2-2. Chemical compositions of Fe-Cr based alloys [38].

Alloy	Concentration/ Wt pct										
	Fe	Cr	Mn	Mo	W	Si	Al	Ti	Y	Zr	La
Fe-10Cr	Bal.	10	<0.02		<0.01						
1.4724	Bal.	13					1				
SUS 430	Bal.	16-17	0.2-1			0.4-1	≤0.2				
Fe-17Cr-0.2Y	Bal.	17							90.2		
1.4016	Bal.	17									
Ferrotherm (1.4742)	Bal.	17-18	0.3-0.7		0.8-0.9	0.9-1					
Fe-18Cr-9W	Bal.	18			9						
Fe-18Cr-7W	Bal.	20			7	0.3	0.6			0.3	
Fe-20Cr	Bal.	20	<0.02		<0.01					0.2	0.04
AL 453	Bal.	22	0.3		0.3	0.6	0.02				0.01
1.4763 (446)	Bal.	24-26	0.7-1.5	≤0.05		0.4-1		<0.05			
FeCRMn (LATi)	Bal.	16-25									
Fe-Cr-Mn	Bal.	16-25									
Fe-25Cr-DIN 50049	Bal.	25	0.3		0.7		0.01				
Fe-25Cr-0.1Y-2.5Ti	Bal.	25						2.5	0.1		
Fe-25Cr-0.2Y-1.6Mn	Bal.	25	16						0.2		
Fe-25Cr-0.4La	Bal.	25									0.4
Fe-25Cr-0.3Zr	Bal.	25								0.3	
Fe26CrTiY	Bal.	26	0.1	<0.02		<0.05	<0.05	0.3	0.4		
Fe26CrTiNbY	Bal.	26	Composition not provided, but presumably same as Fe26CrTiY with Nb								
Fe26CrMoTiY	Bal.	26	0.1	2	<0.05	<0.05	0.3	0.3			
E-Brite	Bal.	26-27	≤0.1	1	0.03-0.2	≤0.05	≤0.05	≤0.01			
Al29-4C	Bal.	27	0.3	4	0.3						
Fe-30Cr	Bal.	30	<0.02		<0.1						

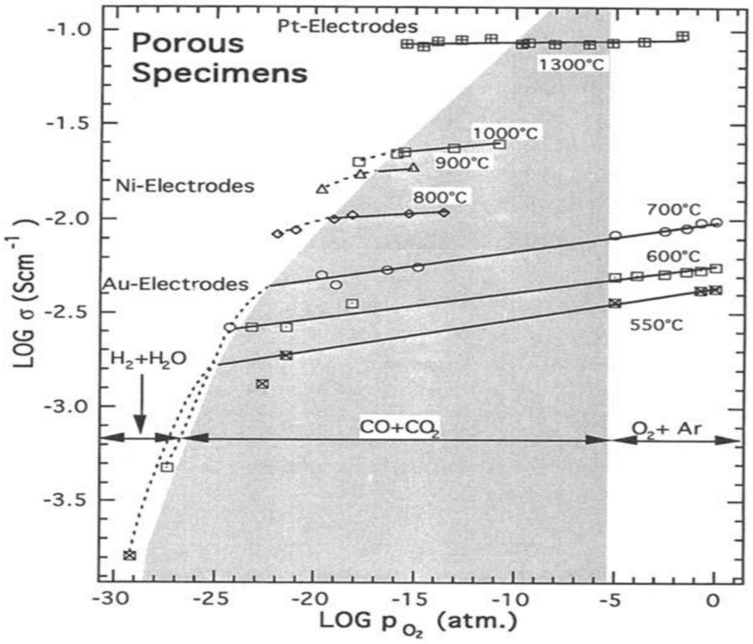

Figure 2-8. Electrical conductivity of chromium oxide as a function of the partial pressure of oxygen at temperatures from 550 to 1300 °C [40].

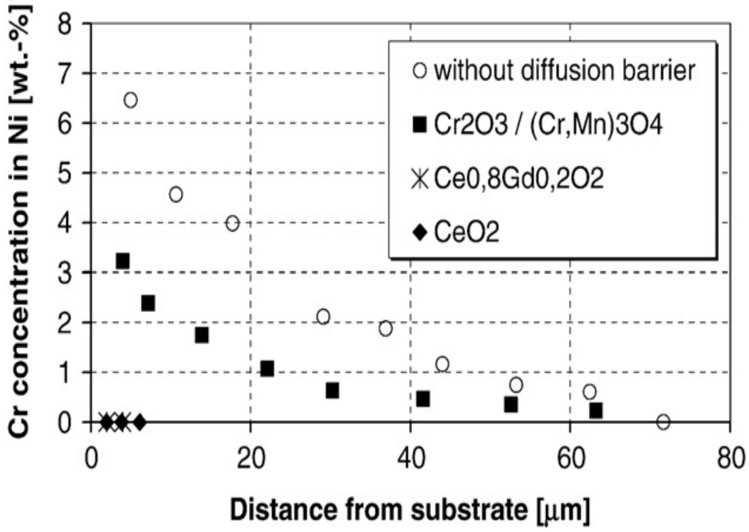

Figure 2-9. Quantitative diffusion profiles of chromium in nickel with and without a diffusion barrier between the CroFer22APU substrate and the nickel [19].

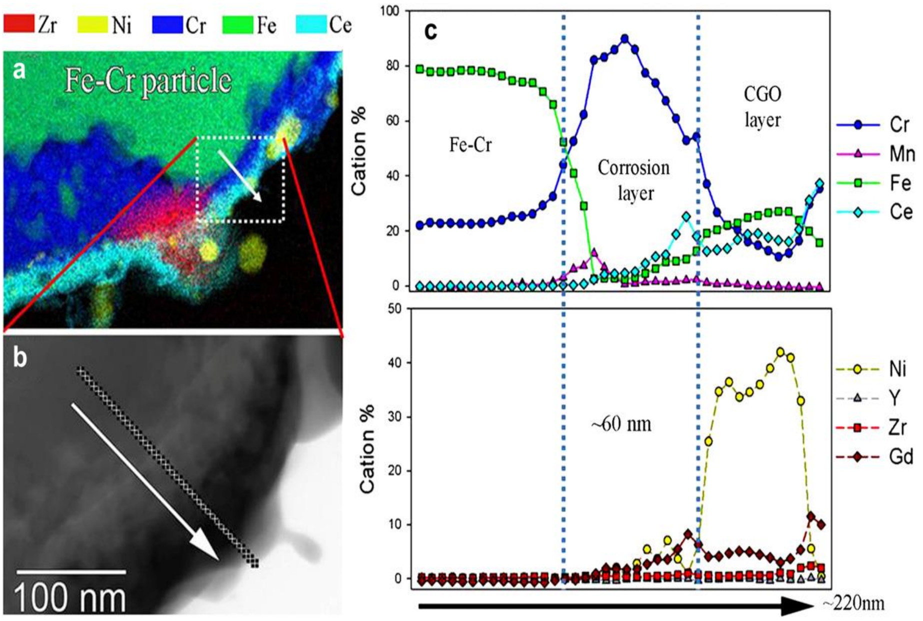

Figure. 2-10. (a) STEM-EDS of GDC-Ni on FeCr alloy, (b) BF-STEM micrograph of the box in (a) illustrating the position of line scan EDS, and (c) the resulting concentration profile [20].

Formation of barrier layers is another solution to prevent the interdiffusion while allowing electron and gas transport, having similar TEC to the other cell components. They should be stable and maintain high performance during cell operation. The properties of possible barrier layer materials are listed in Table 2.3.

Table 2-3. Electronic conductivity of barrier layer.

Material	Electronic conductivity [S/cm]			References
	700 °C	800 °C	900 °C	
Cr_2MnO_4	2.4×10^{-4}	2.3×10^{-3}	6.2×10^{-3}	[41]
$Ce_{0.8}Gd_{0.2}O_{1.9}$	0.047			[42]
CeO_2		0.89	2.3	[43]

2.3 Fabrication of MSCs

There are three critical issues concerning fabrication of MSCs which affect the performance and durability as shown in Table 2-4. (i) In order to avoid oxidation or melting of the porous alloy substrate during fabrication process of the electrolyte layer, annealing in a vacuum at lower temperature than the conventional technologies is required. (ii) Shrinkage of the porous alloy substrate during fabrication process should be matched to the other layers of the cell. (iii) Good adhesion and mechanical strength should be maintained among the porous alloy substrate, electrodes and electrolyte.

Many fabrication processes of MSCs have been developed, such as atmospheric vacuum plasma spraying [44,45], pulsed laser deposition [46], plasma spray processing [47,48], however these processes are very expensive compared to the conventional process (sintering at high temperature in air).

Table 2-4. Example of performance of MSCs integrating porous alloy substrate measures at 0. 7 V in air/H_2.

Porous alloy substrate	Anode	Electrolyte	Cathode	Other layer	Power density at 0.7V in W/cm^2	Remark and References
Fe-Cr	Ni/YSZ	YSZ	LSM/YSZ		0.21 at 800 ^{o}C	[1]
Fe-Cr	Fe22Cr-YSZ	ScYSZ	LSCF-CGO	-	0.4 at 650 ^{o}C	Infiltration of NiO-CGO, Second cathode layer LSC [49]
Ti-Nb (Fe-17Cr Sheet	NiO-GDC	GDC EPD	Doped $LaFeO_3$/ GDC	-	0.22 at 600 ^{o}C	In situ sintering of cathode [50]
Hastelloy X Sheet	NiO-SDC SPS	SDC SPS	SSCo-SDC	-	0.11 at 600 ^{o}C	In situ sintering of cathode [51]
Hastelloy X Sheet	NiO-SDC	SDC	SSCo-SDC	-	0.11 at 650 ^{o}C 0.08 at 600 ^{o}C	In situ sintering of cathode [52]
Hastelloy X Sheet	NiO-SDC	SDC	SSCo-SDC	-	0.53 at 650 ^{o}C 0.35 at 600 ^{o}C	In situ sintering of cathode [53]
ITM Sheet	NiO/YSZ	YSZ	LSM/ LSCF	$La_{0.6}Sr_{0.2}Ca_{0.2}O_3$	0.36at 800 ^{o}C	[54]
Fe-Cr	YSZ	ScYSZ	LSCF/CGO		0.1 at 650 ^{o}C	Infiltrated with CGO and Ni [21]
NiFe	NiO-YSZ	YSZ	LSCF		0.9 at 800 ^{o}C	[55]

2.4 Key issues associated with commercialization of MSCs

MSCs are expected to significantly decrease material costs, improve durability against RedOx and thermal shock. Despite these potential advantages, durability of metal support such as corrosion, oxidation behavior has been major issues for commercialization of MSCs. Volatility of Cr from the metal support and diffusion to the electrode is also a serious problem. The advantages and the key issues of MSCs are summarized in Table 2-5.

Table 2-5. Advantages and key issues of MSCs.

Advantages	Issues to be solved
- High durability against RedOx and thermal shock (--> Higher fuel utilization and rapid start-up) - Low material costs	- Corrosion and oxidation of metal support - Cr poisoning to electrode materials - Fabrication processes should be developed

2.5 Our study

Our objective and contents is illustrated in Figure 2-11. We selected a material of Fe-Cr-Al alloy for the cathode side of MSC, which generally shows high oxidation resistance in air because of the formation of mainly alumina-based oxide layer on the surface as a protective layer. This layer can prevent chromium poisoning to electrode materials because alumina layer can suppress chromium diffusion. This type of alloy has not been considered as a candidate material for MSC because of the high electrical resistance of the alumina layers.

We have fabricated a porous alloy substrate using the alloy and investigated the conditions to decrease electrical resistance between the porous alloy substrate and the cathode materials at high temperature in air. We analyzed the elemental composition, crystal structure, and microstructure of the surface oxide layer which shows high oxidation resistance and high electrical conductivity and investigated mechanism of growth of such an oxide layer in Chapter 4. We investigated the optimum chemical composition and crystal structure to obtain the lowest electrical resistance in Chapter 5. We also evaluated the durability of the alloy by accelerating the growth of the surface oxide layer (interfacial layer) in Chapter 6.

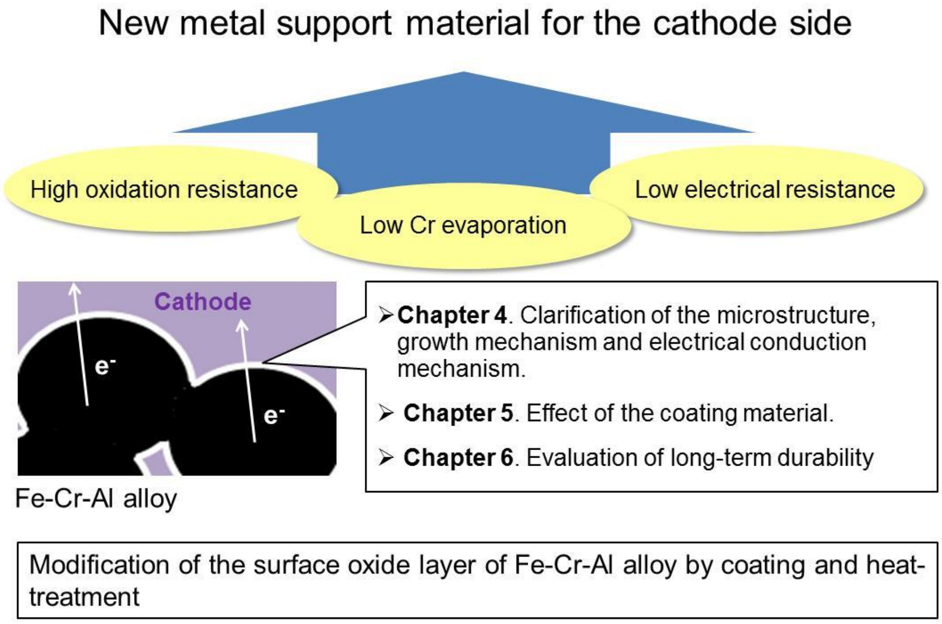

Figure 2-11. The objective and contents of this study.

References

[1] M.C. Tucker, G.Y. Lau, C.P. Jacobson, L.C. DeJonghe, S.J. Visco, J. Power Sources 171(2) (2007) 477.

[2] K.R. Williams, J.G. Smith, US Pat. (1969) 3.

[3] M.K. A.Momma,Y. Kaga, T. Okuo, K. Fujii, K. Hohjyo, Bull. Electrotechn. Lab. 63 (1999) 103.

[4] S.S. G. Schiller, R.H. Henne, M. Lang, R. Ruckdaschel, Fuel Cells Bull. 3 (21) (2000) 7.

[5] R.T. Leah, N.P. Brandon, P. Aguiar, J. Power Sources 145(2) (2005) 336.

[6] R. Knibbe, J. Hjelm, M. Menon, N. Pryds, M. Søgaard, H.J. Wang, K. Neufeld, J. Am. Ceram. Soc. 93(9) (2010) 2877.

[7] R. Küngas, F. Bidrawn, J.M. Vohs, R.J. Gorte, Electrochem. Solid-State Lett. 13(8) (2010) B87.

[8] Y. Tao, J. Shao, W.G. Wang, J. Wang, Fuel Cells 9(5) (2009) 679.

[9] C. Torres-Garibay, D. Kovar, A. Manthiram, J. Power Sources 187(2) (2009) 480.

[10] N. Jordan, W. Assenmacher, S. Uhlenbruck, V. a C. Haanappel, H.P. Buchkremer, D. Stöver, W. Mader, Solid State Ionics 179(21-26) (2008) 919.

[11] M. Sase, D. Ueno, K. Yashiro, A. Kaimai, T. Kawada, J. Mizusaki, J. Phys. Chem. Solids 66(2-4) (2005) 343.

[12] F. Zhao, L. Zhang, Z. Jiang, C. Xia, F. Chen, J. Alloys Compd. 487(1-2) (2009) 781.

[13] Y.M. Kim, P. Kim-Lohsoontorn, J. Bae, J. Power Sources 195(19) (2010) 6420.

[14] T.Z. Sholklapper, C. Lu, C.P. Jacobson, S.J. Visco, L.C. De Jonghe, Electrochem. Solid-State Lett. 9(8) (2006) A376.

[15] M.C. Tucker, J. Power Sources 195(15) (2010) 4570.

[16] P. Blennow, B.R. Sudireddy, Å.H. Persson, T. Klemensø, J. Nielsen, K. Thydén, Fuel Cells 13(4) (2013) 494.

[17] I. Antepara, I. Villarreal, L.M. Rodríguez-Martínez, N. Lecanda, U. Castro, A. Laresgoiti, J. Power Sources 151(1-2) (2005) 103.

[18] C. Hwang, C.-H. Tsai, C.-L. Chang, C.-M. Chuang, Z.-Y.C. Shie, S.-W. Cheng, S.-H. Wu, Thin Solid Films 570 (2014) 6.

[29] M. Brandner, M. Bram, J. Froitzheim, H.P. Buchkremer, D. Stöver, Solid State Ionics 179(27-32) (2008) 1501.

[20] R. Knibbe, H.J. Wang, P. Blennow, K. Thydén, Å.H. Persson, L. Mikkelsen, T. Klemensø, J. Power Sources 228 (2013) 75.

[21] D. Beckel, A. Bieberle-Hütter, A. Harvey, A. Infortuna, U.P. Muecke, M. Prestat, J.L.M. Rupp, L.J. Gauckler, J. Power Sources 173(1) (2007) 325.

[22] R.M. Ormerod, Chem. Soc. Rev. 32(1) (2003) 17.

[23] V. V. Kharton, F.M.B. Marques, A. Atkinson, Solid State Ionics 174(1-4) (2004) 135.

[24] C. Kleinlogel, L.J. Gauckler, Solid State Ionics 135(1-4) (2000) 567.

[25] M. Gödickemeier, J. Electrochem. Soc. 144(5) (1997) 1635.

[26] D. Schneider, M. Godickemeier, L.J. Gauckler, J. Electroceramics 1(2) (1997) 165.

[27] I. Riess, M. Godickemeier, L.J. Gauckler, Solid State Ionics 90(1-4) (1996) 91.

[28] I. Riess, Solid State Ionics 157(1-4) (2003) 1.

[29] H. Kurokawa, G.Y. Lau, C.P. Jacobson, L.C. De Jonghe, S.J. Visco, J. Mater. Process. Technol. 182(1-3) (2007) 469.

[30] H.-C. Pham, S. Taniguchi, Y. Inoue, J.-T. Chou, T. Izumi, K. Matsuoka, K. Sasaki, J. Power Sources 297 (2015) 181.

[31] H.J. Cho, G.M. Choi, Solid State Ionics 180(11-13) (2009) 792.

[32] T. Ishihara, J. Yan, M. Enoki, S. Okada, H. Matsumoto, J. Fuel Cell Sci. Technol. 5(3) (2008) 31205.

[33] Y.-W. Ju, ECS Trans. 25(2) (2009) 719.

[34] J. Yan, M. Enoki, H. Matsumoto, T. Ishihara, Electrochem. Solid-State Lett. 10(9) (2007) B139.

[35] T. Ishihara, J. Yan, M. Shinagawa, H. Matsumoto, Electrochim. Acta 52(4) (2006) 1645.

[36] G. Lee, Younki, Choi, ECS Trans. 25 (2) (2009) 727.

[37] H.C. Park, A. V. Virkar, J. Power Sources 186(1) (2009) 133.

[38] J.W. Fergus, Mater. Sci. Eng. A 397(1-2) (2005) 271.

[39] Z. Wang, J.O. Berghaus, S. Yick, C. Decès-Petit, W. Qu, R. Hui, R. Maric, D. Ghosh, J. Power Sources 176(1) (2008) 90.

[40] A. Holt, P. Kofstad, Solid State Ionics 69(2) (1994) 137.

[41] N. Sakai, T. Horita, Y.P. Xiong, K. Yamaji, H. Kishimoto, M.E. Brito, H. Yokokawa, T. Maruyama, Solid State Ionics 176(7-8) (2005) 681.

[42] B. Steele, Solid State Ionics 129(1-4) (2000) 95.

[43] I.K. Naik, T.Y. Tien, J. Electrochem. Soc. 471 (1975) 562.

[44] M. Lang, T. Franco, G. Schiller, N. Wagner, J. Appl. Electrochem. 32(8) (2002) 871.

[45] G. Schiller, A. Ansar, M. Lang, O. Patz, J. Appl. Electrochem. 39(2) (2009) 293.

[46] S. (Rob) Hui, D. Yang, Z. Wang, S. Yick, C. Decès-Petit, W. Qu, A. Tuck, R. Maric, D. Ghosh, J. Power Sources 167(2) (2007) 336.

[47] R. Vaßen, D. Hathiramani, J. Mertens, V.A.C. Haanappel, I.C. Vinke, Surf. Coatings Technol. 202(3) (2007) 499.

[48] R. Vaßen, H. Kaßner, A. Stuke, F. Hauler, D. Hathiramani, D. Stöver, Surf. Coatings Technol. 202(18) (2008) 4432.

[49] P. Blennow, J. Hjelm, T. Klemensø, S. Ramousse, A. Kromp, A. Leonide, A. Weber, J. Power Sources 196(17) (2011) 7117.

[50] N.P. Brandon, D. Corcoran, D. Cummins, A. Duckett, K. EI-Khoury, D. Haigh, R. Leah, G. Lewis, N. Maynard, T. McColm, R. Trezona, A. Selcuk, M. Schmidt, J. Mater. Eng. Perform. 22(10) (2013) 2900.

[51] Q. a. Huang, J. Oberste-Berghaus, D. Yang, S. Yick, Z. Wang, B. Wang, R. Hui, J. Power Sources 177(2) (2008) 339.

[52] Z. Wang, J.O. Berghaus, S. Yick, C. Decès-Petit, W. Qu, R. Hui, R. Maric, D. Ghosh, J. Power Sources 176(1) (2008) 90.

[53] R. Hui, J.O. Berghaus, C. Decès-Petit, W. Qu, S. Yick, J.G. Legoux, C. Moreau, J. Power Sources 191(2) (2009) 371.

[54] M. Marr, C. Metcalfe, E.S.C. Fan, O. Kesler, ECS Electrochem. Lett. 2(11) (2013) F85.

[55] K.H. Kim, Y.M. Park, H. Kim, Energy 35(12) (2010) 5385.

Chapter 3

Experimentation

3.1 Fabrication of porous alloy substrate for the measurement of heat resistance and contact resistance

Porous alloy substrates were fabricated using a powder of commercially available Fe-Cr-Al alloy (HRE5, Hitachi Metals Ltd.). The chemical composition of the alloy is given in Table 3-1.

Table 3-1. Chemical composition of the Fe-Cr-Al alloy used in this study.

	Cr	Al	Ti	Si	Mn	Ni	Fe
wt.%	23	5.0	0.2	0.4	0.01	0.2	Balance

The particle sizes in the alloy powder ranged from 38 to 125 μm. The porous alloy substrate was fabricated as shown in Figure 3-1 by mixing the alloy powder with ethanol (as a solvent), ethylcellulose (as a binder) and other additives, pressing under a pressure of 55 MPa, and annealing at 1280 °C for 4 h under a reducing pressure. This condition was determined to control the sintering process and obtain a porous alloy substrate with a good mechanical strength, a high electrical conductivity, and gas permeability. In this study, we selected cylindrical shape just for material characterization, although various shapes (planar, tubular) should be considered when we evaluate practical performance of the metal supported cell. Cross-sectional microstructure of the porous alloy substrate is shown in Figure 3-2.

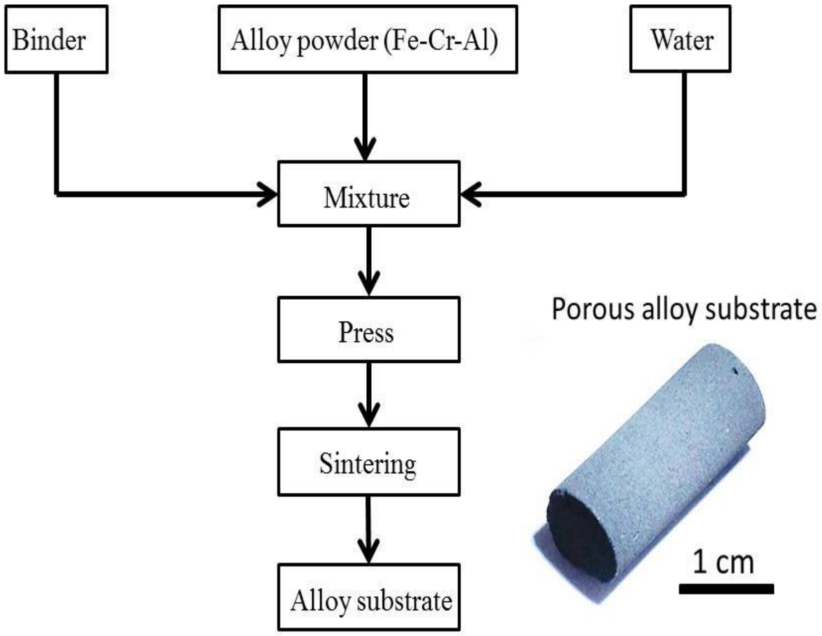

Figure 3-1. Fabrication procedure and appearance of the porous alloy substrate for the measurement of heat resistance and contact resistance.

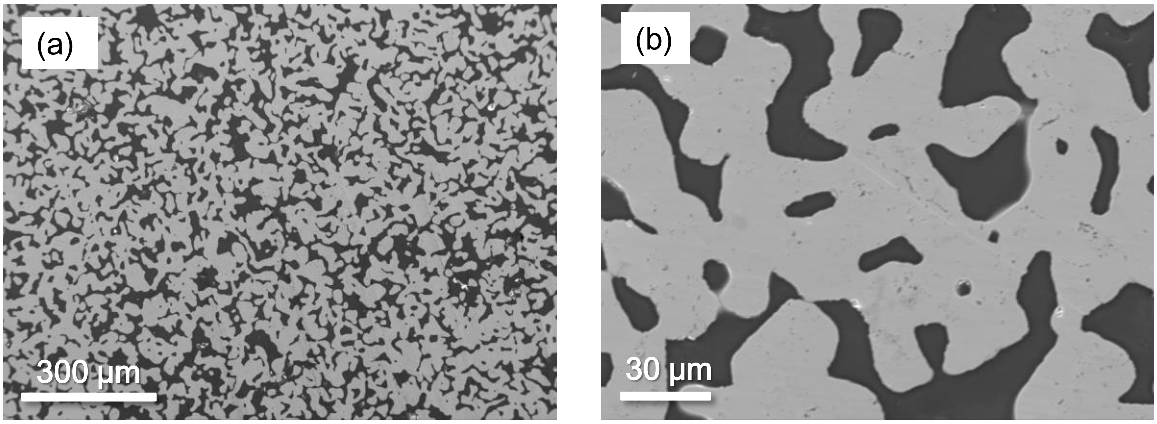

Figure 3-2. Cross-sectional SEM images of the porous alloy substrate at different magnifications.

We also used non-porous rod (8 mm φ) made of the same Fe-Cr-Al alloy to evaluate area specific resistance and weight increase by oxidation.

3.2 Measurement of the electrical resistance in the surface oxide layer

In this study, electrical resistance in the surface oxide layer of the alloy is defined as "interfacial resistance" and it is measured in the configuration shown in Figure 3-3, because it dominates the resistance in the circuit. The interfacial resistance of porous alloy substrate and non-porous alloy substrate were measured using cathode materials as the electrodes, and platinum mesh and wire for the current collector in a furnace as shown in Figure 3-4. The interfacial resistance was calculated by using an apparent electrode area. A cylindrical shape was selected to avoid detachment of the current collector during the measurement.

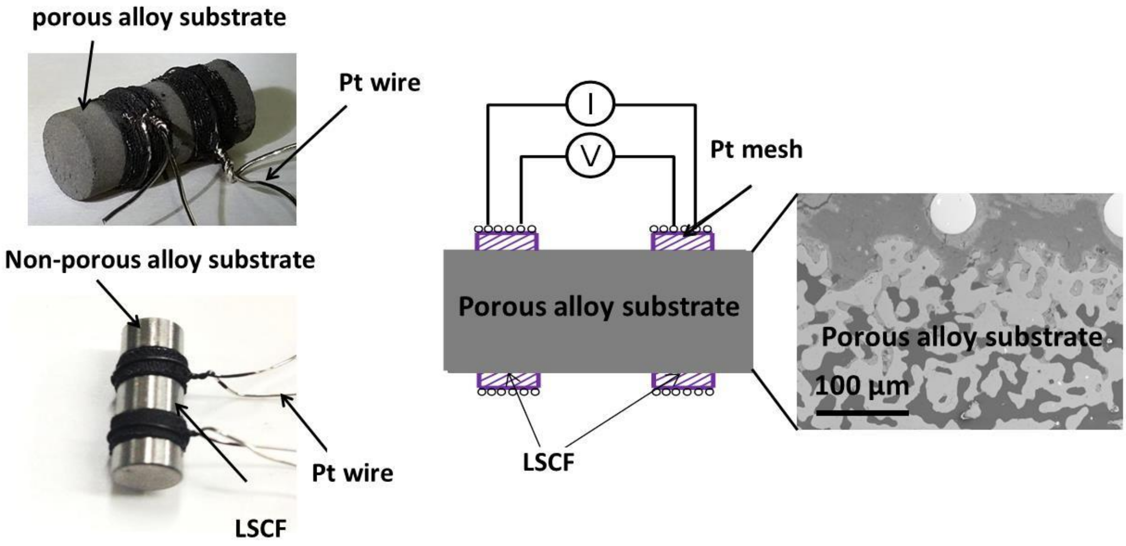

Figure 3-3. Setup for the measurement of the interfacial resistance of the alloy-coated LSCF.

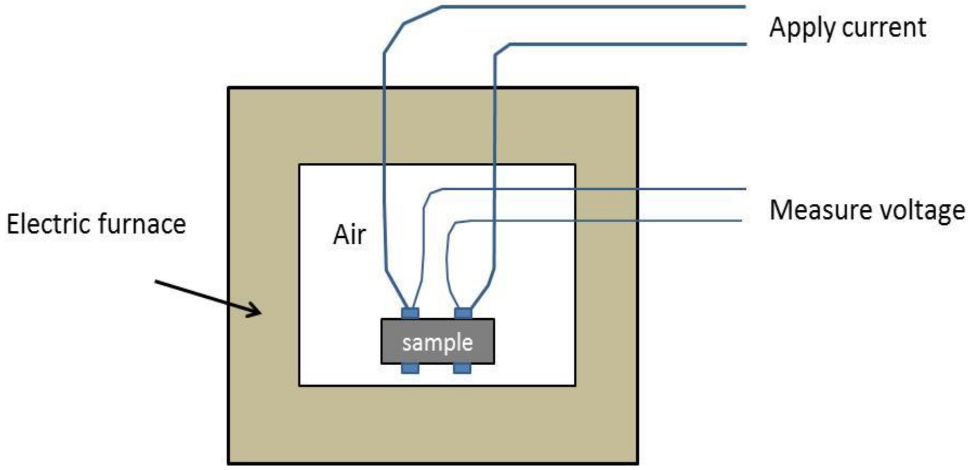

Figure 3-4. Measurement of the interfacial resistance of the sample in an electric furnace.

3.3 Evaluation of oxidation resistance

We evaluated oxidation resistance of the alloy by the weight gain of the alloy in air. The weight gain of the sample was measured after the sample was exposed in an electrical furnace. Figure 3-5 shows an example of the weight gain of the alloy at 700 °C in air.

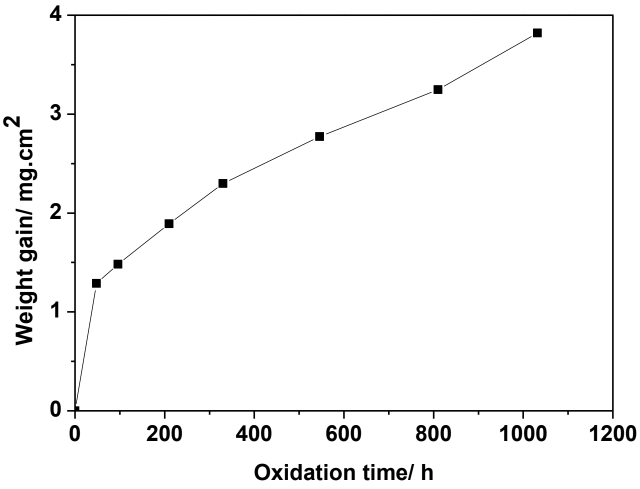

Figure 3-5. Weight gain at 700°C in air as a function of time.

3.4 Material characterization by microscopic analysis

3.4.1 Sample preparation for micromachining by focused ion beam (FIB)

We prepared the sample for FIB micromachining as shown in Figure 3-5. The samples after the measurement of heat resistance and contact resistance were embedded in an epoxy resin. Two types of chemical precursor (liquids) of epoxy resin were mixed and filled in a cup with the sample. The sample in the liquid was evacuated in a desiccator for a few minutes to remove the air from the epoxy resin and left for about 12 h before hardening. Then, the sample was cut by a low-speed cutting machine, and the cross-section of the sample was polished to obtain a smooth surface by polishing machine. Finally, the sample was cut into a smaller one (4 mm × 4 mm × 1 mm) by cutting machine for FIB micromachining.

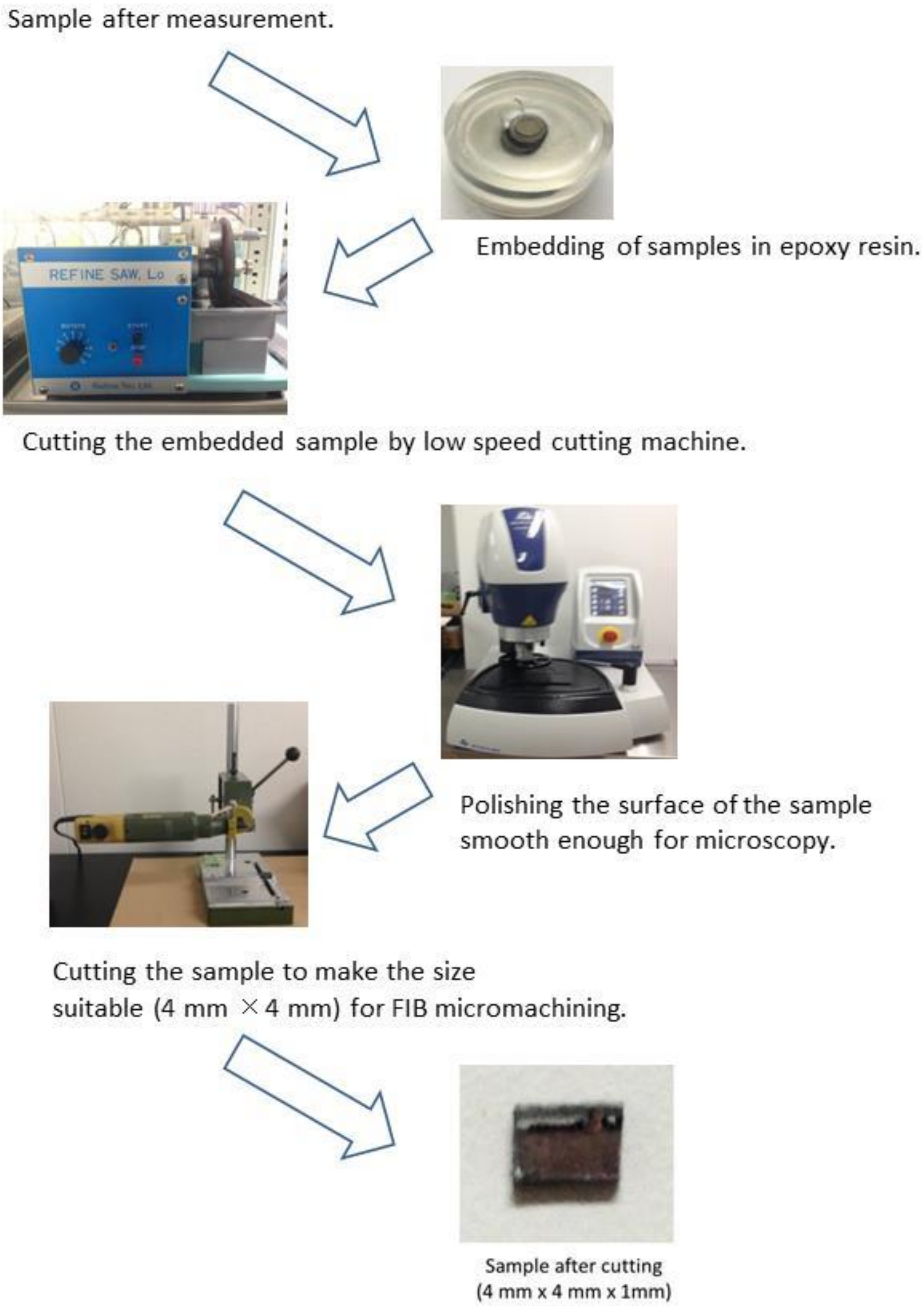

Figure 3-5. Procedure of preparation of the sample for FIB micromachining.

3.4.2 Micromachining by focused ion beam (FIB)

The focused ion beam (FIB) micromachining has been widely used for high resolution microscopy as shown in Figure 3-6. In most commercially available systems, Ga ions are used, and their sputtering action enables precise machining of the samples. In this study, FIB micromachining system (Hitachi High-Tech FB-2100) was utilized to pick up a micrometer-size area (~5 µm × 5 µm) and machine the sample to a thickness (<100 nm) suitable for STEM and TEM analysis. Figure 3-7 shows the sample prepared by the FIB micromachining.

Figure 3-6. The FIB micromachining system (Hitachi High-Tech FB-2100).

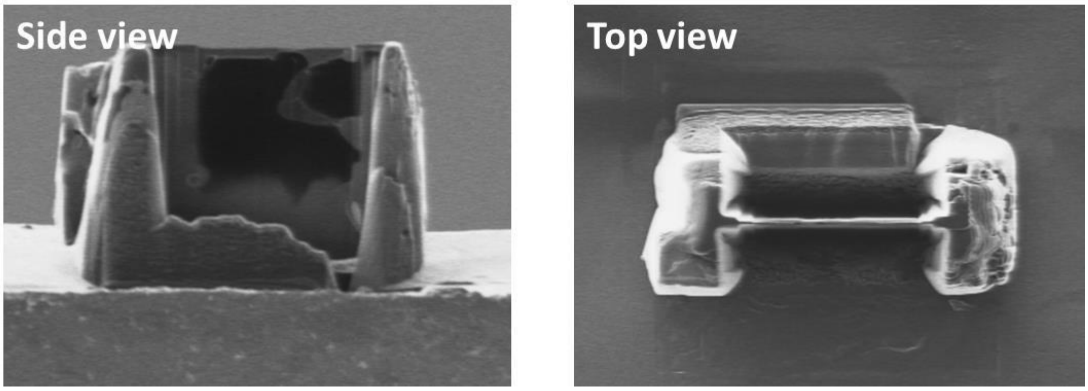

Figure 3-7. STEM sample prepared by FIB.

After the FIB micromachining, the sample should be kept in a vacuum using a desiccator (shown in Figure 3-8) to prevent contamination before high resolution transmission electron microscope (HRTEM) analysis.

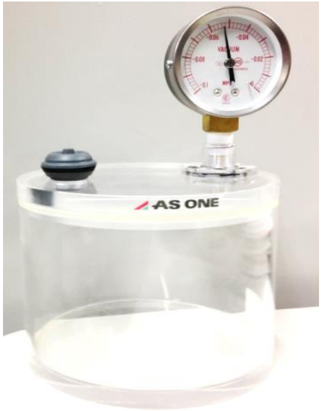

Figure 3-8. Desiccator for keeping samples in a vacuum.

3.4.3 Observation by SEM and STEM

Scanning electron microscope (SEM) images the sample surface by scanning it with a high-energy beam of electrons in a raster scan pattern. The electron interacts with the atoms that make up the sample producing signals that containing information about the sample’s surface topograph, composition, and other properties. SEM with field emission gun (FE-SEM) exhibits significantly improved signal-to-noise ratio and spatial resolution than the normal SEM (tungsten type), and greatly increased emitter life and reliability compared with thermionic devices have been achieved. In this study, the surface oxide layer of the alloy was analyzed using FE-SEM (JEOL JSM-7001F) as shown in Figure 3-9.

Figure 3-9. Field emission scanning electron microscope (FE-SEM).

A scanning transmission electron microscope (STEM) is focusing the electron beam into a narrow spot which is scanned over the sample in a raster. The rastering of the beam across the sample makes these microscopes suitable as analysis techniques for mapping by energy dispersive X-ray (EDX) spectroscopy. These signals can be obtained simultaneously, allowing direct correlation of image and quantitative data. By using a STEM and a high-angle detector, it is possible to form atomic resolution images where the contrast is directly related to the atomic number (Z-contrast image). In this study, the surface oxide layer of the alloy was analyzed by STEM-EDX (Hitachi 200-kV dedicated STEM HD-2300A equipped with an EDAX Si(Li) EDX detector as shown in Figure 3-10) and transmission electron microscopy (TEM; JEOL JEM-ARM200F located at Next-Generation Fuel Cell Research Center and The Ultramicroscopy Research Center).

Figure 3-10. Scanning transmission electron microscope (STEM).

3.4.4 Analysis of crystal structure by electron beam diffraction

Electron beam diffraction is used to study crystal structure of a small and thin sample, usually prepared by FIB in combination, with transmission electron microscopy. The principle of electron beam diffraction is similar to that of X-ray diffraction (XRD), which is the standard method for crystal structure analysis.

3.2.4.1 Information obtained by electron beam diffraction

In this study, we used electron beam diffraction to analyze the crystal structure of the surface oxide layer of porous alloy substrate. Figure 3-11 shows the crystal structure of γ-Al_2O_3 and the diffraction pattern which we can obtain from the crystal structure.

We can measure the *d-spacing* for each plane (hkl) in the diffraction pattern as the following equation in the case of cubic structure,

$$d - spacing = \frac{a}{\sqrt{(h^2 + k^2 + l^2)}}$$

where a is the lattice parameter (a = 7.9 $\AA$ in the case of γ-Al_2O_3.) We also can theoretically simulate the *d-spacing* for each plane (hkl) if we assume a specific crystal structure using database and software. In our study we used CS manager and

CrystalMaker®. If the deviation of all "*d-spacing* for each plane (hkl)" is smaller than 10%, we can consider that the crystal structure is well identified.

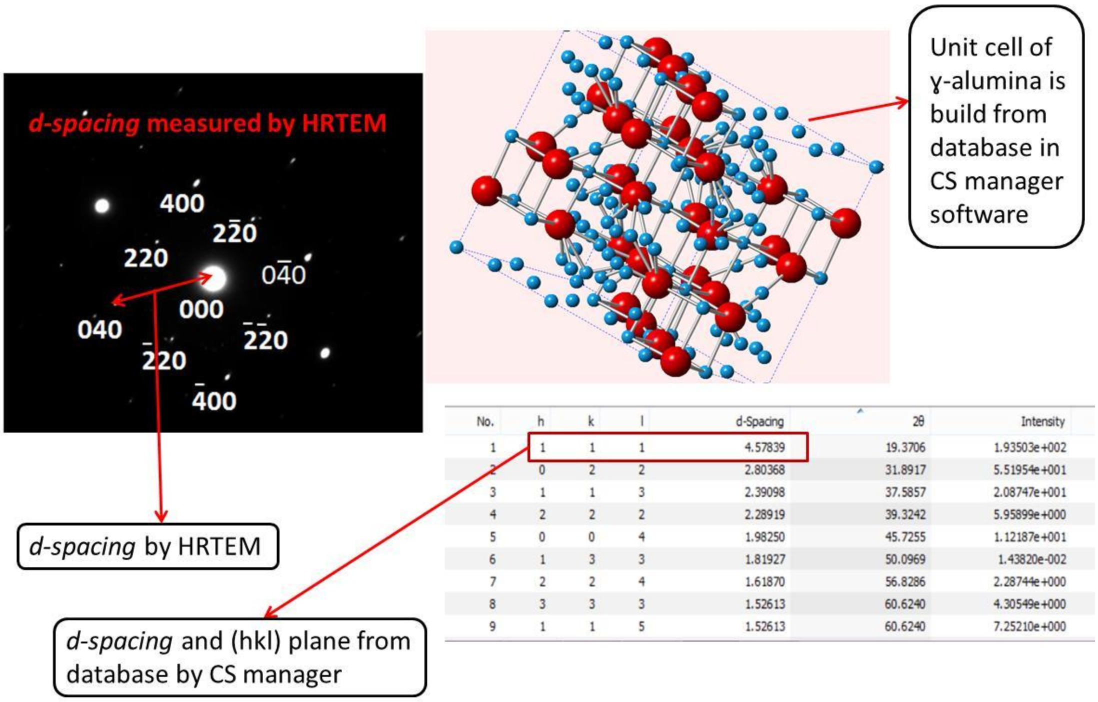

No.	h	k	l	d-Spacing	2θ	Intensity
1	1	1	1	4.57839	19.3706	1.93503e+002
2	0	2	2	2.80368	31.8917	5.51954e+001
3	1	1	3	2.39098	37.5857	2.08747e+001
4	2	2	2	2.28919	39.3242	5.95899e+000
5	0	0	4	1.98250	45.7255	1.12187e+001
6	1	3	3	1.81927	50.0969	1.43820e-002
7	2	2	4	1.61870	56.8286	2.28744e+000
8	3	3	3	1.52613	60.6240	4.30549e+000
9	1	1	5	1.52613	60.6240	7.25210e+000

Figure 3-11. Crystal structure and diffraction pattern of γ-Al_2O_3.

3.2.4.2 Fast fourier transformation (FFT) analysis

When we observe high resolution TEM (HRTEM) images, we can obtain a similar information as electron beam diffraction by using fast fourier transformation (FFT). FFT is the software transformation which is applied to the HRTEM image data. FFT image indicates the reciprocal space of the crystal. The advantage of FFT method is that we can analyze a very small area using HRTEM images.

Chapter 4

Decrease in Electrical Resistance of Surface Oxide of Porous Al-Cr-Fe Alloy by $La_{0.6}Sr_{0.4}Co_{0.2}Fe_{0.8}O_3$ Coating and Heat-Treatment for the Application of Metal-Supported SOFCs

Abstract [1]

We have investigated the property of a Fe-Cr-Al-type stainless steel as a porous alloy substrate for metal-supported solid oxide fuel cells (MSCs) especially on the cathode side. We found that the microstructure and electrical resistance of the surface oxide layer of the alloy changes depending on the heat-treatment conditions. A relatively low electrical resistance was obtained when the porous alloy substrate was coated with $La_{0.6}Sr_{0.4}Co_{0.2}Fe_{0.8}O_3$ (LSCF) and heat-treated at 700–800 °C in air. The morphology of the surface oxide layer observed by high-resolution transmission electron microscopy was columnar structure of γ-Al_2O_3 polycrystal and $Sr_3Al_2O_6$ growing outward in the same direction. In contrast, the surface oxide layer of the alloy showed a high electrical resistance when the uncoated porous alloy substrate was heat-treated. The morphology of the surface oxide layer in that case was a columnar structure consisting of only γ-Al_2O_3 growing outward in various directions.

---

[1] Published in Hung-Cuong Pham, Shunsuke Taniguchi, Yuko Inoue, Jyh-Tyng Chou, Toru Izumi, Koji Matsuoka, and Kazunari Sasaki, *J. Power Sources*, 297 (2015) 181-187.

4.1 Introduction

There are few reports of application of metal support to the cathode side. This is because vaporization of chromium species such as CrO_3(g) or $CrO_2(OH)_2$(g) from the alloy surface can cause degradation of the cathode [1-7], and the electrical resistance may increase after long-term operation owing to the growth of less-conductive Cr_2O_3 on the surface of the alloy.

Fe-Cr-Al alloy has been widely used for high-temperature applications such as heating furnaces and fire grids [8]. The excellent oxidation resistance of Fe-Cr-Al alloy originates from alumina layers formed on the surface at high temperatures [9]. However, Fe-Cr-Al alloy has not been considered as a candidate material for metal-supported SOFCs (MSCs) because of the high electrical resistance of the alumina layers [10]. It was reported that the microstructure of the alumina layers on the surface of Fe-Cr-Al alloy differs depending on the temperature, specifically long alumina whiskers appear at 900 °C [11] while equiaxed grains on the outer surface of and a columnar structure inside the alumina layer appear at 1000–1300 °C [12–14].

We have fabricated a porous Fe-Cr-Al alloy substrate and investigated its property as a support material on the cathode side of MSCs. We found that the electrical resistance between the porous alloy substrate and the $La_{0.6}Sr_{0.4}Co_{0.2}Fe_{0.8}O_3$ (LSCF) coating layer was relatively low and stable at 700 °C in air [15].

In Chapter 4, the objective is to clarify the elemental composition, crystal structure, and microstructure of the surface oxide layer of the Fe-Cr-Al alloy, which contributes to the electrical conduction by allowing the alloy to maintain a high oxidation resistance. Porous Fe-Cr-Al alloy substrates were heat-treated under different conditions with or without the LSCF coating, the interfacial resistance was measured, and the oxide layers were analyzed using high-resolution microscopy.

4.2 Experimental

Commercially available LSCF powder (>99.9%, Praxair, CT, US), terpineol, and ethylcellulose were mixed to make a LSCF coating material. We prepared several samples under different conditions as shown in Table 4-1 to clarify the effect of the LSCF coating on the oxidation process of the alloy.

Table 4-1. Experimental conditions for the investigation of the LSCF coating and heat-treatment effects.

	Condition 1	Condition 2	Condition 3	Condition 4
Heat-treatment	800 °C, 60 h in air	800 °C, 60 h in air	------	------
Coating	------	LSCF	LSCF	LSCF
Electrical resistance measurement	------	700 °C, 90 h in air	700 °C, 230 h in air	800 °C, 230 h in air
			Temperature dependence	Temperature dependence
Analysis	SEM, STEM-EDS	STEM-EDS, TEM-selected area electron diffraction	------	STEM-EDS, TEM-selected area electron diffraction

Two samples were firstly heat-treated at 800 °C in air for 60 h. One of these was then coated with LSCF, and the electrical resistance was measured at 700 °C in air for 90 h. Two other samples were firstly coated with LSCF and then heat-treated at 700 °C or 800 °C in air for 230 h while the electrical resistance was simultaneously measured.

The interfacial resistance was measured using the LSCF as the electrode with a platinum mesh and wire for the current collector as shown in Figure 3-3. The resistance obtained in this configuration reflects the electrical resistance of the surface oxide layer, which dominates the resistance in the circuit. The interfacial resistance was calculated by using an apparent electrode area. A cylindrical shape was selected to avoid detachment of the current collector during the measurement.

4.3 Results and discussion

4.3.1 Oxidation state of the alloy after heat treatment

The porous alloy substrate has a porosity of 45%, which seems to be sufficient for gas permeation as required for components of SOFC electrodes. A cross-sectional SEM image and STEM-EDS mappings of the substrate after the heat-treatment at 800 °C for 60 h (Condition 1) are shown in Figure 4-1and 4-2.

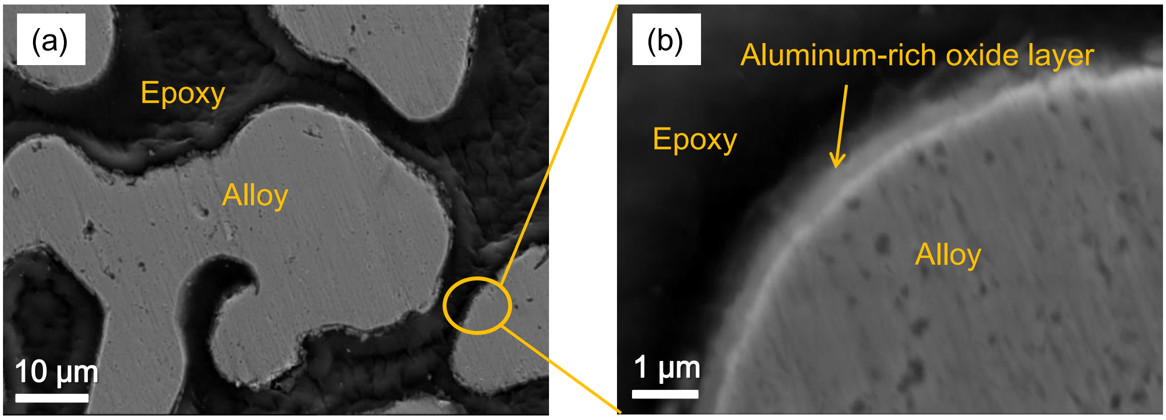

Figure 4-1. Cross-sectional SEM image of the porous alloy substrate after the heat-treatment at 800 °C for 60 h in air (Condition 1).

An aluminum-rich oxide layer with a thickness of 200–400 nm was observed over the whole surface of the alloy.

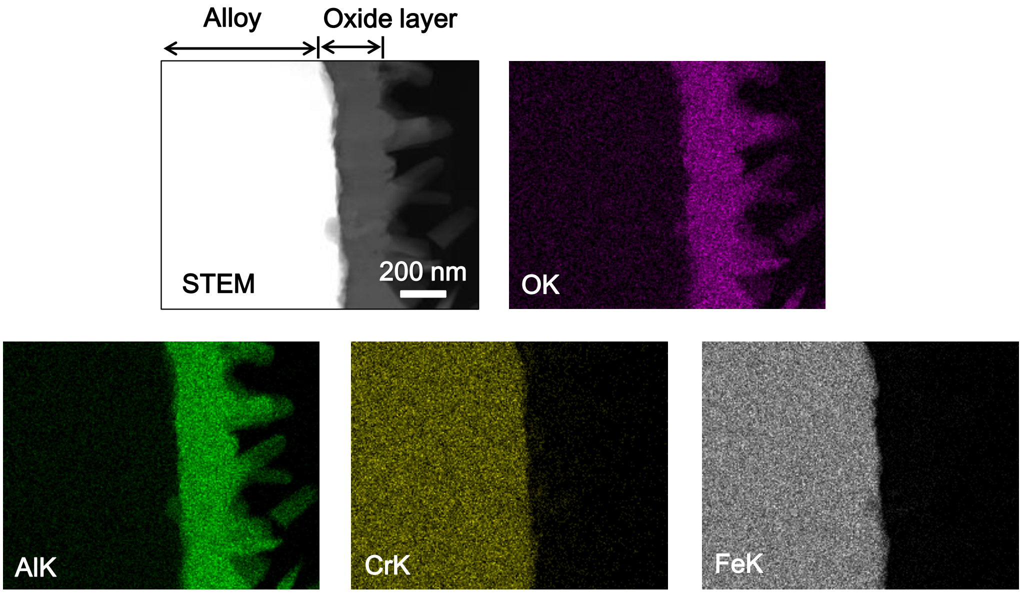

Figure 4-2. STEM image and EDS mappings (raw count maps of O, Al, Cr, and Fe) of the surface oxide layer of the porous alloy substrate after the heat-treatment at 800 °C for 60 h in air (Condition 1).

4.3.2 Decrease in electrical resistance of the surface oxide layer of the alloy by the LSCF coating

Figure 4-3(a) and 4-3(b) show the difference in the interfacial resistance caused by different heat-treatment conditions. Figure 4-3(a) shows the interfacial resistance of the porous alloy substrate heat-treated at 800 °C for 60 h and then coated with LSCF (Condition 2). The initial resistance was about 50 mΩcm^2, and after 90 h, the resistance increased to 470 mΩcm^2. This high electrical resistance comes from the oxide layer that covers the surface of the alloy. It seemed that some defects in the oxide layer, which may be generated by a reduction in temperature, caused the relatively low initial electrical resistance because LSCF grains may come into direct contact with the alloy. The increase in the electrical resistance with time may correspond to the oxide growth filling these defects.

In contrast, the interfacial resistance was stable at a relatively low value of around 20 mΩcm^2 in the case of samples prepared and measured under Conditions 3 and 4. The difference in the time dependence of Condition 3 and 4 seemed to be caused by the resistance of the LSCF coating. Because the heat-treatment temperature of 700 °C is not enough for sintering of the LSCF grains, the electrical resistance of Condition 3 may include the resistance of the LSCF coating. The electrical resistance of Condition 4 must have decreased over time because of sintering of the LSCF grains at 800 °C. Because the contact area between the porous alloy substrate and the LSCF coating was larger than in the case of a flat sample, it was estimated to be roughly 10 times larger than the apparent electrode area considering the pore size of the substrate and the penetration depth of the LSCF coating. The interfacial resistance shown in Figure 4-4 includes the effect of the increased contact area. Figure 4-3(c) shows the temperature dependence of the interfacial resistance of samples in Conditions 3 and 4 measured by decreasing the temperature after completing the measurement of the data in Figure 4-3 (b). Semi-conducting behavior was confirmed by the temperature dependence; therefore, the interfacial resistance was dominated by electron conduction through the surface oxide layer and not through direct contact with the LSCF coating with the metallic state of the alloy.

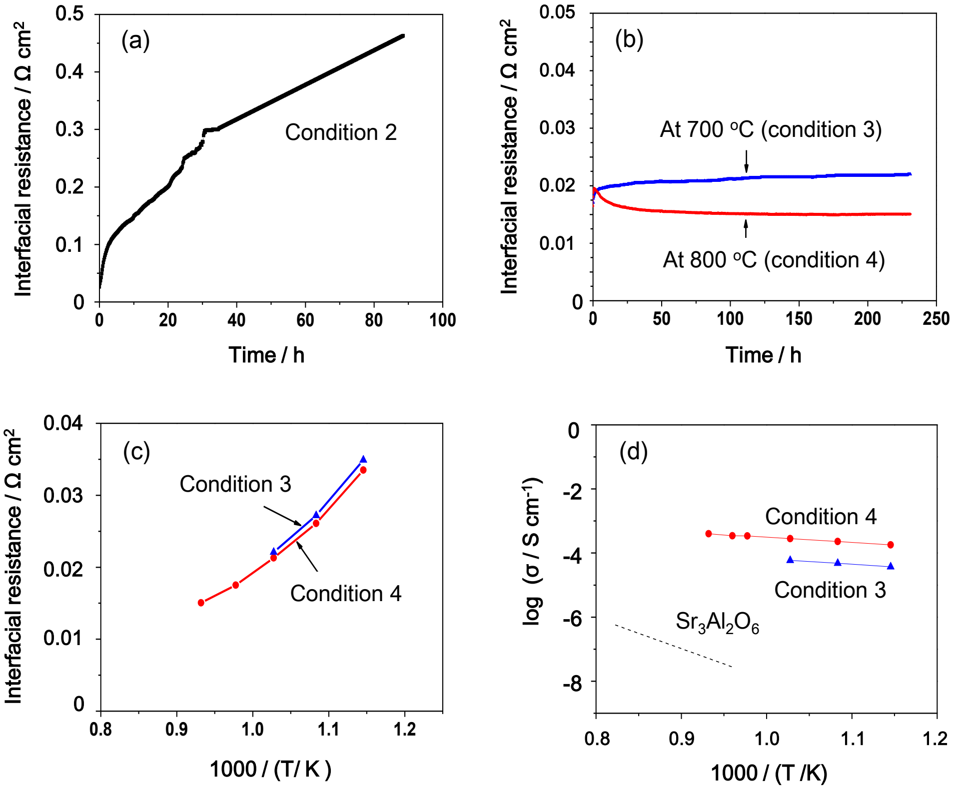

Figure 4-3. Interfacial resistance between the porous alloy substrate and the LSCF coating for samples (a) heat-treated at 800 °C for 60 h in air, coated with LSCF, and then measured at 700 °C for 90 h (condition 2), and (b) coated with LSCF, heat-treated at 700 °C or 800 °C for 230 h in air, and simultaneously measured (Conditions 3 and 4). (c) Temperature dependence of the interfacial resistance and (d) electrical conductivity after the measurements shown in (b). The literature data for $Sr_3Al_2O_6$ [17] is also shown for comparison.

Figure 4-3(d) shows electrical conductivity of the surface oxide layer under Conditions 3 and 4,which was estimated using the data in Figure 4-3(c), assuming that the contact area was 10 times larger than the apparent electrode area and the thicknesses of the oxide layers were 130 nm and 600 nm under Conditions 3 and 4, respectively.

4.3.3 Change in crystal structure of the surface oxide layer by the LSCF coating

Figure 4-4 shows an STEM image and EDS mappings of the surface oxide layer of the porous alloy substrate after the experiment conducted under Condition 2. The O, Al, and Sr concentrations in the oxide layer were 63.4, 34.9, and 0.7 at.%, respectively. The Cr concentration in the oxide layer obtained by the EDS analysis was 0.3 at.%, which is considered to be below the background level. Figure 4-5 shows a TEM image of this surface oxide layer; columnar oxide crystals growing in different directions are represented by arrows. The crystal structure in the circled area in Figure 4-5(a) was identified as γ-Al_2O_3 by the electron diffraction pattern shown in Figure 4-5(b).

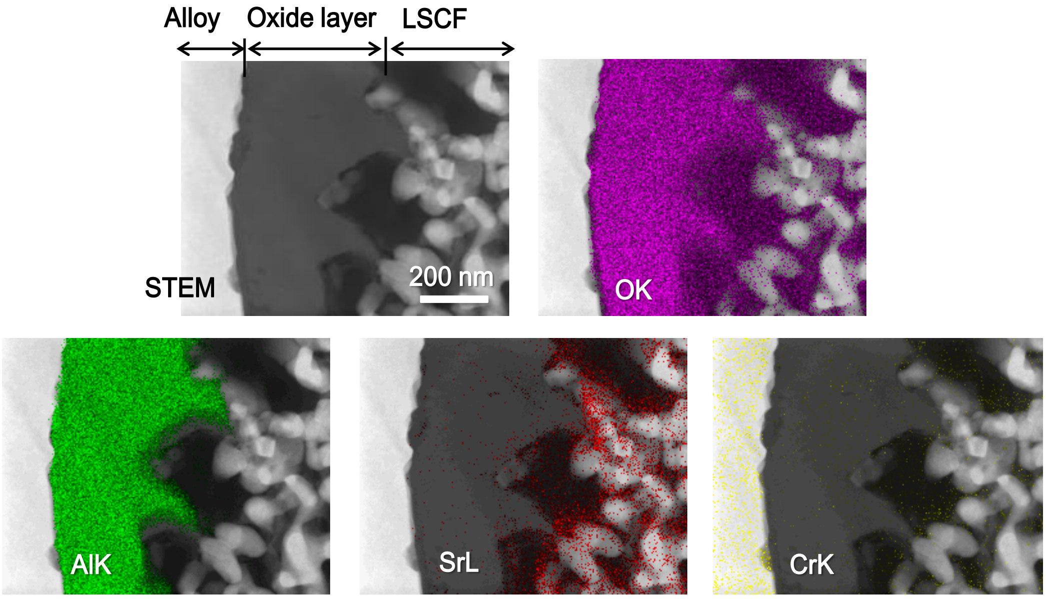

Figure 4-4. STEM image and EDS mappings (raw count maps of O, Al, Sr, and Cr) of the surface oxide layer of the porous alloy substrate after the experiment conducted under Condition 2.

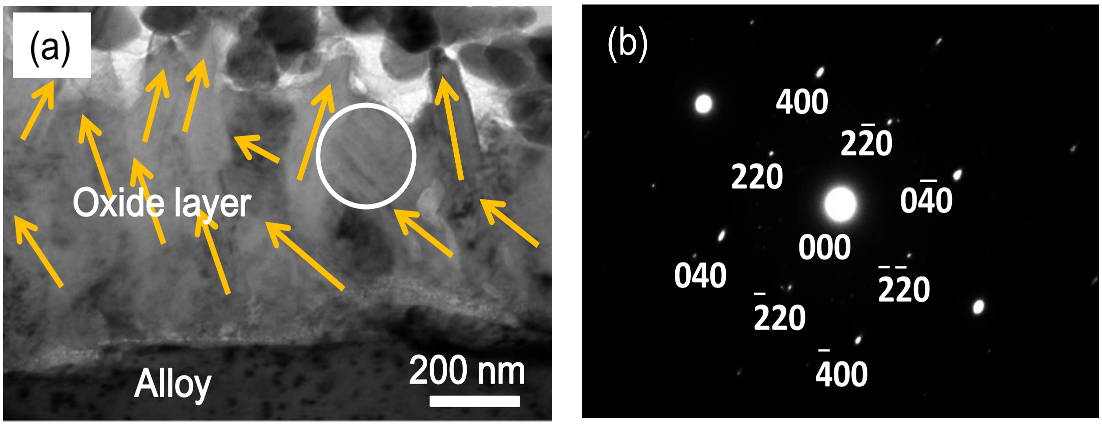

Figure 4-5. (a) TEM image of the surface oxide layer of the porous alloy substrate after the experiment conducted under Condition 2. (b) Electron diffraction pattern obtained from the selected-area shown in (a).

Figure 4-6 shows a STEM image and EDS mappings at the interface of the porous alloy substrate and the LSCF coating before heat-treatment. We clearly distinguish the alloy and LSCF, and there was no surface oxide layer formed on the alloy.

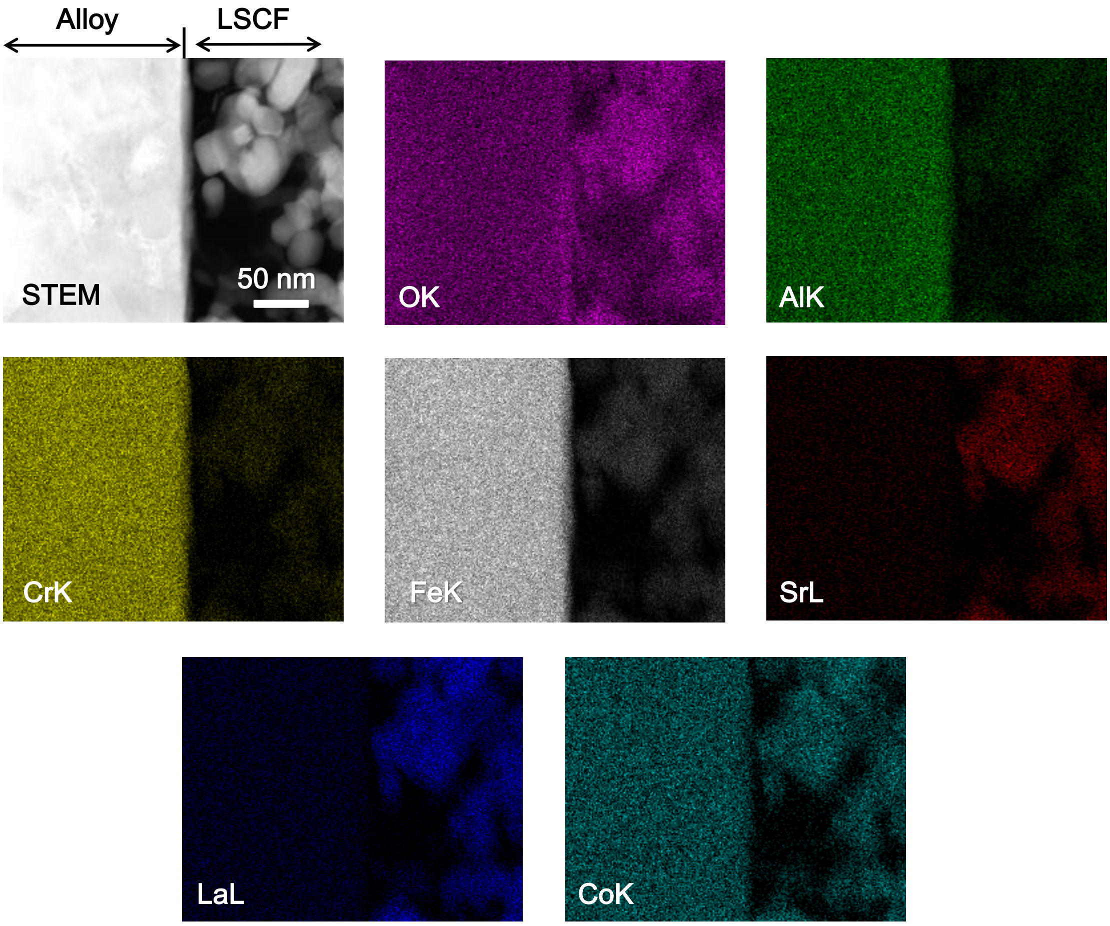

Figure 4-6. STEM image and EDS mappings (raw count maps of O, Al, Fe, Cr, Sr, La, and Co) at the interface of the porous alloy substrate and LSCF coating before any heat-treatment.

Figure 4-7 shows a STEM image and EDS mappings of the surface oxide layer of the porous alloy substrate after the experiment conducted under Condition 4. The O, Al, and Sr concentrations in the oxide layer were 58.6, 36.4, and 3.8 at.%, respectively. The Cr concentration in the oxide layer obtained by the EDS analysis was 0.3 at.% (below the background level), which means that the surface oxide layer prevented Cr diffusion outward from the alloy. It is, therefore, suggested that the porous alloy substrate may suppress vaporization of chromium species in comparison with the case of Fe-Cr alloy.

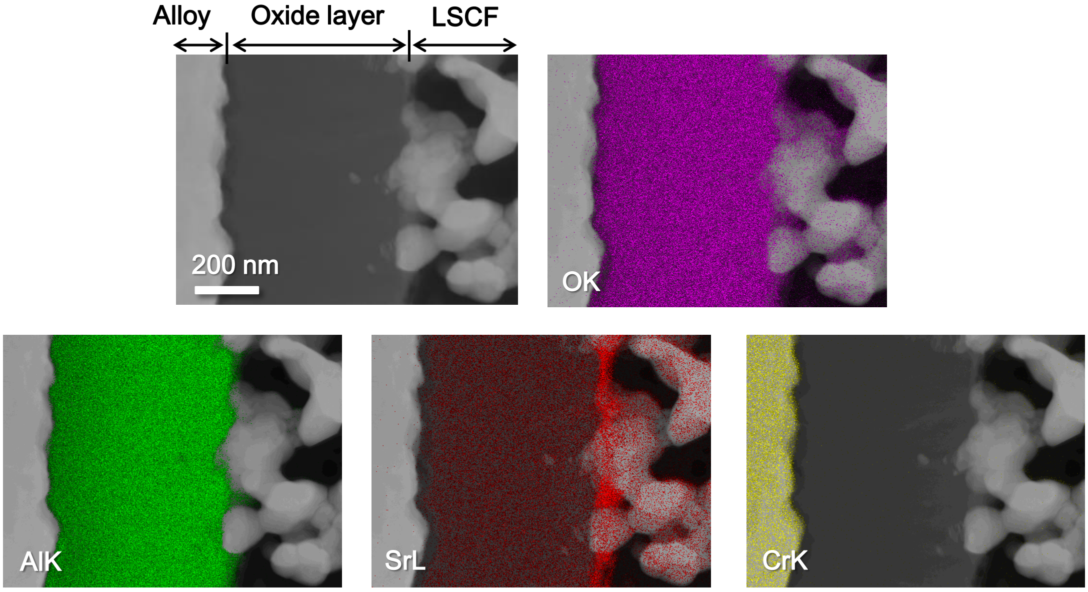

Figure 4-7. STEM image and EDS mappings (raw count maps of O, Al, Sr, and Cr) of the surface oxide layer of the porous alloy substrate after the experiment conducted under Condition 4.

The microstructure of the surface oxide layer after the experiment conducted under Condition 4 was observed using TEM as shown in Figure 4-8. A columnar oxide grew outward in the direction indicated by the arrows in the figure. The electron diffraction pattern obtained from area 1 in Figure 4-8(a) is shown in Figure 4-8(b) and indicates a polycrystal of γ-Al_2O_3; the rings were attributed to γ-Al_2O_3 (311), (400), and (440). The electron diffraction pattern obtained from area 2 in Figure 4-8(a) is shown in Figure 4-8(c), and the rings were attributed to cubic $Sr_3Al_2O_6$ (511), (250), and (761) [16]. These electron diffraction patterns suggest a complex structure consisting of γ-Al_2O_3 polycrystal and $Sr_3Al_2O_6$ crystal. As shown in Figure 4-3(d), the electrical conductivity of the surface oxide layer was roughly 10^3-10^4 higher than that of $Sr_3Al_2O_6$ at 800 °C [17]. The activation energies of the electrical conduction for Conditions 3 and 4 were 32 kJ/mol and 31 kJ/mol, respectively, in contrast to that of 188 kJ/mol for $Sr_3Al_2O_6$.

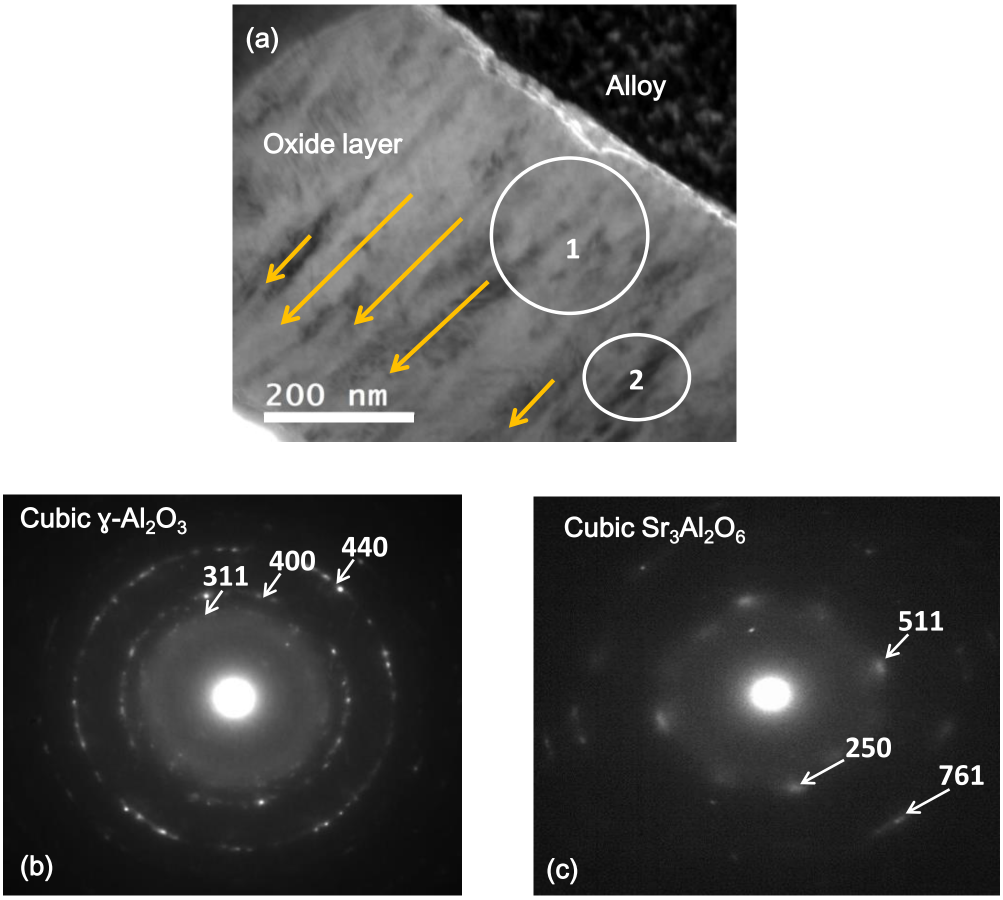

Figure 4-8. (a) TEM image of the surface oxide layer of the porous alloy substrate after the experiment conducted under Condition 4 and electron diffraction patterns obtained (b) from area 1 and (c) from area 2.

4.3.4 Mechanism of the growth of the surface oxide layer

Considering the above results, the differences in the surface oxide layers generated under these experimental conditions are summarized in Figure 4-9. In the case of Condition 2, Al ions diffuse outward during the heat-treatment to react with oxygen and result in a columnar structure consisting of γ-Al_2O_3 with different orientations as shown in Figure 4-9(a). The columnar structure of γ-Al_2O_3 was also observed by Liu et al. [18] on a FeCrAlRE alloy at 900 °C. This columnar structure is stable and does not allow any other cations to diffuse, and so the LSCF coating and further heat-treatment do not change the elemental composition and crystal structure. As a result, the interfacial resistance remains high because of the electrical property of γ-Al_2O_3 and the random direction of the columnar structure.

In the case of Condition 4, some of the Al ions diffusing outward during oxidation of the alloy react with Sr segregated from LSCF to form $Sr_3Al_2O_6$. Although the Sr content in the surface oxide layer is less than 4 at.%, the formation of $Sr_3Al_2O_6$ along with γ-Al_2O_3 results in a complex structure consisting of γ-Al_2O_3 polycrystal and $Sr_3Al_2O_6$ crystal growing outward in the same direction as a columnar structure as shown in Figure 4-9(b). The electronic conductivity of the oxide layer was 10^3-10^4 times higher than that of $Sr_3Al_2O_6$ as shown in Figure 4-9. We hypothesize that the electronic conduction path was generated at a thin interface of γ-Al_2O_3/$Sr_3Al_2O_6$ by a similar mechanism to that at the hetero-interface of $LaAlO_3$/$SrTiO_3$ [19-20] or γ-Al_2O_3/$SrTiO_3$ [21], in which the polarity discontinuities lead to electronic reconstruction and significantly enhance the mobility of the charge carriers.

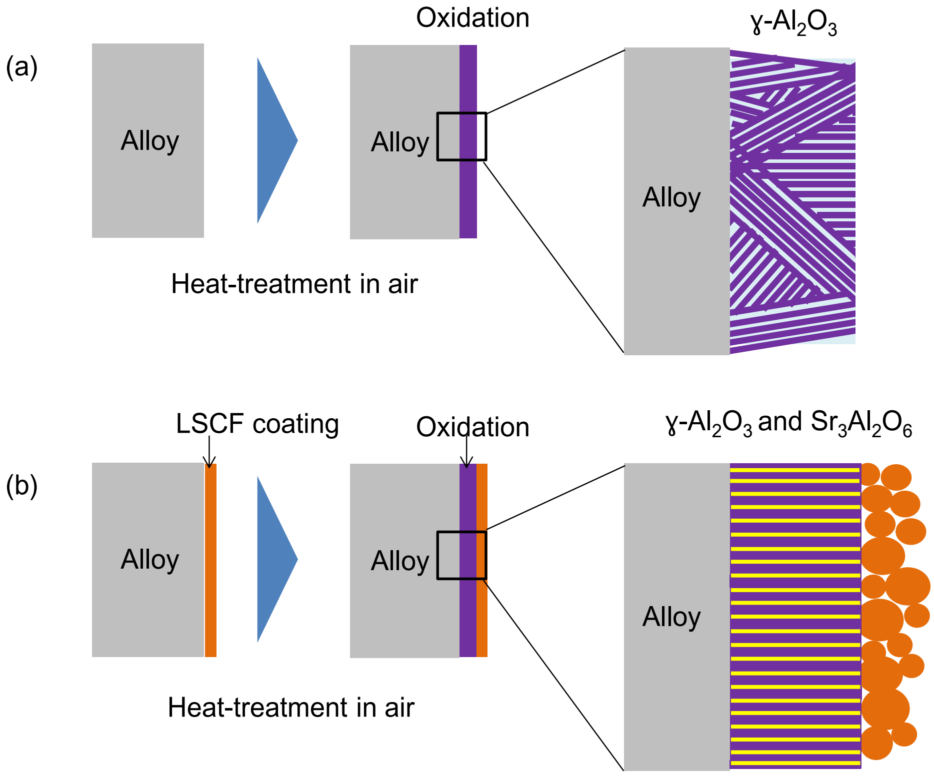

Figure 4-9. Schematic diagram of the difference in the microstructure of the oxide layer formed on the surface of the Fe-Cr-Al alloy.

The columnar structure arranged perpendicular to the surface may also contribute to the enhancement of the electronic conductivity by connecting the conduction path from inside the alloy to the outside.

4.4 Conclusions

The microstructure and electrical resistance of the surface oxide layer of porous Fe-Cr-Al alloy changes depending on the heat-treatment conditions. A relatively low electrical resistance was obtained when the LSCF-coated porous alloy substrate was heat-treated at 700–800 °C in air. The surface oxide layer was a complex structure consisting of γ-Al_2O_3 polycrystal and $Sr_3Al_2O_6$ crystal growing outward in the same direction as a columnar structure. We hypothesize that the electronic conduction path was generated at a thin interface of γ-$Al_2O_3/Sr_3Al_2O_6$ by a similar mechanism to that occurred at the hetero-interface of $LaAlO_3/SrTiO_3$ or γ-$Al_2O_3/SrTiO_3$, in which the polarity discontinuities lead to electronic reconstruction and significantly enhance the mobility of the charge carriers. In addition, the columnar structure arranged perpendicular to the surface may also contribute to the enhancement of the electronic conductivity by connecting the conduction path from inside of the alloy to the outside. In contrast, the surface oxide layer of the alloy showed a high electrical resistance when the uncoated porous alloy substrate was heat-treated. The surface oxide layer consisted of columnar γ-Al_2O_3 growing in various directions and showed a high electrical resistance due to the electrical properties of γ-Al_2O_3.

References

[1] S. Taniguchi, M. Kadowaki, H. Kawamura, T. Akiyama, Y. Miyake, T. Saitoh, J. Power Sources 55 (1995) 73.

[2] K. Hilpert, D. Das, M.Miller, D. H. Peck, R. Weiss, J. Electrochemical Society 143 (11) (1996) 3642.

[3] S. P. S. Badwal, R. Deller, K. Fogera, Y. Ramprakash, J.P. Zhang, Solid State Ionics 99 (1997) 297.

[4] S. P. Jiang, J. P. Zhang, L. Apateanu, K. Foger, J. Electrochemical Society 147 (11) (2000) 4013.

[5] Y. Matsuzaki, I. Yasuda, J. Electrochemical Society 148 (2) (2001) A126.

[6] J. W. Fergus, Int. J. Hydrogen Energ. 32 (2007) 3664.

[7] M. K. Stodolny, B. A. Boukamp, D. H. A. Blank, F. P. F. van Berkel, J. Power Sources, 209 (2012) 120.

[8] H. Echsler, H. Hattendorf, L. Singheiser, W. J. Quadakkers, Mater. Corros. 57 (2006) 115.

[9] T. Ohashi, N. Tsuno, T. Kurokawa, European Patent EP 0617139 B2 (2003).

[10] H. Venugopalan, K. Tankala, T. DebRoy, J. Am. Ceram. Soc. 77 (1994) 3045.

[11] C. Badini, F. Laurella, Surf. Coat. Technol. 135 (2001) 291.

[12] J. Öijerholm, J. Pan, Q. Lu, C. Leygraf, Oxid. Met. 68 (2007) 253.

[13] J. K. Tien, F. S. Pettit, Metall. Trans. 3 (1972) 1578.

[14] J. A. Nychka, D. R. Clarke, Oxid. Met. 63 (2005) 325.

[15] H. C. Pham, E.-J. Park, S. Taniguchi, K. Sasaki, ECS Trans. 57 (2013) 2289.

[16] Y.-L. Chang, H.-I Hsiang, M.-T. Liang, J. Am. Ceram. Soc. 90 (2007) 2759.

[17] K. V. Zakharchuk, A. A. Yaremchenko, D. P. Fagg, J. Alloys Compd. 613 (2014) 232.

[18] F. Liu, H. Götlind, J.-E. Svensson, L.-G. Johansson, M. Halvarsson, Oxid. Met. 74 (2010) 11.

[19] A. Ohtomo, H. Y. Hwang, Nature 427 (2004) 423.

[20] N. Reyren, S. Thiel, A. D. Caviglia, L. F. Kourkoutis, G. Hammerl, C. Richter, C. W. Schneider, T. Kopp, A.-S. Rüetschi, D. Jaccard, M. Gabay, D. A. Muller, J.-M. Triscone, J. Mannhart, Science 317 (2007) 1196.

[21] Y. Z. Chen, N. Bovet, F. Trier, D. V. Christensen, F. M. Qu, N. H. Andersen, T. Kasama, W. Zhang, R. Giraud, J. Dufouleur, T. S. Jespersen, J. R. Sun, A. Smith, J. Nygård, L. Lu, B. Büchner, B. G. Shen, S. Linderoth, N. Pryds, Nat. Commun. 4 (2013) 1371.

Chapter 5

Modification of the Microstructure of the Surface Oxide Layer of Fe-Cr-Al Alloy by Coating Materials

Abstract[1]

We investigated effect of coating materials using $La_{0.8}Sr_{0.2}MnO_3$ (LSM), $LaNi_{0.6}Fe_{0.4}O_3$ (LNF), and $Pr_{0.8}Sr_{0.2}MnO_3$ (PrSM). Relatively low contact resistances were obtained in all cases when these materials were coated on the alloy first, and then heat-treated at 700 °C in air, which are the similar results with the case of LSCF. The surface oxide layer of the alloy was analyzed by STEM-EDS in detail to clarify the cause of low electrical resistance. In the surface oxide layer, small amount of La, Ni, Pr or Sr were observed. It is expected that the same microstructure, as discussed in Chapter 4, consisting of γ-Al_2O_3 columnar crystal grows outward in the same direction, and small amount of aluminum compound with La, Ni, Pr or Sr was formed for each material. In the case of LNF, the interfacial resistance and activation energy of the electrical conduction were slightly lower than the other cases. Possibility of formation of $NiAl_2O_4$, with higher electronic conductivity than $Sr_3Al_2O_6$, between the γ-Al_2O_3 columnar crystals was suggested.

---

[1] Hung-Cuong Pham, Shunsuke Taniguchi, Yuko Inoue, Jyh-Tyng Chou, Toru Izumi, Koji Matsuoka, and Kazunari Sasaki, *J. Alloys Comp.* (To be submitted).

5.1 Introduction

The area specific resistance (ASR) of cell should be relatively low for long-term operation when porous alloy substrate is applied for MSC. In Chapter 4, we found that the microstructure and electrical resistance of the surface oxide layer of porous Fe-Cr-Al alloy changes depending on the heat-treatment conditions. We obtained relatively low electrical resistance with LSCF-coated Fe-Cr-Al alloy at 700–800 °C in air. The surface oxide layer changed to a complex structure consisting of γ-Al_2O_3 polycrystal and $Sr_3Al_2O_6$ crystal growing outward in the same direction as a columnar structure by the LSCF coating and heat treatment. The surface oxide layer does not contain chromium and may suppress chromium diffusion, which has been one of the critical issues for the conventional Fe-Cr alloy. Thus, we regard this material as a candidate material for MSC.

In this chapter, we used various electrode materials such as $La_{0.6}Sr_{0.4}Co_{0.2}Fe_{0.8}O_3$ (LSCF), $La_{0.8}Sr_{0.2}MnO_3$ (LSM), $LaNi_{0.6}Fe_{0.4}O_3$ (LNF), $Pr_{0.8}Sr_{0.2}MnO_3$ (PrSM) and investigated the change in the electrical resistance, microstructure and elemental composition of the surface oxide layer to clarify the optimum condition for the application of MSCs.

5.2 Experimental

We measured interfacial resistance between non-porous Fe-Cr-Al alloy and electrode materials such as LSCF, LSM, LNF or PrSM in the configuration shown in Figure 3-4. We used non-porous Fe-Cr-Al alloy to compare the interfacial resistances quantitatively. The samples were firstly coated with these electrode materials and then heat-treated at 700 °C in air for 230 h while the electrical resistances were simultaneously measured. We also conducted the same experiments using the porous alloy substrates as in Chapter 4, and analysed the surface oxide layer by STEM.

5.3 Results and Discussion

5.3.1 Interfacial resistances for different electrode materials

Figure 5-1 shows the interfacial resistances between the non-porous alloy substrates for different electrode materials. The interfacial resistances were relatively low and stable for 230 h not only for LSCF but also for the other electrode materials. We think that the low interfacial resistance was caused by the coating condition, in which the samples were firstly coated with these electrode materials and then heat-treated in air. The interfacial resistances in this chapter were approximately 10 times higher than the results in Chapter 4. The difference in the interfacial resistance came from the difference in contact area between the alloy and the electrodes.

Figure 5-2 shows the temperature dependence of the interfacial layers measured by decreasing the temperature after completing the measurement in Figure 5-1. Semi-conducting behavior was confirmed as discussed in Chapter 4. Therefore the interfacial resistance was dominated by electron conduction through the surface oxide layer. The activation energy of the electronic conduction through the surface oxide layer for LSCF, LSM, LNF and PrSM derived from Figure 5-2 were 30.3 kJ/mol, 30.13 kJ/mol, 18.8 kJ/mol, 27.2 kJ/mol, respectively. The interfacial resistance for LNF was slightly lower, and activation energy of the electronic conduction was also slightly lower than the other cases. Thus, possibility of formation of higher conductive material was suggested in the case of LNF. Activation energies for LSCF, LSM, and PrSM were almost the same, even though the interfacial resistance for PrSM was slightly higher than the other cases.

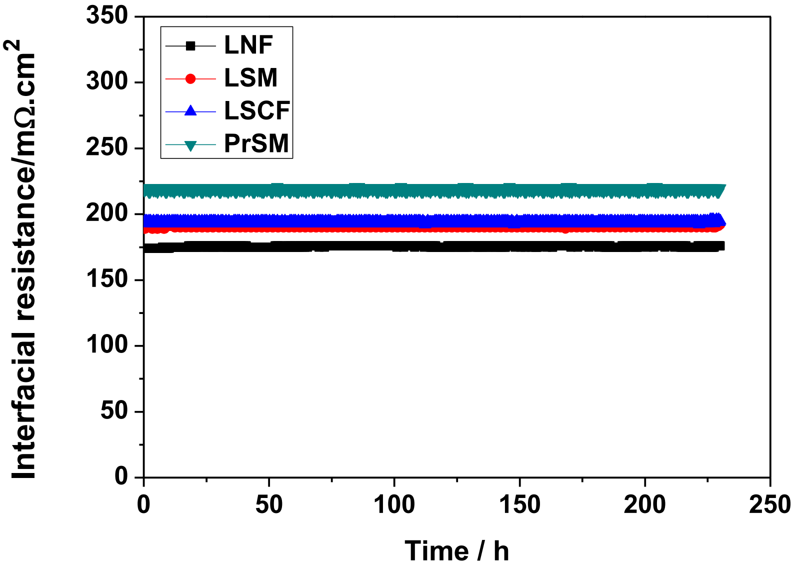

Figure 5-1. Interfacial resistances between the non-porous alloy substrate and electrode materials at 700 °C in air.

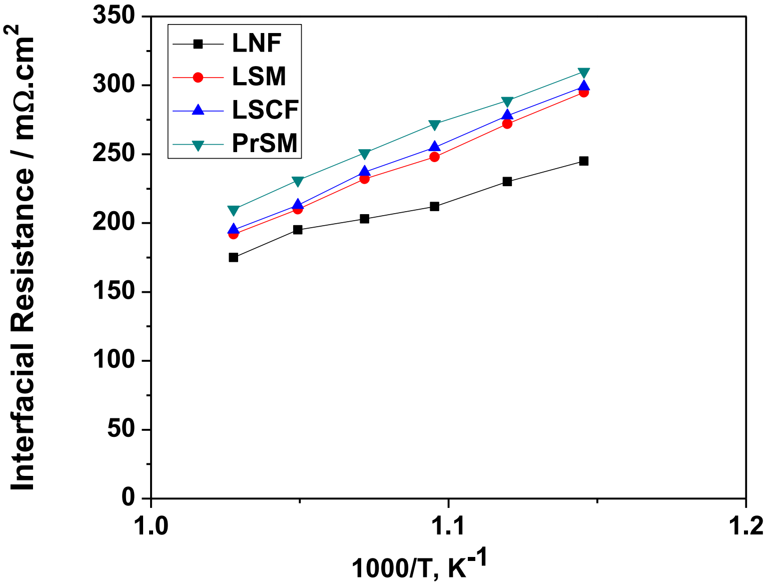

Figure 5-2. Temperature dependence of the interfacial resistance after the measurements shown in Figure 5-1.

5.3.2 Elemental composition of the surface oxide layer

Figure 5-3 shows an STEM image and EDS mappings of the surface oxide layer of the porous alloy substrate and LSCF coating after heat treatment at 700 °C for 230 h in air. An aluminum-rich oxide layer with a thickness of about 100 nm was observed over the whole surface of the alloy. The O, Al, and Sr concentrations in the oxide layer were 58.6, 35.6, and 3.97 at.%, respectively as shown in Figure 5-4.

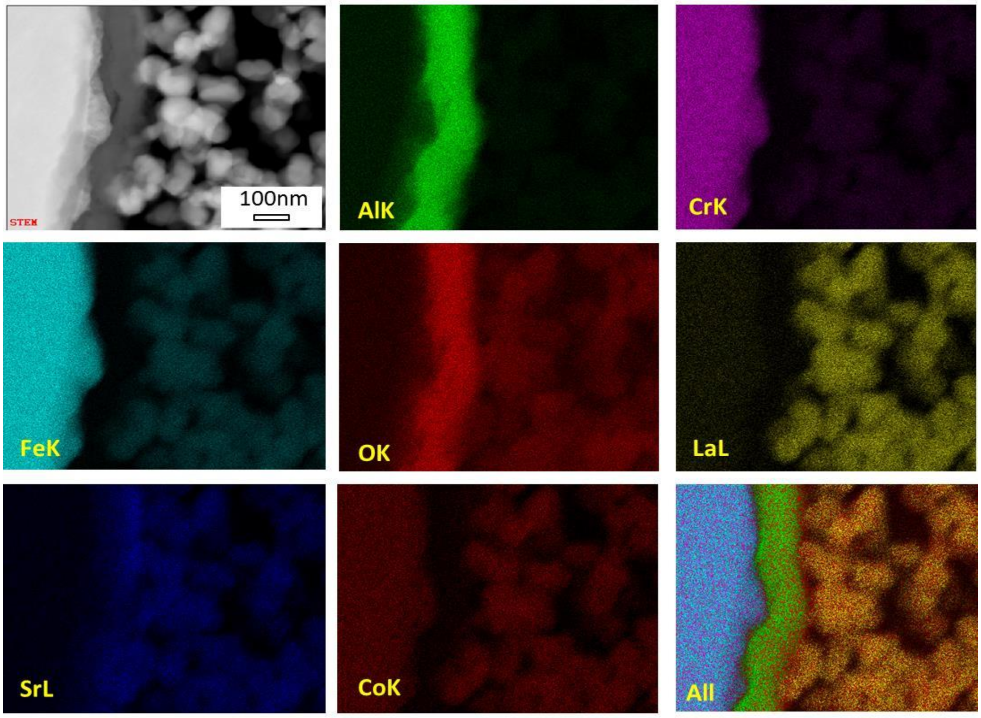

Figure 5-3. STEM image and EDS mappings (raw count maps of Al, Cr, Fe, O, La, Sr and Co) of the surface oxide layer of the porous alloy substrate coated with LSCF and heat-treated at 700 °C for 230 h in air.

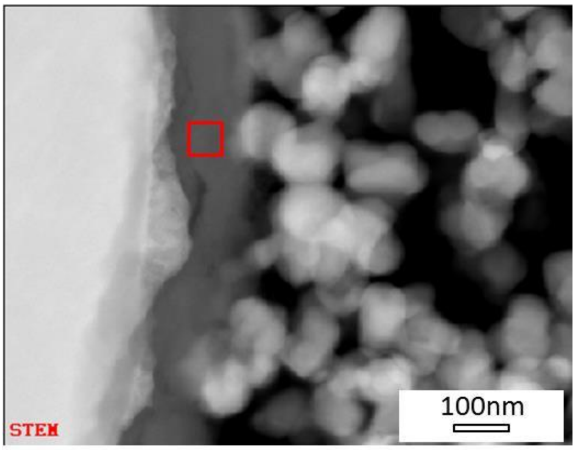

Element	Wt%	At%
AlK	40.51	35.59
CrK	0.84	0.38
FeK	1.85	0.78
OK	39.59	58.66
LaL	1.79	0.31
SrL	14.67	3.97
Cok	0.75	0.3

Figure 5-4. STEM image and elemental composition of the surface oxide layer of the porous alloy substrate coated with LSCF and heat-treated at 700 °C for 230 h in air.

Figure 5-5 shows an STEM image and EDS mappings of the surface oxide layer of the porous alloy substrate and LSM coating after heat treatment at 700 °C for 230 h in air. The O, Al, La, and Sr concentrations in the oxide layer were 56.71, 40.25, 0.91 and 0.48 at.%, respectively as shown in Figure 5-6.

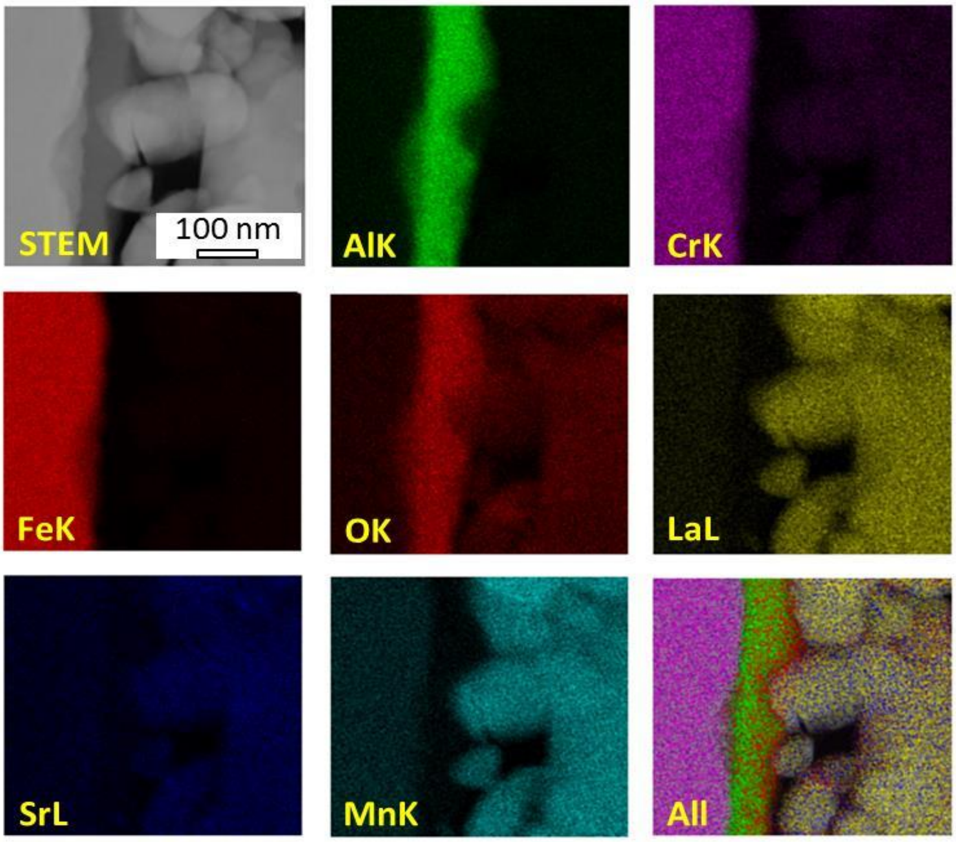

Figure 5-5. STEM image and EDS mappings (raw count maps of Al, Cr, Fe, O, La, Sr and Mn) of the surface oxide layer of the porous alloy substrate coated with LSM and heat-treated at 700 °C for 230 h in air.

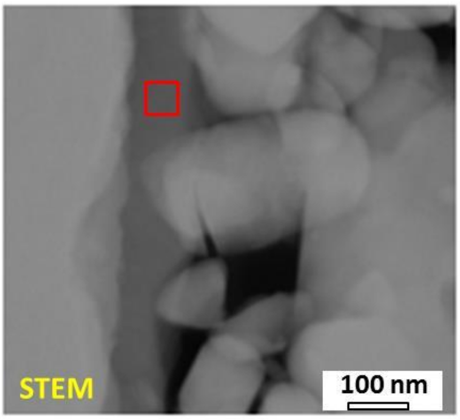

Elemental	Wt%	At%
AlK	48.71	40.25
CrK	0.98	0.42
FeK	1.71	0.68
OK	40.70	56.71
LaL	2.97	0.48
SrL	3.56	0.91
MnK	1.36	0.55

Figure 5-6. STEM image and elemental composition of the surface oxide layer of the porous alloy substrate coated with LSM and heat-treated at 700 °C for 230 h in air.

Figure 5-7 shows an STEM image and EDS mappings of the surface oxide layer of the porous alloy substrate and LNF coating after heat treatment at 700 °C for 230 h in air. The O, Al, La, and Ni concentrations in the oxide layer were 62.51, 32.54, 0.85 and 2.38 at.%, respectively as shown in Figure 5-8.

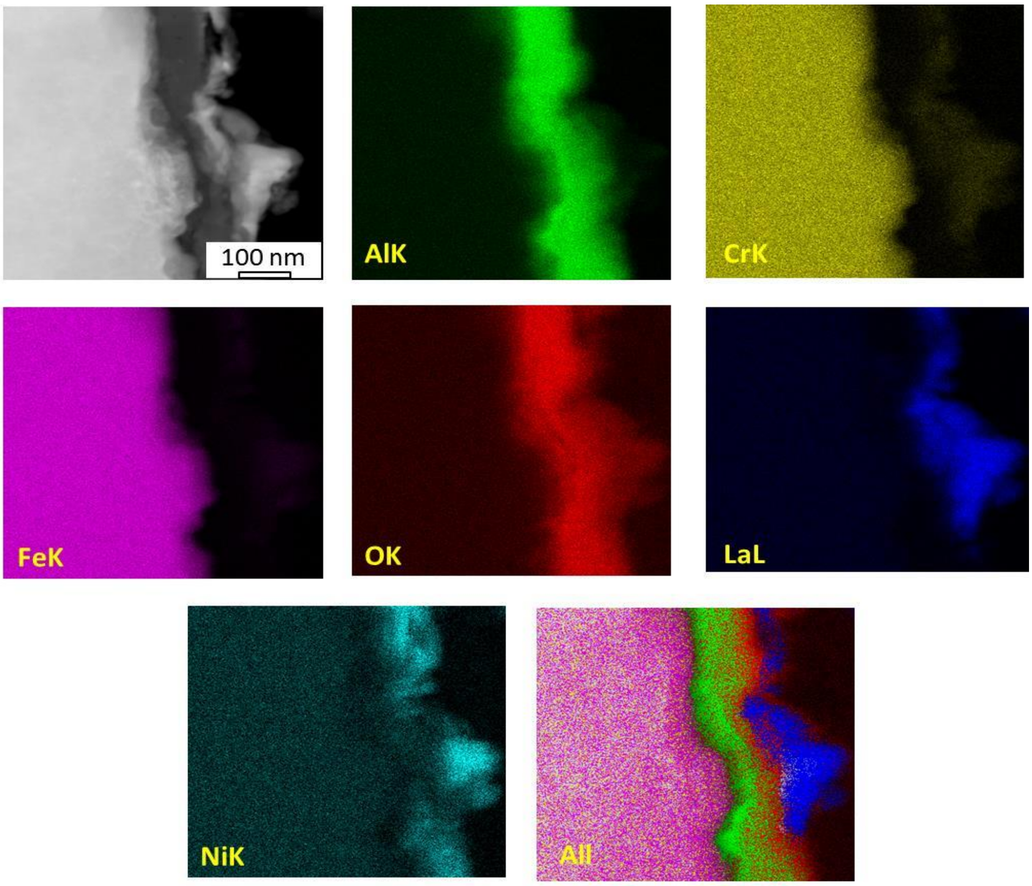

Figure 5-7. STEM image and EDS mappings (raw count maps of Al, Cr, Fe, O, La and Ni) of the surface oxide layer of the porous alloy substrate coated with LNF and heat-treated at 700 °C for 230 h in air.

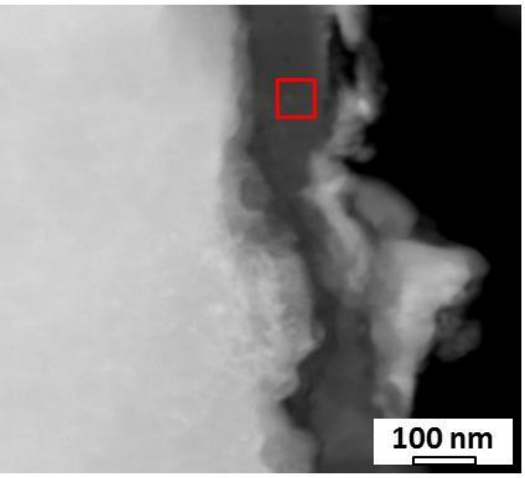

Element	Wt%	At%
AlK	39.38	32.54
CrK	1.34	0.58
FeK	2.87	1.15
OK	44.86	62.51
LaL	5.27	0.85
NiK	6.28	2.38

Figure 5-8. STEM image and elemental composition of the surface oxide layer of the porous alloy substrate coated with LNF and heat-treated at 700 °C for 230 h in air.

Figure 5-9 shows an STEM image and EDS mappings of the surface oxide layer of the porous alloy substrate and PrSM coating after heat treatment at 700 °C for 230 h in air. We clearly observed O, Al, La, and Ni mapping at the interface, and the O, Al, and Pr concentrations in the oxide layer were 63.54, 34.36, and 0.9 at.%, respectively as shown in Figure 5-10.

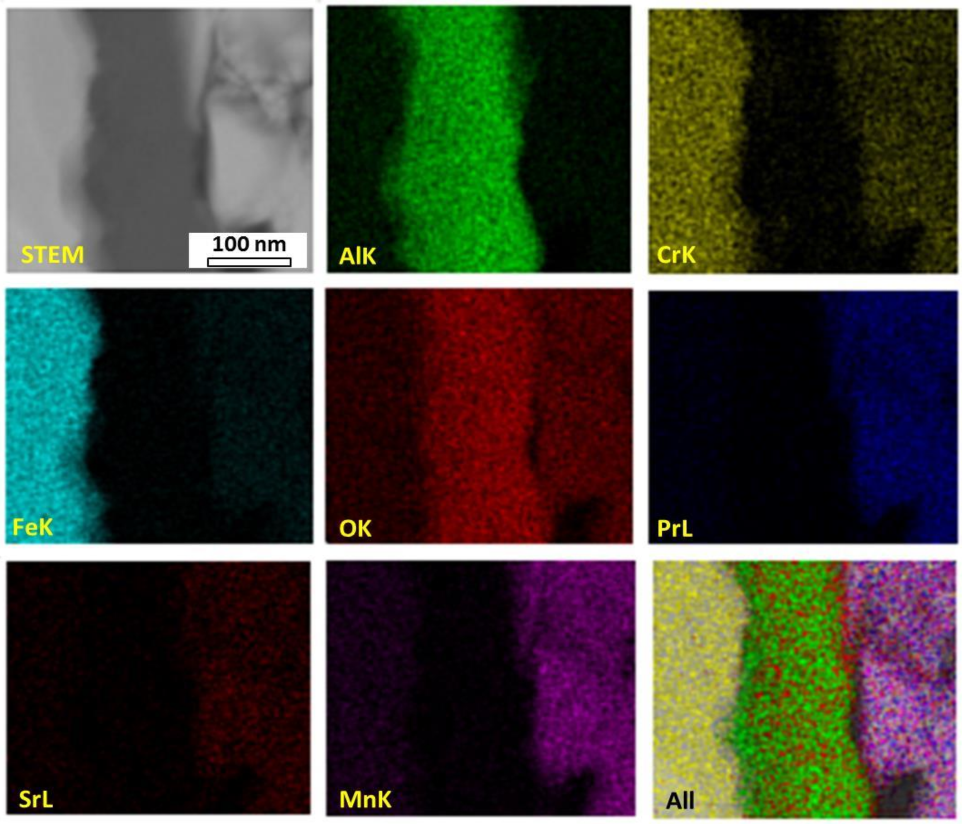

Figure 5-9. STEM image and EDS mappings (raw count maps of Al, Cr, Fe, O, Pr, Sr and Mn) of the surface oxide layer of the porous alloy substrate coated with PrSM and heat-treated at 700 °C for 230 h in air.

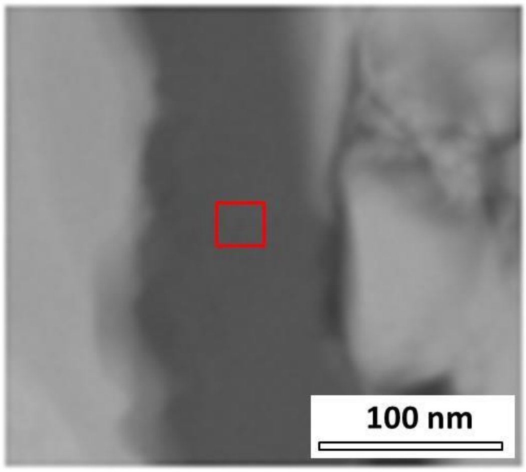

Element	Wt%	At%
AlK	44.85	34.36
CrK	0.48	0.19
FeK	1.33	0.49
OK	45.60	63.54
PrL	6.09	0.90
SrL	0.70	0.16
MnK	0.94	0.35

Figure 5-10. STEM image and elemental composition of the surface oxide layer of the porous alloy substrate coated with PrSM and heat-treated at 700 °C for 230 h in air.

5.3.3 Microstructure of the surface oxide layer of the alloy

As we confirmed in Chapter 4, in the case of LSCF-coating, the surface oxide layer was a complex structure consisting of γ-Al_2O_3 polycrystal and $Sr_3Al_2O_6$ crystal growing outward in the same direction as a columnar structure. We believe that the similar microstructure was obtained in the surface oxide layer for LSM-, LNF- and PrSM-coating, because the interfacial resistance was relatively low and stable for each case. Small amount of La, Ni, Pr was also observed in the surface oxide layer, which may contribute electronic conduction as Sr in the case of LSCF-coating. We assume that γ-Al_2O_3/$Sr_3Al_2O_6$ (in the case of LSM), γ-Al_2O_3/$NiAl_2O_4$ (in the case of LNF), and γ-Al_2O_3/$PrAlO_3$ (in the case of PrSM) formed between γ-Al_2O_3 columnar polycrystal growing outward in the same direction.

5.4 Conclusions

We obtained relatively low interfacial resistances when we used LSM, LNF or PrSM for the electrode materials, which are the similar results with the case of LSCF. In the surface oxide layer, small amount of La, Ni, Pr or Sr were observed. It is expected that the same microstructure, as discussed in Chapter 4, consisting of γ-Al_2O_3 columnar crystal growing outward in the same direction, and small amount of aluminum compound with La, Ni, Pr or Sr was formed for each material. In the case of LNF, the interfacial resistance and activation energy of the electrical conduction were slightly lower than the other cases. Possibility of formation of γ-Al_2O_3 /$NiAl_2O_4$, with higher electronic conductivity than γ-Al_2O_3 /$Sr_3Al_2O_6$, between γ-Al_2O_3 columnar crystals was suggested.

Chapter 6

Durability of the Fe-Cr-Al Alloy with the Modified Surface Oxide Layer

Abstract [1]

We investigated long-term durability of the oxidation resistance of the LSCF-coated Fe-Cr-Al alloy at 700 °C by measuring the mass gain, surface oxide thickness, and electrical resistance at different temperatures from 700 to 900 °C. Relatively low interfacial resistance were obtained at 700, 800, and 900 °C, and the mass gain followed the parabolic law of Wagner’s theory over the whole period investigated. By extrapolation of the data, we estimated that operation of 17,000 h at 700 °C is equal to that of 230 h at 900 °C, and the interfacial resistance was estimated to become 53 mΩcm^2 from the initial value of 20 mΩcm^2. Therefore, we regarded this material as a candidate material which can show durability for commercialization.

---

[1] Published in Hung-Cuong Pham, Shunsuke Taniguchi, Yuko Inoue, Jyh-Tyng Chou, Toru Izumi, Koji Matsuoka, and Kazunari Sasaki, *ECS Trans*., 68(1) (2015)1715-1720.

6.1 Introduction

There have been a number of studies concerning MSCs using Fe-Cr alloys as porous substrate materials, which form semiconductor of Cr_2O_3 scales on their surfaces [1-3]. The scale grows owing to the transport of charged ionic species under an oxygen potential gradient through the alloy/scale/gas interface [4], and the growth may result in a significant increase in the cell resistance during long-term operation. In general, oxidation of metal can be accelerated by increasing temperature. Hammer et al. [5] conducted an accelerated test for a Fe-16Cr alloy and found that the thickness of the surface chromium oxide layer after 1,500 h at 900 °C was equal to that after 16,000 h at 800 °C.

In this chapter, we tried acceleration tests to evaluate durability of the Fe-Cr-Al alloy, previously revealed to show promising characteristic in Chapters 4 and 5. The oxidation resistance of an LSCF-coated Fe-Cr-Al alloy in a long-term at 700 °C in air was investigated, assuming the operating temperature of the MSC is around 700 °C. We measured the mass gain, surface oxide thickness, and electrical resistance by increasing temperature from 700 to 900 °C as acceleration tests to clarify the durability of the Fe-Cr-Al porous alloy substrate.

6.2 Theoretical background of oxidation of metal

In one dimension, the diffusion coefficient D is given by Brownian's equation,

$$D = \frac{1}{2} G X^2 \qquad (1)$$

where (X^2) is the mean-square distance that an atom jumps in a single site change and G is the jump rate (sec^{-1}). The diffusion coefficient D may also be defined in terms of Fick's law, an empirical relation which states that the rate of mass flow j through a unit area is proportional to the concentration gradient ∇C.

$$j = -D \nabla C \qquad (2)$$

To derive the equation for the rate of oxide growth, we consider the motion of the mobile species, a current flux of charged particles j is affected by diffusion along a concentration gradient and motion in any electric fields present. Therefore,

$$j_e(X) = -D_e \frac{dC_e(X)}{dt} + EC_e(X)\mu_e \tag{3}$$

and

$$j_i(X) = -D_i \frac{dC_i(X)}{dt} + EC_i(X)\mu_i \tag{4}$$

where subscripts i and e refer to mobile ions and electrons, respectively. X is the distance in the films measured from the metal/oxide interface, *C(X)* is the position-dependent concentration, and μ is the particle mobility. Enstein's relation between the diffusion coefficient and mobility is the following equation.

$$\frac{D}{\mu} = kT / ze \tag{5}$$

Where k is the Boltzmann constant and ze is the charge on the diffusing particle. Eliminating E in above equation (3), (4), and assuming a steady state ($j_e, j_i = j$) and z = 1, then,

$$j\left(\frac{1}{C_e(X)\mu_e} + \frac{1}{C_i(X)\mu_i}\right) = kT / e\left(\frac{1}{C_e(X)}\frac{dC_e}{dX} + \frac{1}{C_i(X)}\frac{dC_i}{dX}\right) \tag{6}$$

If σ is the total conductivity of the semiconductor, then the transference number t_e and t_i (the fractions of the conductivity resulting from electrons and ions, respectively) are defined by the following equations.

$$t_e\delta = eC_e\mu_e \tag{7}$$

$$t_i\delta = eC_i\mu_i \tag{8}$$

Since C_e and C_i is equal C by charge neutrality and $\mu_e \gg \mu_i$, $t_e \gg t_i$, therefore, $t_e = 1$, $(t_e + t_i = 1)$, and equation (6) may be approximated by the following equation.

$$j = -2\frac{t_i \delta kT}{x^2 C}\frac{dC}{dX} \tag{9}$$

Or $j = -2D_i \frac{dC}{dX}$ (10)

For a certain thickness of thin film X_0, equation (10) may be approximated by the following equation,

$$j = -2D_i \frac{c_1 - c_o}{X_o} \tag{11}$$

where C_1 and C_o are the fractions of cation vacancies at the metal/oxide and oxide/gas interfaces, respectively. The film growth rate, *dX/dt*, is equal to the current flux multiplied by the volume associated with each metal in the oxide:

$$\frac{dX}{dt} = 2D_i \frac{c_1 - c_o}{X_o} V \tag{12}$$

At time t_o corresponding to X_o , equation (12) may be compared to the empirical relation,

$$\frac{dX}{dt} = \frac{K}{X} \tag{13}$$

where K (cm^2s^{-1}) is the parabolic rate constant. Integration of equation (13) yields,

$$X^2 = 2Kt \tag{14}$$

thus, if we can assume the same oxidation mechanism at 700 and 900^{o}C, we can calculate the thickness of the metal oxide.

Estimation of long-term durability by increasing temperature

Based on equation (14), we can express relationship between the thickness (x_{900}) of the metal oxide at 900^{o}C and the operation time (t_{900}).

$$x_{900}^2 = 2K_{900}t_{900} \tag{15}$$

We also express relationship between the thickness (x_{700}) of the metal oxide at 700^{o}C and the operation time (t_{700}).

$$x_{700}^{2} = 2K_{700}t_{700} \tag{16}$$

When we want to accelerate the oxidation at 700^{o}C, we can increase the temperature to, for example 900^{o}C. Rate constant K_{900} increases (compared to K_{700}), and the time t_{900} to reach a certain thickness ($x_{700} = x_{900}$) decreases.

Therefore, we can estimate the value of t_{700} (= durability at 700^{o}C) using the experimental data at 900^{o}C in a short term, based on the equation (15) and (16) as follows.

$$t_{700} = \frac{K_{900}t_{900}}{K_{700}} \tag{17}$$

6.3 Experimental

We measured the interfacial resistance between the porous alloy substrate and LSCF coating at 700, 800, and 900 °C in air in the configuration shown in Figure 3-4. To evaluate durability, we measured the mass gain at 700 and 900 °C in air using an LSCF-coated Fe-Cr-Al alloy plate (20 mm × 20 mm × 0.65 mm) with the same chemical composition as the porous alloy substrate. After these measurements, we analysed the surface oxide layer by SEM and STEM.

6.4 Results and discussion

6.4.1 Interfacial resistances of the alloy at different temperatures

Figure 6-1 shows the interfacial resistance of the LSCF-coated porous alloy substrate at 700, 800, and 900 °C in air. The interfacial resistance was calculated using an apparent electrode area. The interfacial resistance was stable at 700 and 800 °C, but it increased to 38 mΩcm^{2} at 900 °C for 230 h. Figure 6-2 shows the temperature dependence of the interfacial resistance after 230 h following the measurement at 900 °C. Semi-conducting behavior was confirmed by the temperature dependence. Therefore, the interfacial resistance was dominated by electron conduction through the surface oxide layer and not through direct contact with the LSCF coating with the metallic state of the alloy.

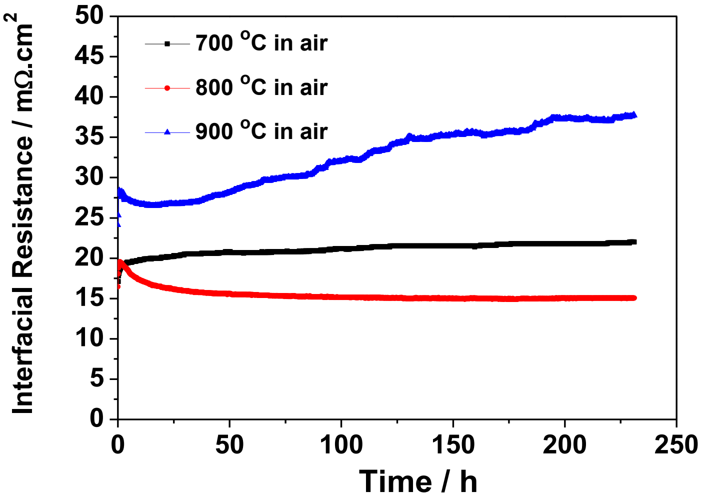

Figure 6-1. Interfacial resistance of the LSCF-coated porous alloy substrate at 700, 800, and 900 °C in air.

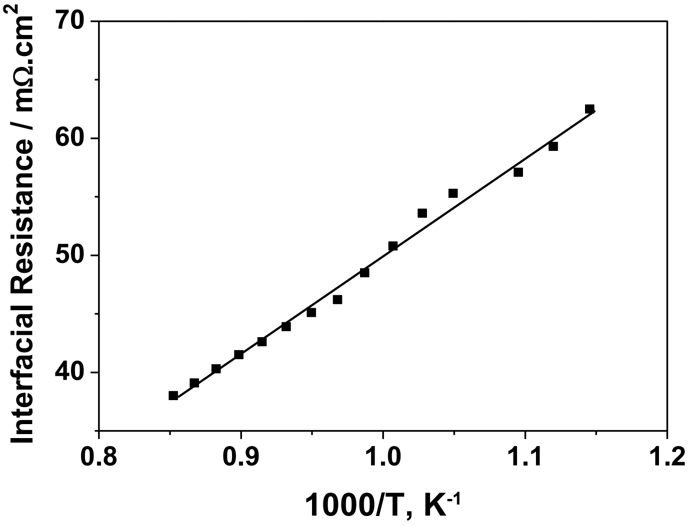

Figure 6-2. Temperature dependence of the interfacial resistance after the resistance measurement at 900 °C shown in Figure 6-1.

6.4.2 Weight increases of the alloy at different temperatures

Figure 6-3 shows the mass gain of the LSCF-coated alloy plate at 700 and 900 °C in air. The mass gain followed the parabolic law (mass gain = $kT^{1/2}$) of Wagner's theory over the whole period investigated (~230 h). The mass gain comes from the growth of the surface oxide layer, and the mass gain at 900 °C is much higher than that at 700 °C. We derived equations for the mass gain at 700 and 900 °C as a function of $t^{1/2}$, where t is the time, as shown in Figure 6-3(b). Figure 6-4 shows the long-term mass gain at 700 °C in air as estimated by extrapolation of the data in Figure 6-3(b). As an example, the mass gain after 17,000 h of operation at 700 °C was estimated to be 0.34 mg/cm^2, which is equal to that after the 230-h test at 900 °C.

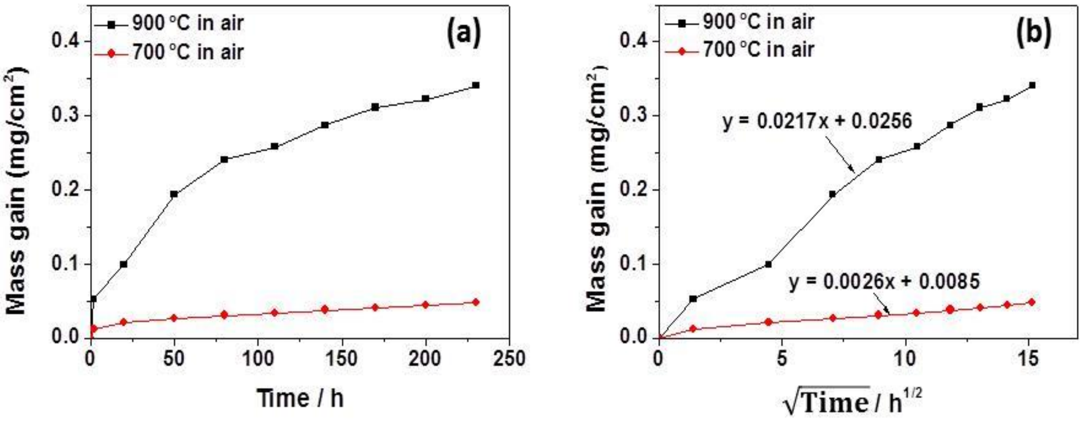

Figure 6-3. Mass gain of the LSCF-coated Fe-Cr-Al alloy plate at 700 and 900 °C in air.

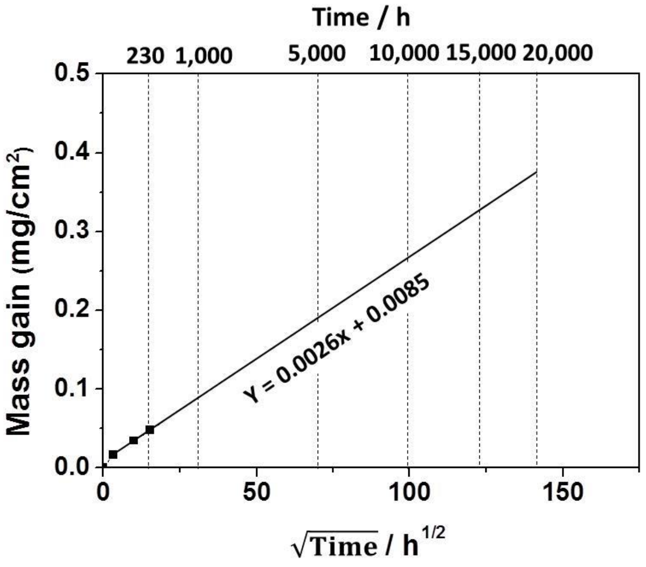

Figure 6-4. Estimation of the mass gain of the LSCF-coated alloy plate in air at 700 °C by extrapolation of the data in Figure 6-3.

6.4.3 Thickness and elemental composition of surface oxide layer after the heat treatments

Figure 6-5 presents an STEM image and EDS mappings of the surface oxide layer of the alloy plate and LSCF coating after 230 h at 700 °C in air. In the case of a porous alloy substrate, we already know the Al_2O_3-based oxide layer contains about 3–4 at% of Sr [6].

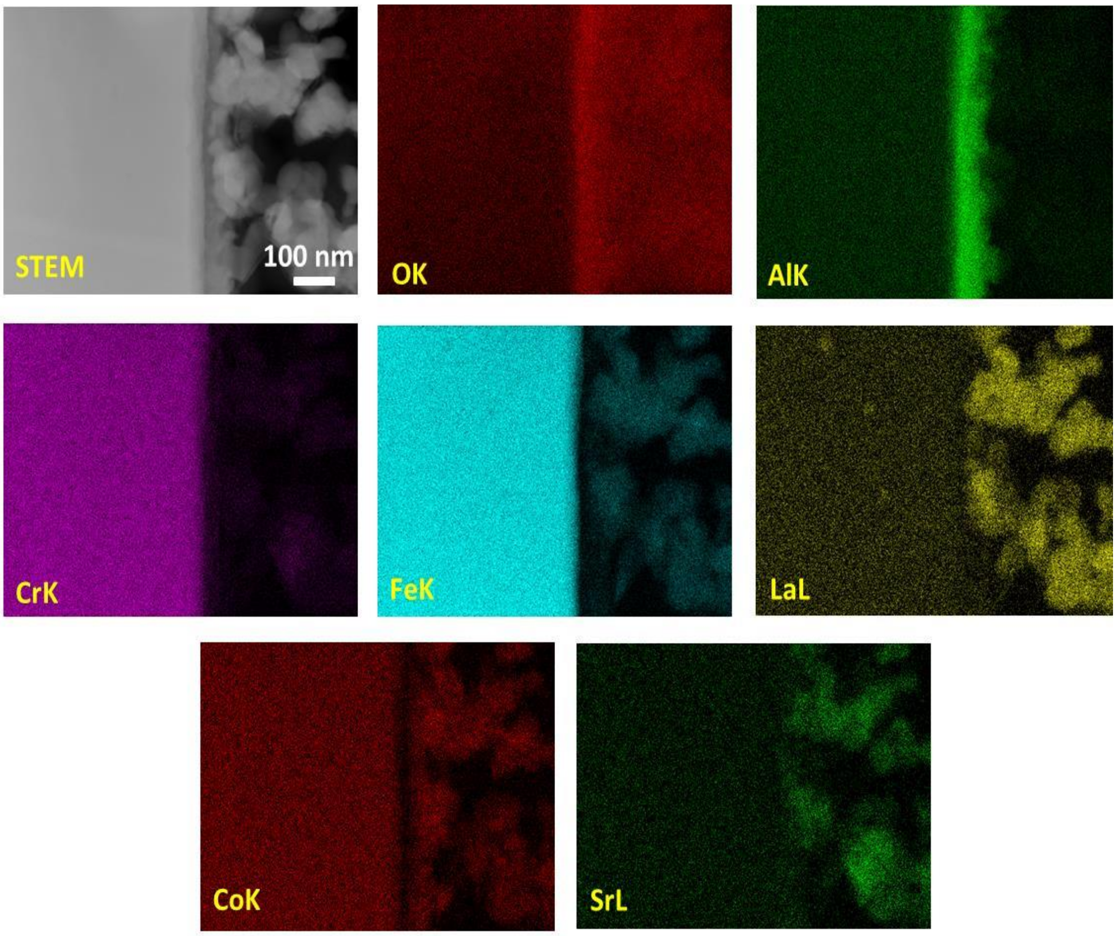

Figure 6-5. STEM image and EDS mappings (raw count maps of O, Al, Cr, Fe, La, Co, and Sr) of the surface oxide layer of the alloy plate after measurement of the mass gain at 700 °C for 230 h in air.

Figure 6-6 presents an SEM image and EDS mappings of the surface oxide layer of the LSCF-coated alloy plate after 230 h at 900 °C in air. The thickness of the surface oxide layer was about 2.2 μm. Chromium oxide appeared inside the Al_2O_3-based oxide layer. On the assumption that the oxidation mechanism at 900 °C is the same as that at 700 °C, Figure 6-6 should reflect the oxidation state after 17,000 h at 700 °C. The interfacial resistance of the LSCF-coated porous alloy substrate after 17,000 h at 700 °C is estimated from the data in Figure 6-2 to be about 53 $m\Omega cm^2$.

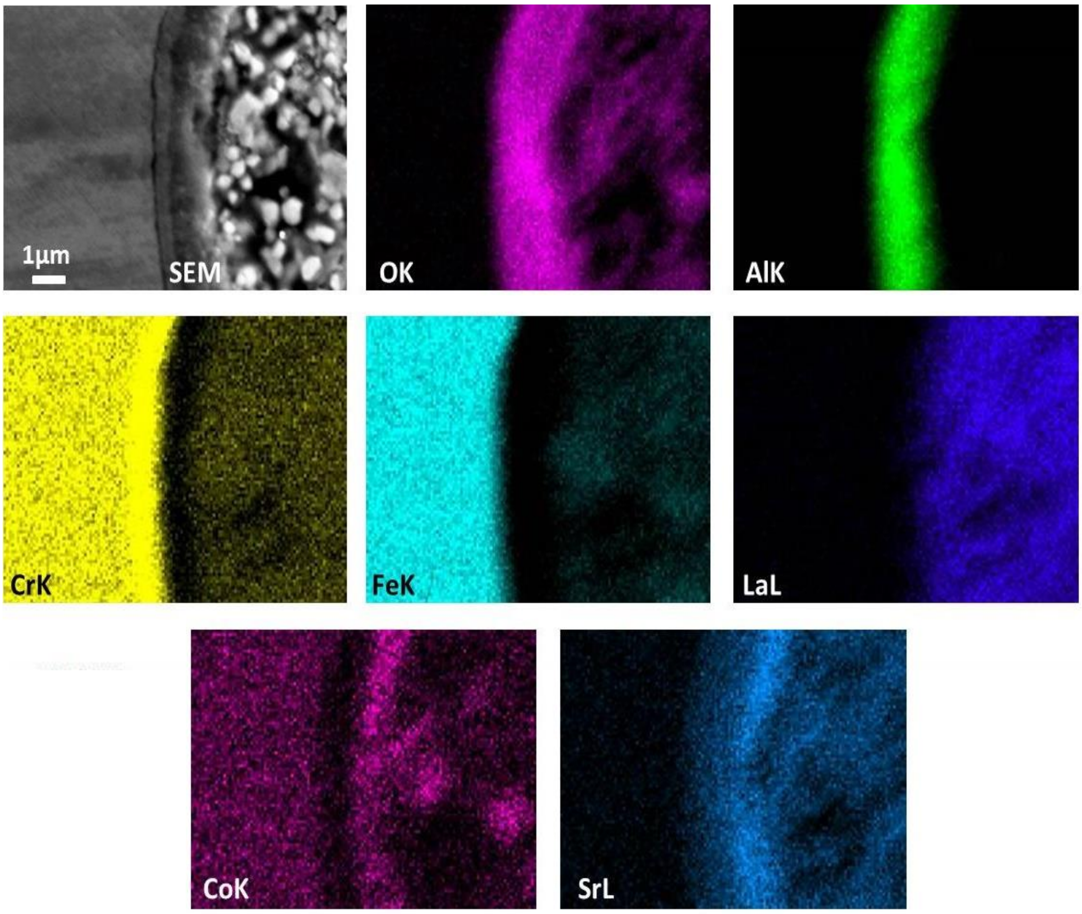

Figure 6-6. SEM image and EDS mappings (raw count maps of O, Al, Cr, Fe, La, Co, and Sr) of the surface oxide layer of the LSCF-coated alloy plate after measurement of the mass gain at 900 °C for 230 h in air.

6.5 Conclusions

We evaluated long-term durability of the Fe-Cr-Al alloy coated with LSCF by increasing temperature as acceleration tests. We measured the mass gain, surface oxide thickness, and electrical resistance by increasing temperature from 700 to 900 °C. The mass gain of the alloy at 700 and 900 °C followed a parabolic law. By extrapolation of the data, we estimated the mass gain after 17,000 h at 700 °C to be equal to that after 230 h at 900 °C. We thus estimated that the interfacial resistance of the porous alloy substrate at 700 °C will increase from 20 mΩcm^2 to 53 mΩcm^2 after 17,000 h of operation based on the results at 900 °C after 230 h in air. Therefore, we regarded this material as a candidate material for commercialization, even though the durability estimated in this chapter is still need improvement.

References

[1] P. Blennow, J. Hjelm, T. Klemensø, Å. H. Persson, S. Ramousse, M. Mogensen, Fuel Cells, 11, (2011) 661.

[2] R. Sachitanand, M. Sattari, J.-E. Svensson, J. Froitzheim, Int. J. Hydrogen Energy, 38, (2013) 15328.

[3] M. C. Tucker, J. Power Sources, 195, (2010) 4570.

[4] H. Liu, M. M. Stack, S. B. Lyon, Solid State Ionics, 109, (1998) 247.

[5] J. E. Hammer, S. J. Laney, R. W. Jackson, K. Coyne, F. S. Pettit, G. H. Meier, Oxid. Met., 67, (2007) 1.

[6] H.-C. Pham, S. Taniguchi, Y. Inoue, J.-T. Chou, T. Izumi, K. Matsuoka, K. Sasaki, J. Power Sources, 297 (2015) 181.

Chapter 7

Conclusions and Perspectives

7.1 Microstructure and Electrical Resistance of Surface Oxide Layer of Fe-Cr-Al Alloy

This dissertation deals with a material of Fe-Cr-Al alloy for metal-supported SOFC (MSC) and investigated its property as porous substrate such as electrical resistance and heat resistance, which are important factors for commercialization. The Fe-Cr-Al alloy generally shows high oxidation resistance in air because of the formation of mainly alumina-based oxide layer on the surface as a protective layer. The oxide layer is stable at high temperature, and it can prevent the chromium poisoning from the alloy to the electrode materials.

We succeeded in decreasing electrical resistance of the surface oxide layer of the Fe-Cr-Al alloy in Chapter 4. A relatively low electrical resistance was obtained when the LSCF-coated porous alloy substrate was heat-treated at 700–800 °C in air. The surface oxide layer was changed to a complex structure consisting of γ-Al_2O_3 polycrystal and $Sr_3Al_2O_6$ crystal growing outward in the same direction as a columnar structure. We hypothesize that the electronic conduction path was generated at a thin interface of γ-$Al_2O_3/Sr_3Al_2O_6$, in which the polarity discontinuities lead to electronic reconstruction and significantly enhance the mobility of the charge carriers. The columnar structure arranged perpendicular to the surface may also contribute to the enhancement of the electronic conductivity by connecting the conduction path from inside of the alloy to the outside. In contrast, the surface oxide layer of the alloy showed a high electrical resistance when the uncoated porous alloy substrate was heat-treated. The surface oxide layer consisted of columnar γ-Al_2O_3 growing in various directions and showed a high electrical resistance due to the electrical properties of γ-Al_2O_3.

We obtained the similar results with the case of LSCF using LSM, LNF or PrSM for the electrode materials in Chapter 5. In the surface oxide layer, small amount of La, Ni, Pr or Sr were observed. We think that the same microstructure as described above was formed for each material, in which small amount of aluminum compound with La, Ni, Pr or Sr may exist between γ-Al_2O_3 columnar crystal growing outward in the same direction. In the case of LNF, the interfacial resistance and activation energy of the electrical conduction were slightly lower than the other cases. Possibility of formation of γ-Al_2O_3/$NiAl_2O_4$, with higher electronic conductivity than γ-Al_2O_3/$Sr_3Al_2O_6$, between γ-Al_2O_3 columnar crystals was suggested.

We evaluated long-term durability of the Fe-Cr-Al alloy coated with LSCF by increasing temperature as acceleration tests in Chapter 6. We measured the mass gain, surface oxide thickness, and electrical resistance by increasing temperature from 700 to 900 °C. The mass gain of the alloy at 700 and 900 °C followed a parabolic law. By extrapolation of the data, we estimated the mass gain after 17,000 h at 700 °C to be equal to that after 230 h at 900 °C. We thus estimated that the interfacial resistance of the porous alloy substrate at 700 °C will increase from 20 mΩcm^2 to 53 mΩcm^2 after 17,000 h of operation based on the results at 900 °C after 230 h in air. Therefore, we regarded this material as a candidate material for commercialization, even though the durability estimated in this study still needs improvement. Figure 7-1 summarizes the results of this study.

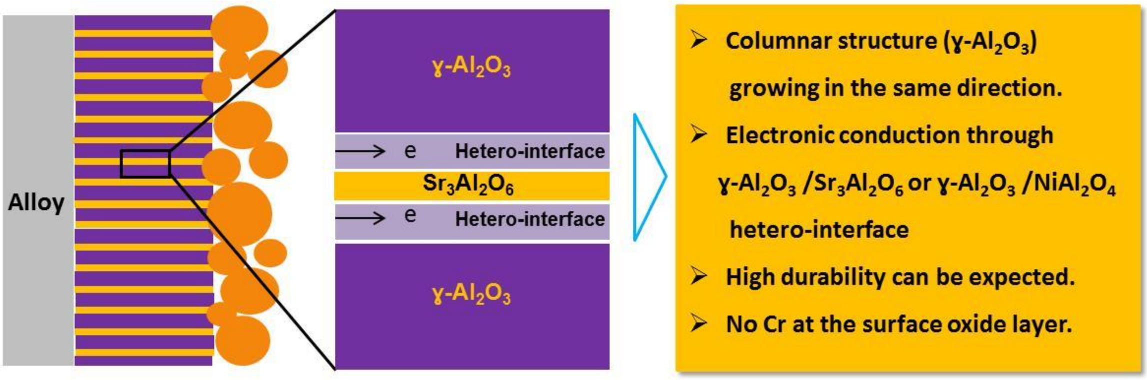

Figure 7-1. Unique microstructure of the surface oxide layer on the Fe-Cr-Al alloy and enhancement of electronic conduction clarified in this study.

7.2 Outlook for future works

We have clarified that the Fe-Cr-Al alloy can be applied for the porous alloy substrate of MSCs. We can expect high durability of MSCs using this material because of not only its stability but also less chromium evaporation.

However, we need to investigate the following issues in more detail as the future works, which may be required for commercialization of MSCs and also for development of new materials.

- Understanding the mechanism of oxide growth and electron conduction in more detail by high resolution analysis. For example, crystal structure can be identified by fast fourier transformation (FFT) using high resolution TEM image. Figure 7-2 shows an example of FFT analysis for γ-Al_2O_3 in the surface oxide layer.
- Detailed study on defect chemistry of the complex oxides such as $Sr_3Al_2O_6$ and $NiAl_2O_4$ and the hetero-structure.
- Improvement of electron conductivity and long-term durability by modifying the crystal structure and elemental composition of the surface oxide layer.
- Development of fabrication procedure of MSCs using the alloy as porous alloy substrates.
- Development and Demonstration of SOFC stacks and systems using HSCs.

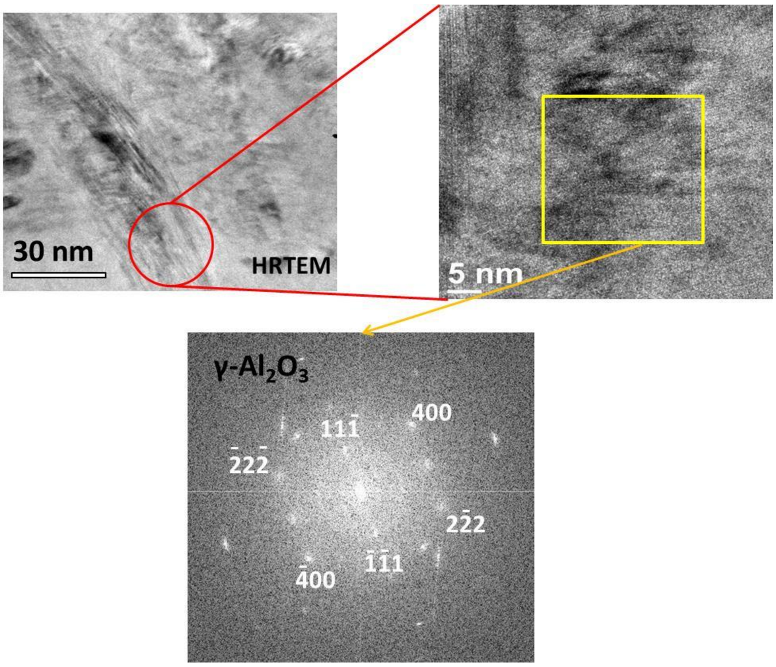

Figure 7-2. High resolution TEM image and FFT image indicating existence of γ-Al_2O_3.

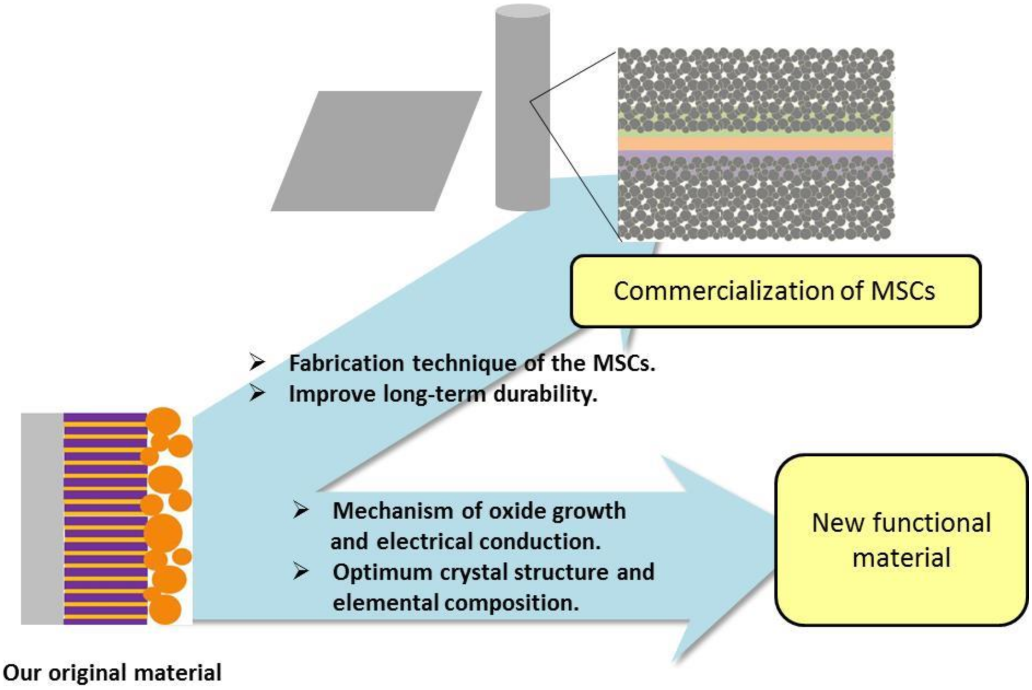

Figure 7-3. Future works for commercialization of MSCs and development of new materials.

Acknowledgements

In the past three and a half years, many people gave me great help in study and life. I am very grateful to what they have done for me. I would like to start by thanking my advisor, Prof. Sasaki, for his guidance throughout my time here. He is always willing to share his knowledge, expertise, and excitements in our research with our group members. His patience and confidence has provided opportunities for me to learn about the advanced theories and technologies in the world, and given me suggestions for drafting this dissertation. The study under his instruction would be the most valuable and unforgettable experience in the rest of my lifetime. I wish to thank him for the possibility he gave me to present my work at international conferences all over the world.

I am deeply thankful to Prof. Taniguchi for his persistent encouragement, helpful suggestions, explanation and scientific discussions. His contributions just can’t be put into words.

I would also like to convey my deep regards to Prof. Shiratori and Prof. Yamazaki for their precious time to read the manuscript, provide the valuable suggestions and advice throughout this process.

Our group members have contributed greatly to my research efforts. Ms. Zaitsu has provided useful university’s information during my stay at Kyushu University. Prof. Chou and Prof. Matsuda greatly helped me analyze the samples by using HRTEM and gave me a lot of useful advice. Especially, I learnt a lot of technique to use FIB and TEM from Mr. Nagai. Finally I’d like to thank my family. My parents, Thach and Khanh, have been constant sources of encouragement and never-ending support. My sister, Huong, has always been a source of joy. Her courage and commitment to helping others is contagious. My accomplishments here pale in comparison to her selfless efforts towards others.